PHD

EIT for void detection in conductive concrete (Alternative Format Thesis)

Davey, Stephen

Award date:
2021

Awarding institution:
University of Bath

EIT for void detection in conductive concrete

(Alternate Format Thesis)

Davey, Stephen

Award date:
2021

Awarding institution:
University of Bath

EIT for void detection in conductive concrete

submitted by

Stephen Davey

for the degree of Doctor of Philosophy

of the

University of Bath

ACE

December 2020

Acknowledgements

I could easily get quite carried away writing this, so I'll have to limit myself to thanking my supervisors, family, friends, and colleagues for their support.

Contents

List of Figures

List of Tables

Glossary

CEM: Complete Electrode Model
CFP: Carbon Fibre Powder
CMRR: Common Mode noise Rejection Ratio
CPE: Constant Phase Element
ECT: Electrical Capacitance Tomography
EIDORS: Electrical Impedance and Diffuse Optical image Reconstruction Software
EIT: Electrical Impedance Tomography
EPI: Electrical Property Imaging
ERT: Electrical Resistance Tomography
FDEIT: Frequency Difference Electrical Impedance Tomography
GP: Graphite Powder
GPR: Ground Penetrating Radar
GREIT: Graz consensus Reconstruction algorithm for EIT
IA: Impedance Analyser
IEM: Instrumental Electrode Model
KHU Mk 2.5: Kyung-Hee University Mark 2.5 EIT machine
MEMS: Mirco-Electrical-Mechanical Sensors
MIT: Magnetic Inductance Tomography
MRI: Magnetic Resonance Imaging
MSDS: Material Safety Datasheet
NDT: Non-Destructive Testing
PPE: Personal Protective Equipment
SFRC: Steel Fibre-Reinforced Concrete
SHC: Self-Healing concrete
SHM: Structural Health Monitoring

SMA: Shape Memory Alloy
SNR: Signal to Noise Ratio
SVD: Singular Value Decomposition
TDEIT: Time Difference Electrical Impedance Tomography
TK-R: Tikhonov regularisation
tSVD: Truncated Singular Value Decomposition
TV: Total Variation
WPCM: Weight Percentage of Carbonaceous Material

Supervisors:
Prof. Kevin Paine (Department of Architecture and Civil Engineering)
Prof. Manuchehr Soleimani (Department of Electronic and Electrical Engineering)

Summary

Electrical Impedance Tomography (EIT) is an imaging method that works by reconstructing a distribution of the electrical conductivity of an object from voltage measurements taken on the object surface. In cases where conductivity variations can be reliably correlated with types of feature, the conductivity distribution gives a good idea of what is inside the object.

Concrete is a near-ubiquitous building material and its production accounts for a substantial proportion of global CO_2 emissions. By improving the resilience of concrete to deterioration and finding methods for assessing the risks posed by cracking and damage, the amount of wasted concrete and thus CO_2 emissions can be reduced.

This project was aimed at developing EIT techniques for the practical problem of imaging of voids and cracks in concrete, to provide a means for assessing those risks as well as for validating the performance of self-healing concrete.

Matured concrete is a good insulator of electricity and applying EIT to it without high-voltage equipment is very difficult. This project investigated the creation of less resistive concrete by adding conductive additions to mortars, and a methodology for applying EIT to this less resistive mortar was developed.

A lot of development remains before EIT can be accepted as a method for assessment of in-use structures, but this work will be of use for anyone attempting to apply EIT to concrete and cementitious materials, as well as reducing the resistivity of those materials.

1 | Introduction

The purpose of this work was to investigate the application of EIT to the problem of detecting and classifying cracks in concrete, with a particular focus on subsurface voids and the practical application of EIT to the problem.

1.1 Motivation for the work

Concrete is an almost ubiquitous construction material, used in almost all mid-to-large scale construction projects. Concrete production accounts for around 2 billion tonnes of CO_2 emissions per year, representing as much as 7% of the global total as of 2011 (Shi et al., 2011).

A number of avenues are being explored to reduce this. Shi et al. reviewed work being undertaken to find alternatives to Portland cement. Construction methods and structural geometries designed to reduce concrete use have been explored. Most relevant to this project is the research into self-healing concrete to make structures more resilient to damage (Paine et al., 2015; De Belie et al., 2018).

For self-healing concrete to be accepted for industrial use its performance must be validated. A number of self-healing mechanisms have been proposed, and the majority of these are more effective at the surface of the concrete - there is a risk of a crack healing only at the surface, with a void remaining that will compromise the performance of the structure. This is illustrated in Fig. 1-1.

The motivation for this work was to investigate the possibility for using EIT to ensure that this behaviour was not occurring. Such a system would also have potential applications for crack classification which would help to determine how much risk a crack in a concrete structure poses; this is discussed in more detail in Section 3.3.

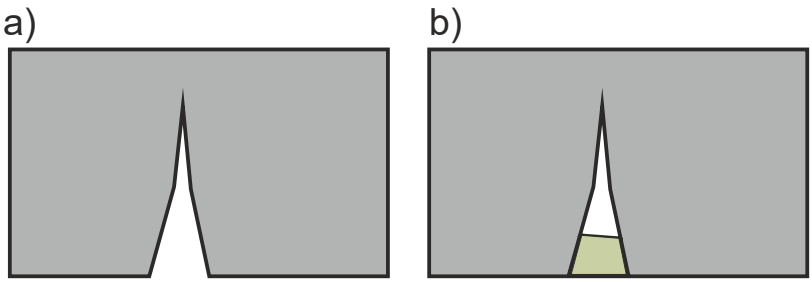

Figure 1-1: a) Cracked concrete. b) Concrete after sub-optimal self-healing process; on the surface the crack appears healed but a void remains.

1.2 Aims and objectives

The broad aim of the project was to work towards the development of a EIT methodology capable of assessing the performance of self-healing concrete and crack classification in a realistic setting. Following the exploratory experimental work, the direction of the project was decided and a set of objectives produced. The whole set of objectives are given below.

1. Assess the feasibility of using EIT on concrete using the available equipment
2. Investigate the electrical properties of mortar containing conductive additions, and thus determine how best to produce a mortar that can be imaged using the available equipment
3. Develop a methodology for performing EIT imaging on this conductive mortar with the available equipment

The exploratory experimental work (objective one) demonstrated the difficulty in imaging mature concrete. The decision was made to concentrate on applying EIT in a real-world setting. The objectives reflect this decision, which is discussed in more detail in Section 1.3.

1.2.1 Concrete and mortars

The project and the objectives related to concrete, however in the experiments performed in service of objectives two and three, mortar was substituted. This was a decision made for practical reasons including mould sizes and the cost of

conductive additions. The work done remains relevant to the broader goals of the project because modifying the cement paste is the most practical way to control resistivity.

1.3 Programme of work

The general aims of this project were to work towards the development of methods for using EIT on concrete, for Non-Destructive Testing (NDT) and Structural Health Monitoring (SHM) with a particular focus on assessing subsurface cracks for the future purpose of validating the performance of self-healing concrete technology. Self-healing concrete was not available during the project, so all experimental work was carried on other materials. The programme of work for this was divided into three parts:

- Exploratory experimental work on EIT on dental plaster and concrete, as well as brief research into other Electrical Property Imaging (EPI) modalities.
- Research into and development of methods for reducing mortar resistivity.
- Application of EIT to conductive mortar cylinders.

Early work (Chapter 5) showed the difficulty of applying EIT to concrete and cementitious materials using available EIT hardware, which informed later work.

The difficulty encountered in actually imaging concrete suggested two general directions for the work. The first possibility was to concentrate on development of image reconstruction techniques, using simulation or experimental work performed using saline phantoms - tanks containing saline solution and inclusions commonly used in EIT research. The other option was to work towards practical application of EIT or other EPI modalities on concrete.

Looking at the existing work on EIT for concrete (Section 3.5) it was decided that the best contribution given the resources available would be to examine the possibility of modifying concrete to reduce its resistivity to facilitate easier NDT and SHM in future construction projects. It was decided to focus on practical considerations in order to improve the prospects for EIT as an industrially accepted method for NDT and SHM.

1.4 Thesis structure

This thesis is divided into 9 chapters, including this one. Two of these chapters are presented as journal papers, each with an introduction discussing how the work described relates to the project overall.

Because of the interdisciplinary nature of the project, the literature review has been split into two parts. Chapter 2 discusses the relevant literature on EIT, while Chapter 3 discusses the relevant literature surrounding cracking and deterioration in concrete as well as other NDT methods for concrete. Taken together, these two chapters introduce the literature around the problem and the methods applied during the project.

Chapter 4 describes the experimental programme, and materials and equipment used. This chapter also includes some supplementary information on methods for the two results chapters presented as papers, where this information could not be included due to restriction on format imposed by journals.

Chapters 5, 6, 7 and 8 give the results of the project. Chapters 6 and 8 have been presented in a journal paper this format; as such they each contain an introduction, methods, results and discussion, and conclusions sections. There is some overlap between the introductions to these chapters and the literature review chapters. Chapters 5 and 7 are presented in a more traditional format, and contains only results, with the associated methods given in Chapter 4.

Chapter 9 gives overall conclusions of the project along with suggestions of further work.

1.5 Summary of outcomes

Obtaining EIT images at good spatial resolution and without noise is difficult, especially when using a relatively resistive material such as concrete. The exploratory work described in Chapter 5 indicated that performing EIT on mature concrete with the available equipment was not feasible, most likely due to the low conductivity of fully hydrated concrete.

A detailed study of the effects of different mix parameters on mortar resistivity was performed, with results in Chapters 6 and 7. Several conductive cylinders intended for imaging were produced on the basis of this work.

Several methods were attempted for imaging these conductive cylinders. A methodology was found which produced some images of reasonable quality. This method required immersion of the cylinders in water, as attempts to obtain images on the same samples when dry using identical electrode arrangements were unsuccessful. This further supports the hypothesis that the difficulty in imaging concrete was at least partially due to the inability of the available equipment to drive sufficient voltage through the low conductivity material. Additionally a method for combining image reconstructions, removing some of the sensitivity to user experience of the EIT imaging process, was described and demonstrated. This is described in Chapter 8.

EIT was ultimately not applied to self-healing concrete or mortars due to issues with the availability of the materials, and testing the technology with these materials is an obvious and important area of further work for this project.

2 | Literature - EIT

Electrical Impedance Tomography (EIT) refers to a tomography method in which a distribution of electrical conductivity is constructed from boundary measurement data. A review of EIT methods is given here to provide some information about the EIT techniques used in the project. EIT is one of the family of Electrical Property Imaging (EPI) methods. The earliest work into EPI was done by Barber et al. (1983) using what they called "applied potential tomography" for medical imaging, and attempted to reconstruct resistivity distributions from voltage measurements which would now be referred to as Electrical Resistance Tomography (ERT) or EIT. One of their early results, on producing resistivity maps of a human forearm, is shown in Fig. 2-1.

2.1 Overview of the process in EIT

An overview of the process of EIT is useful to put the following sections into context. The fundamental goal of EIT is to take a voltage measurement set $\mathbf{V}$ from a number of electrodes on boundary $\partial\Omega$ of body Ω and infer a conductivity distribution σ. This conductivity distribution is visualised to produce an image. Obtaining an EIT image broadly requires three stages.

1. The measurement stage: measurements are taken on a body, in the case of this project these bodies were cylinders made of plaster, concrete, and mortar. This gives the voltage measurement set $\mathbf{V}$. Stimulation frequency and stimulation/measurement patterns can be chosen based on what may be expected to give the most suitable images (although given an automated and flexible device and the high rate at which measurements can be taken it may be totally convenient to simply take measurements on all possible

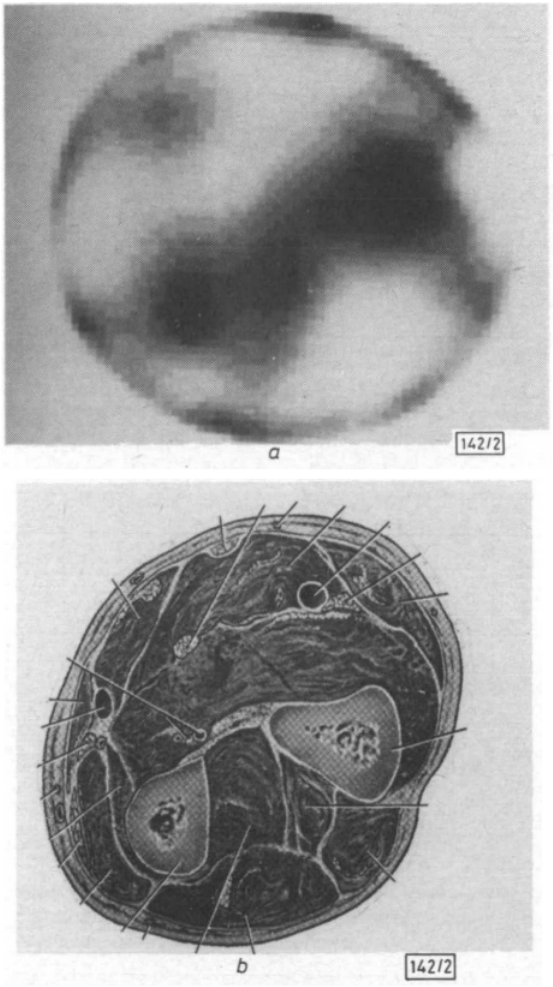

Figure 2-1: Early example of EIT imaging. a) shows the inferred resistivity distribution, b) shows an illustration of a forearm cross-section. From Barber et al. (1983).

settings) provided the correct metadata is associated with each reading. These choices have some effect on the next steps, although reconstruction can generally be performed without consideration for the frequency used. Careful attention must be paid to ensure that the external dimensions of the body and positions of electrodes attached to it are known and recorded to be used in the next stage. Hardware used in the measurement stage is briefly discussed in general in section 2.3, and as applied to this project in section 4.2.1.

2. The forward modelling stage: a computer model of the body and electrodes

is produced, using the information recorded during the measurement stage. This model is used to generate some form of expectation about how perturbations to the conductivity distribution inside the body would affect the measurements taken on the boundary. Usually this is done using finite element analysis to produce a sensitivity matrix (Section 2.4.2), but in the older linear back projection algorithm (Section 2.4.3) the relationship is based on assumptions based on a simple model using equipotential lines. This stage is described in more detail in section 2.2.2.

3. The inversion stage: finally the measurement data and the output of the forward modelling are used to infer a conductivity distribution within the body from $\mathbf{V}$. The conductivity distribution is typically given a colour map, which is applied to the same model produced in the second stage to visualise the outcome. The problem of producing the inversion is described in more detail in section 2.4.

Note that it is not essential that the first two stages be performed in this order. However in practice it is likely to be easier to make the computer model follow the physical arrangement of body and electrodes than vice versa.

2.1.1 Three general types of imaging

It is useful at this point to mention that there are basically three methods of imaging in EPI i.e. three ways of obtaining and using voltage readings. These are:

1. Absolute imaging
2. Time difference imaging
3. Frequency difference imaging

The three imaging types are described here in terms specific to EIT.

In absolute imaging an image is reconstructed from a single set of voltage measurements. This is practically impossible, as it requires the computer model and experimental setup to correspond exactly.

Time difference imaging mitigates this requirement by reconstructing an image from two sets of readings, one taken before an inclusion is added (the "background") and one after. Modelling errors are represented equally in both reading, so when one set of measurements is subtracted from the other their effects are limited. This has been the most commonly used method for imaging in EPI.

Frequency difference imaging operates on the same principle as time difference imaging, except that the voltage difference arises from frequency dependence of the impedance of the body material. If the body and inclusions respond differently to the varying frequency, these differences can be reconstructed. This has the advantage of not requiring a background.

2.2 Related physics

This section gives an overview of the electromagnetic phenomena that are of interest in EIT. This is particularly relevant to the "forward problem" in EIT - the prediction of measured boundary voltages given a conductivity distribution and a current injection pattern.

2.2.1 Complex impedance and resistivity

When a constant voltage is applied to a material or component, the relationship between the magnitude of the applied voltage and the current is given by Ohm's law $V = IR$. In the alternating current (a.c.) case, this relationship basically holds except that the resistance of the material is dependent on the a.c. frequency, and there is the possibility of some phase difference between current and voltage. Complex impedance is the quantity that describes the relationship in this case.

Complex impedance and resistance are quantities relating to a particular piece or component. Resistivity is electrical resistance per unit volume, having the unit ohm metre ($\Omega \cdot m$). It is an intrinsic property of a material. Therefore resistivity is used when discussing the properties of different types of material.

Frequency dependence is the result of inductive or capacitive properties in the material. Impedance as a result of these properties is called reactance. Impedance in concrete is related to its capacitance and resistivity (Whittington et al., 1981); inductance is not a significant factor. The capacitance of the material will cause

the measured voltage to lag the applied current with some phase difference, since the material is charging and discharging at a rate dependent on its capacitance. Thus measuring both the voltage and phase difference allows more information about the material to be inferred.

Complex impedance Z, like all complex numbers, is expressed in either Cartesian or polar form. Both forms are given by Eq. 2.1.

$$Z = R + jX \qquad\qquad Z = |Z|e^{j\theta} \tag{2.1}$$

Where R is the resistance and X is total reactance (both in Ohms) and θ is phase angle. The real part of the complex impedance relates the voltages at the moment when the applied voltage is maximum i.e. phase difference is zero. The modulus of the complex impedance relates the maximum values of the two voltages. Capacitive reactance is given by Eq. 2.2.

$$X_C = \frac{1}{\omega C} \tag{2.2}$$

Where ω is the frequency of the applied signal, and C is capacitance in farads.

The complex impedance of a material or component over a range of frequencies is often expressed graphically using a Nyquist plot. These are described and discussed in the context of concrete in section 3.2.2.

ERT reconstructs impedance magnitude, while EIT can reconstruct both the real and imaginary parts of impedance. Ammari et al. (2014) suggests that separate image reconstruction of real and imaginary components of measurements may give more information and be useful for distinguishing between resistive and conductive regions in a body. Image reconstruction of both the real and imaginary parts of the conductivity map is sometimes referred to as spectral EIT.

2.2.2 Forward modelling

Finite element modelling and simulation of electromagnetic behaviour is important in EPI for developing the sensitivity matrix as described in Section 2.4.2. In the EIT forward problem, voltages are simulated given known current injections and conductivity distributions

The first step in forward modelling is mesh creation; discretising the body being simulated into finite elements. The Electrical Impedance and Diffuse Optical image Reconstruction Software (EIDORS) (Adler and Lionheart, 2006) software used in this project generally uses the "distmesh" meshing algorithm (Persson and Strang, 2004), which is sufficient for 2D reconstruction The elements are assigned conductivity values, and electrodes assigned to the appropriate nodes. Once a suitable model has been produced, the system is simulated as though it were an arrangement of resistors according to the physics described above. The mesh is also used in visualisation once an inverse solution has been found.

2.2.3 Continuum electromagnetics

The most important equation in the EIT forward problem is the Laplace equation given in Eq. 2.3 (Holder, 2004, Chap. 1). This is the equivalent of Kirchoff's current law for a continuum.

$$\nabla \cdot (\sigma \nabla V) = 0 \tag{2.3}$$

Where σ is conductivity, and V is the scalar potential distribution within the medium.

In words, the Laplace equation states that there is no charge source or sink within the body. When a voltage is applied across the body, it produces a scalar field of electrical potential V. The divergence of this scalar field ∇V gives the directions for the vector field of current flow. From $V = IR$ and $\sigma = {}^{1}/_{R}$ the complete vector field of the current flow is given by $\sigma \nabla V$. Finally the divergence operator $\nabla \cdot$ gives the sum of the currents flowing into and out of every point in the body.

2.2.4 Electrode modelling

In order to have a chance of accurately solving the forward problem and predicting voltage measurements, the electrodes and their attachment to the body must be modelled appropriately. The most commonly used electrode model is the Complete Electrode Model (CEM), as described by Vauhkonen et al. (1999).

The CEM is given by the following equations:

$$\nabla \cdot (\sigma \nabla V) = 0, \qquad x \in \Omega \tag{2.4a}$$

$$u + z_l \sigma \frac{\partial u}{\partial n} = U_l, \qquad x \in e_l, \qquad l = 1, 2, 3, ..., L \tag{2.4b}$$

$$\int_{e_l} \sigma \frac{\partial u}{\partial n} dS = I_l, \qquad x \in e_l, \qquad l = 1, 2, 3, ..., L \tag{2.4c}$$

$$\sigma \frac{\partial u}{\partial n} = 0, \qquad x \in \partial\Omega \Big\backslash \bigcup_{l=1}^{T} e_l \tag{2.4d}$$

"Where σ is conductivity distribution, u is the scalar potential distribution, u is the scalar potential distribution, n is the outward unit normal of the boundary $\partial\Omega$, z_l are the contact impedances, I_l are the injected currents and are the corresponding potentials on the electrodes, L is the number of electrodes and e_l denotes the lth electrode, and Ω is the [body]." (Vauhkonen et al., 1999)

The first equation is simply Laplace's equation as in Eq. 2.3. The second relates the measured voltage to the potential field and the contact impedance of the electrode connection. The third is a surface integral over the area of an individual electrode, dictating the current it injects. The fourth equation describes the behaviour of the electric field at points on the boundary not attached to an electrode.

Finally, conservation of charge must be accounted for:

$$\sum_{l=1}^{L} I_l = 0 \tag{2.5}$$

And a reference point for the measured voltages is set:

$$\sum_{l=1}^{L} U_l = 0 \tag{2.6}$$

More recently, W. Zhang and Li (2014) proposed the Instrumental Electrode Model (IEM) to account for non-ideal behaviour of EIT instruments in data acquisition. This adds an additional boundary condition, which for the current source (as opposed to voltage source) case is given by:

$$I_{Sl} + \frac{V_l}{\mathbf{Z}_F} + I_l = 0 \tag{2.7}$$

Where I_{Sl} is the output current of the current source, V_l is the voltage measured on electrode l, $\mathbf{Z}_F$ is a virtual impedance accounting for the total impedance in the drive and measurement part of the equipment, and I_l is the current that finally reaches electrode l.

This final boundary condition essentially accounts for the impedance of the equipment by applying Kirchoff's current law between the device and the electrode. W. Zhang and Li (2014) report better agreement between simulations with a multiphysics package and an implementation of IEM than with CEM, and particularly better results at high frequencies above 500kHz. For the IEM to work it is necessary to have an accurate value for $\mathbf{Z}_F$, which must be determined experimentally.

2.3 EIT hardware

EIT can be performed using any instrument capable of taking impedance measurements. For practical use, several dedicated EIT machines have been built, both in academia and industry. Hardware development was outside the scope of this project. An example of an EIT machine built in academia, the KIT4 described by Kourunen et al. (2009), is shown in Fig. 2-2.

A basic EIT machine needs to have a number of channels which can be driven and measured independently. Beyond this, the only constant requirement is high accuracy and Signal to Noise Ratio (SNR). Measurement and drive may be sequential or simultaneous, with a simultaneous setup giving a much wider range of usable drive patterns. Other features such as variable frequency and automatic calibration can be found in some devices. For spectral EIT (separate reconstruction of Re and Im parts of impedance) it is also necessary for the machine to be able to measure the phase difference between the driven and measured signals. The patterns of stimulation and measurement have some effect on the image reconstruction process and image quality (Adler et al., 2011). Most commonly used is a four point configuration in which (assuming a circular body) one pair of adjacent electrodes is stimulated while other adjacent pairs are used for measurement.

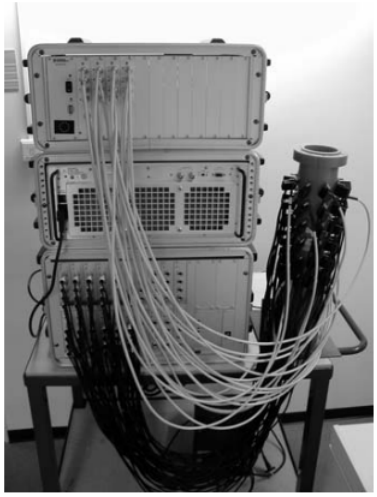

Figure 2-2: An example of an EIT machine. From Kourunen et al. (2009).

However some devices allow this to be changed.

Required SNR varies depending on what is to be imaged. Wi et al. (2014) looked at several studies in medical imaging and found necessary SNR to vary from 30dB to $\tilde{9}$0dB depending on what part of the body was to be imaged. No such study could be found on other materials.

Hardware used in this project is described in Section 4.2.1.

2.4 Inverse problem mathematics

The fundamental task in all EPI, reconstruction of a conductivity distribution based on boundary measurements, is what mathematicians refer to an inverse problem. A number of approaches for image reconstruction exist, and these algorithms can be adapted for use in EIT. It is also useful to describe the most basic algorithm for image reconstruction, linear back projection, which does not come directly from inverse problem mathematics but is still in use in some EPI applications.

2.4.1 The inverse problem

Inverse problems are generally problems of mathematically modelling physical phenomena based on measured data. The inverse problem in EIT is inferring the

conductivity distribution σ of a body Ω from a set of voltage measurements $\mathbf{V}$ recorded on the body boundary $\partial\Omega$. This is an example of an ill-posed inverse problem, which adds some difficulty in producing a good image reconstruction.

An inverse problem is called "well posed" if the following conditions are met (Kirsch, 2011, p. 9):

1. A solution (σ here) to the inverse problem exists.

2. That solution is unique for a given set of measurements.

3. The solution is continuously variable with those measurements.

This first condition is not a problem; anything that can have boundary voltage measurements recorded can be safely assumed to have a conductivity distribution. The second and third conditions are problematic for EIT (and all EPI). Measurement noise inherent to any practical EIT device, as well as the resolution of those devices, means that changes in the conductivity distribution can will produces changes in the measured quantity too small to resolve (Holder, 2004, Chap. 1). This also challenges the uniqueness condition; more than one conductivity distribution may have produced a single set of measurements. Producing a good reconstruction of the conductivity distribution is difficult, and various image reconstruction algorithms approach the problem in different ways. There are several algorithms in use, each having its own advantages and disadvantages.

2.4.2 The sensitivity matrix

Modern methods of image reconstruction tend to make use of a sensitivity matrix. These methods are more versatile and provide better results than linear back projection, which does not use a full sensitivity matrix (see section 2.4.3). The sensitivity matrix relates each boundary measurement to the resistivity or conductivity of every discretised region of the body being imaged. In the literature the term sensitivity matrix is sometimes used interchangeably with "Jacobian", since the matrix takes the form of all of the first partial derivatives of the system:

$$\frac{\partial V_i}{\partial \sigma_j} \tag{2.8}$$

In which i is a particular measurement, for example the voltage difference between electrode 5 and 6, and j is the element number from the FEM. The sensitivity matrix thus relates σ to V. If the ill-posedness of the problem could be ignored, the conductivity distribution could be calculated from:

$$\sigma = J^{-1}V \tag{2.9}$$

The sensitivity matrix can be produced by repeatedly solving the "forward problem" - calculating boundary measurements from an invented conductivity distribution and current injection - by simulation, with different values of σ in each element on each run. By altering the conductivity map the effect of each region on each boundary measurement can be inferred. In modern EPI software, the sensitivity matrix can also be calculated using an adjoint model to improve computational efficiency.

The sensitivity matrix is linearised around a particular point - the linearisation point is the starting conductivity distribution used by the perturbation method. This causes inaccuracy in cases where the distribution is significantly different to that assumption, or where the conductivity discontinuities are very large. This problem can be mitigated to an extent using iterative algorithms where the sensitivity matrix is recalculated on every iteration, but this adds computation time and is often not necessary.

2.4.3 Image reconstruction algorithms

Some commonly used algorithms for image reconstruction in EIT are described here; this list is by no means exhaustive.

Linear back projection

Linear back projection was the earliest algorithm applied to EPI (Barber et al., 1983). Rather than calculating a sensitivity matrix based on physical simulation, an analogous map of sensitivity of measurements to region conductivities is assumed based on the space bounded by the edges of the measurement electrodes, and the equipotential lines from the driving electrodes pair.

Once the sensitivity regions have been estimated for each measurement, resistivity values calculated from the voltage differences are back projected into them.

This produces an image for each current injection pattern; all of these images are summed to produce the final image (Barber et al., 1983).

Linear back projection has several associated problems. The sensitivity regions are based on predictions of current flow with no inclusions; any inclusion would alter the pattern of the equipotential lines. The algorithm would therefore produce worse results as the actual conductivity became further from the assumed conductivity. The other significant problem was of calculations becoming extremely complex when trying to reconstruct an image in 3D. Once these limitations became a problem, research in EIT moved to using sensitivity matrix based approaches.

Tikhonov regularisation

Tikhonov regularisation (TK-R) is currently the most commonly used image reconstruction algorithm in EPI literature, although it is impossible to say how commonly used it is in industrial EPI applications due to the closed-source nature of most equipment and software.

Regularisation methods solve inverse problems by using some prior knowledge of the problem. Two factors must be balanced - the error between the solution and the data, and this prior knowledge of the problem. This can be expressed as the Tikhonov functional as given by Kirsch (2011, p. 40), expressed in EIT terms by Eq. 2.10.

$$\| J\sigma - \mathbf{V} \|^2 + \alpha \| \sigma \|^2 \tag{2.10}$$

This leads to the TK-R equation for a conductivity distribution, given by Eq. 2.11:

$$\sigma = (J^T J + \alpha R)^{-1} J^T V \tag{2.11}$$

In TK-R the prior assumption is of a uniform conductivity distribution. This prior knowledge is expressed using the hyperparameter α and a regularisation matrix R (often called the prior). This assumption of uniformity results in R being an identity matrix of the appropriate size. The regularisation matrix can be constructed to emphasise certain types of feature or otherwise influence the result, for example a Laplacian prior will result in smoothing of discontinuities in the conductivity.

tSVD

Truncated Singular Value Decomposition (tSVD) is an alternative method of regularisation, attempting to achieve the same thing as TK-R. Singular Value Decomposition (SVD) is the factorisation of a matrix, such that $A = U\Sigma V^T$ where Σ is a diagonal matrix consisting of the singular values σ of matrix A. There are several uses for this and it is a powerful tool in linear algebra; for this problem it provides a pseudoinverse $A^+ = V\Sigma^+U^T$ (Hansen, 1987) which could be applied in $\sigma = J^+V$ since J is not necessarily invertible. However this will not produce satisfactory results due to ill-posedness.

tSVD defines an approximation of the matrix A thus:

$$A_k \equiv U\Sigma_k V^T \tag{2.12}$$

Where Σ_k is a diagonal matrix consisting of the k largest singular values of A with other elements set to zero. This filters out the contribution of the weaker singular values, and reduces the sensitivity of the solution to errors in the data or the sensitivity matrix. Hansen also proposes an alternative filter in which the diagonal elements of Σ_k are set as $\sigma^2/(\sigma^2+\lambda^2)$ so as to provide a smoothing filter which dampens the effects of singular values smaller than λ.

Values of k or λ must be chosen by the user, similarly to the hyperparameter in TK-R. The general process of tSVD is very similar to TK-R with the differences being the choice of filter and filter parameters, and the inversion itself.

GREIT

The Graz Consensus Reconstruction algorithm for EIT (GREIT) (Adler et al., 2009) was developed as an attempt to produce an algorithm incorporating best practice knowledge from the clinical EIT community. The original publication of GREIT also defined several figures of merit, referred to as the GREIT parameters. These parameters are applicable to tomograms produced by any algorithm, as well as being central to the way GREIT works.

GREIT works by using desired performance parameters to produce a reconstruction matrix $\mathbf{R}$. Conductivity changes and measurement noise are represented in separate sets of training data, and a desired output is produced using the figures of merit - for example, zero position error. Once this is done the problem is

to produce an $\mathbf{R}$ that produces the output with the closest possible values for the figures of merit. Each of the figures of merit is weighted when calculating $\mathbf{R}$. If the desired behaviour for each of the figures of merit is ideal, and the weights are uniform, GREIT is equivalent to TK-R. Once $\mathbf{R}$ has been produced, the reconstruction is simply $\sigma = \mathbf{R}V$. GREIT gives more control over different parts of the reconstruction than other algorithms, but also requires work to determine the best weighting scheme in the figures of merit when calculating the reconstruction matrix.

Iterated Tikhonov

The iterated TK-R algorithm is a combination of the standard TK-R algorithm and the Newton-Raphson method (Yang, W. Q. and Peng, 2003)(Yang and Peng, 2003). Newton-Raphson optimisation is used to minimise the error between the measured voltages and the voltages predicted from the conductivity distribution. The algorithm begins by finding a conductivity distribution σ using standard TK-R. This σ is then used in a forward simulation, producing a simulated voltage set V. A new distribution is then calculated using the iterative procedure:

$$\sigma_{k+1} = \sigma_k - (J_k^T J_k + \alpha R)^{-1} J^T (V_k - V) \tag{2.13}$$

Where k is the iteration number, and all other symbols are as in standard TK-R.

The process can be run for a predetermined number of iterations, or stopped when $V_k - V$ falls below a certain value. A pseudocode example of this is given below.

```
Voltage data 1 = Import(file1)
Voltage data 2 = Import(file2)
VDiff = Voltage Data 2 - Voltage data 1
tolerance = user input()
Element data = tkr(model)
Vcalc = 0
While (Vcalc - Vdiff) > tolerance
       Previous element data = Element data
       Jk = calculate Jacobian(Previous element data)
       Vcalc = Jk * Previous element data
       Element data = ((Jk'*Jk + Alpha*R)^-1) * ...
              (J'*(Vcalc - VDiff))
End
```

Depending on the choice of tolerance, the error in measured and calculated voltage may never decrease sufficiently so it is probably more sensible to loop through a predetermined number of iterations.

Total Variation

Regularisation methods work by balancing two conflicting interests: minimising the error between the solution and measured data, and using prior information to ensure that the solution is plausible and not totally noise dominated. In the derivation of the TK-R equation, L_2 norms are used to calculate the magnitudes of errors in both of these terms. In regularisation using Total Variation (TV) L_1 norms are used instead (Rudin et al., 1992). TV regularisation tends to produce better results for imaging of cracks in concrete(see the passage about the work of Smyl et al. (2018) in Section 3.5) but is more complex to implement than more commonly used methods. An implementation of TV regularisation for EIT is given by González et al. (2017) along with some information about the distinction between the isotropic and anisotropic variants of TV. González et al. tested TV regularisation in some saline phantom studies, and found that with the right parameter choices it provides excellent reproduction of the size and position of the inclusion, with some interesting distortions to shape.

2.5 Applications for EIT

The earliest practical application of EIT/ERT was medical imaging. Barber et al. (1983) used an ERT system to produce cross-sectional images of a human wrist, with lower conductivity bone being readily distinguishable from higher conductivity flesh. Since then the technology has been progressed and considered for several medical applications. Generally ERT or EIT are considered over other EPI modalities since measurements are easier and the need for physical contact with the body is not typically an issue. EIT is not well suited to conventional pure imaging applications in the same way that X-Ray and Magnetic Resonance Imaging (MRI) are because it provides much lower spatial resolution in images.

However EIT has characteristics that give it advantages over these technologies in certain applications. EIT technologies can be operated at very high temporal resolution and do not involve subjecting a patient to any harmful ionising radiation. This makes EIT well suited for longer duration patient monitoring. Swisstom AG (2013) has marketed an EIT based device for monitoring of lungs which can be applied for the duration of a hospital stay. The system is able to provide more detail than existing monitoring devices

Packham et al. (2012), L. Yang et al., (2016) and other have worked towards the use of EIT for stroke detection. This is potentially an excellent application for EIT since the equipment is much more portable than radiation based imaging methods and could be carried in an ambulance.

M.H. Choi et al., (2007), Boverman et al. (2008), Murphy et al. (2017) and others have worked towards using EIT for mammography. This would remove the need to expose patients to X-Rays, improving patient safety. Murphy et al. investigated rotating the electrode array around the target in order to improve resolution, using experimental arrangements shown in Fig. 2-3.

EIT has also been suggested for use in human-computer interfaces. Yao and Soleimani (2013) used EIT and a conductive fabric to create a pressure mapping system that could be incorporated into garments or used in robotics. Y. Zhang et al., (2016) and Y. Wu et al., (2018) have developed EIT devices worn on users' wrists which can correlate different conductivity maps of the forearm with a number of hand gestures. The equipment is small enough to be potentially of use with mobile devices.

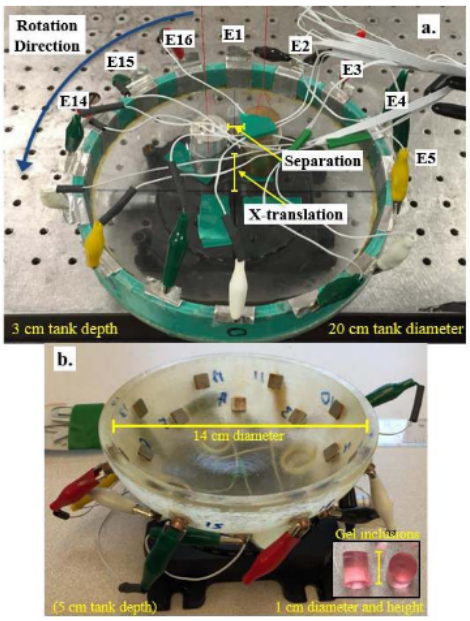

Figure 2-3: Experimental simulation of EIT imaging using rotating electrodes for mammography. a. shows a setup typical of experimental simulations using EIT, while b. shows a tank and electrode arrangement designed for mammography. From Murphy et al. (2017).

2.6 Conclusions

EIT remains a relatively niche technology due to its combination of high temporal and low spatial resolution. However in some applications it opens up some unique possibilities impossible with other technologies, such as the long term monitoring provided by the Swisstom AG device.

Some examples of EIT being applied to concrete and cementitious materials are discussed in Section 3.5.

3 | Literature - Concrete properties and assessment

Concrete is a complex material, and can be studied to great depths along a number of axes. This chapter contains some very general information on concrete and its cracking behaviours as well as a literature review on its electrical properties and existing methods of Structural Health Monitoring (SHM) and Non-Destructive Testing (NDT).

3.1 Composition of concrete

Concrete is a composite material ubiquitous in modern construction. Concrete consists of aggregates bound together by hydrated cement. The aggregates support the bulk of compressive loads, and typically consists of gravel and stones of different sizes depending on the load to be supported. The water/cement mixture must ensure that the concrete remains bound when under the design loads, so an appropriate water:cement ratio is necessary. Water:cement ratio also strongly influences the viscosity of the concrete in its fluid form before hydration, and thus is important when considering the possibility of manufacturing a given concrete element. In order to achieve necessary strength and workability, plasticisers are sometimes added to the water/cement mixture. Concrete is often reinforced with metal bars (sometimes called "rebar") to provide some capacity for tensile loading.

After casting, concrete undergoes a process called hydration. This is where liquid water bonds with the cement and hardens. Concrete changes in strength over this process. In most cases it will have achieved 90% of its maximum strength after around 30 days of hydration.

3.2 Electrical properties of concrete

Knowledge of the electrical properties of concrete has been shown to have uses far outside of NDT and imaging. In particular they have been found to be related to the state of the concrete in the hydration process (Forde et al., 1981), which is known to be related to its mechanical properties. Thus electrical measurements provide a way to estimate the strength of a concrete element at a particular point in time, provided that the details of the time development of the electrical and mechanical properties of that particular concrete are known.

3.2.1 Conduction paths

Whittington et al. (1981) produced an equivalent circuit model for concrete, given three possible conduction paths. These are conduction exclusively through the cement paste; exclusively through the aggregate; and through the cement paste and aggregate in series. This is illustrated by Fig. 3-1.

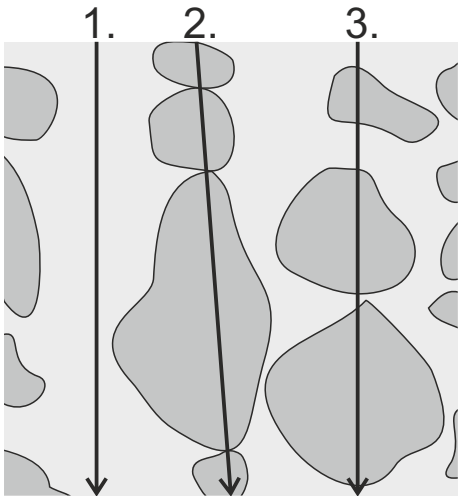

Figure 3-1: 1. Conduction through cement paste. 2. Conduction through the aggregate. 3. Conduction in series through both phases.

Whittington et al. give typical resistivity values of cement paste of 10−13 Ω·m. They also offer some typical resistivity values for aggregates, which are several orders of magnitude higher. Thus the majority of the current passes though the cement paste, and the resistivity of concrete is strongly dependent on both the resistivity of the cement paste and the proportion of paste to aggregates.

3.2.2 Resistivity and frequency response of concrete from literature

The electrical properties of concrete and cementitious materials have been studied, principally for the aforementioned purposes of assessing hydration status. Hornbostel et al. (2013) gives a typical resistivity for dry concrete as 10^6 Ω·m. Yim et al. (2017) gives the resistivity of fully hydrated and dry cement paste (which is more relevant to the work presented in Chapter 6) as between 10^3 Ω·m and 10^4 Ω·m. In both cases, material that is not fully hydrated, water saturated, or both, would have lower resistivity.

Forde et al. (1981) studied the resistivity of concrete over a long period and found that the most rapid changes over time occur in the first 20 or so days of curing, but also that the resistivity continued to change more slowly over more than 100 days. This result would be expected to hold for mortar since the changes are occurring in the cement.

McCarter (1994) took average resistivity values across a 1Hz to 15MHz frequency range for different concrete compositions, and found a range of values from 0.815 Ω·m to 14.69 Ω·m. This is a significant variance depending on mix. The experimental procedure has some effect on the recorded readings, so these results are best used for comparison between mixes used in the study. Also of interest from the perspective of Electrical Impedance Tomography (EIT) is the strong frequency dependence of the resistivity in the kHz range. This would suggest that Frequency Difference Electrical Impedance Tomography (FDEIT) may be feasible for concrete.

Nyquist plots

Complex impedance is described in more detail in Section 2.2.1. Studies into the electrical properties of concrete have generally investigated the complex impedance of the concrete rather than the resistance, and this has generally been measured over a range of frequencies. Complex impedance spectra are used because the information over the range of frequencies can be used to make inferences (although not necessarily detailed ones) about mix properties, hydration state, and the effects of the measurement equipment on the reading. Results of these studies are often expressed using Nyquist plots.

A Nyquist plot for complex impedance shows real (Re) impedance on the X axis and negative imaginary (Im) impedance on the Y axis. Each point gives the complex impedance at a particular frequency. A Nyquist plot obtained during the work discussed in Chapter 6 is given in Fig. 3-2.

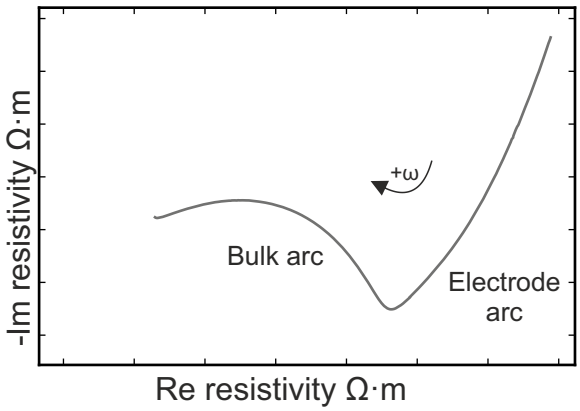

Figure 3-2: An example of a Nyquist plot for complex resistivity of mortar. The arrow indicates increasing frequency.

Fig. 3-2 shows the results of a measurement on mortar, and is a typical result similar to those obtained by McCarter et al. (1988). Plots obtained for concrete by McCarter (1996) and others show the same overall shape, with some variation.

The electrode arc is observed at lower frequencies. This arc is dominated by the behaviour of the contact between the electrode and cementitious material. The bulk arc is observed at higher frequencies, and is dominated by the capacitance and polarisation behaviour within the cementitious material (McCarter, 1994).

McCarter (1996) gives a number of Nyquist plots for various concrete mixes. Changes to the mix proportions resulted in larger changes to Re impedance than Im, and no change to the plot shape. Ordinary Portland cement and pulverised fuel ash based concretes are presented, and the different materials do result in different shapes, particularly in the electrode arc.

Equivalent circuits

By using the complex impedance information it is also possible to model an equivalent electrical circuit of the material being measured. The actual circuit

model must be developed based on the physical characteristics of the experimental system, with different physical characteristic corresponding to parts of the circuit. This is illustrated by Fig. 3-3, adapted from (Brantervik and Niklasson, 1991).

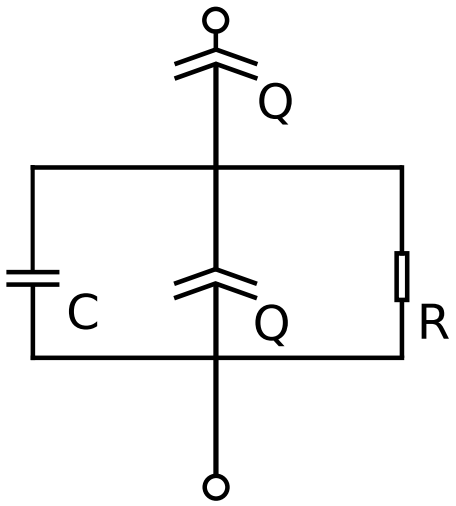

Figure 3-3: Equivalent circuit for typical mortar under certain humidity conditions, after Brantervik and Niklasson (1991).

Where R is a resistor, C is a capacitor, and Q is a Constant Phase Element (CPE), an invented component similar to a capacitor used to fit experimental data. CPE behaviour is sometimes attributed to the effects of a material's surface interacting with electrodes (Jorcin et al., 2006); as such they are common when modelling cementitious materials. See Barsoukov and Macdonald (1987)[Section 2.2.2.2] for a detailed explanation of CPEs and their behaviour.

Once a model has been developed, the frequency response can be used to calculate values for the components. This allows the numerical comparison of each conduction path within the material. Models for conductive cementitious materials or those with other additions are necessarily more complex than those for conventional ones, due to a greater number of conduction paths to be considered. A number of equivalent circuit models for cementitious materials are reviewed by Hu et al. (2019).

3.2.3 Production of conductive concrete

Several investigators have worked on modifying the resistivity of concrete. This has had three main applications:

- Self-heating concrete (Gomis et al., 2015)
- Electromagnetic shielding (Khalid et al., 2017)
- Self-sensing concrete (Chen et al., 2017)

Aside from these applications, conductive concrete has the potential to facilitate the use of EIT by reducing the resistivity and making it easier for existing EIT equipment to penetrate a concrete body.

A number of substances may be used as conductive additions. Xie et al. (1995) lists metallic and conductive fibres including metallic glass fibres and carbon fibres, particles including those made of conductive polymers, coke breeze, and metallic or graphite flakes. Pan et al. (2015) conducted a review of the additions and substitutions to concrete mixes used to produce conductive concretes for self-heating applications. The substances mentioned by Pan et al. are graphite powder, carbon black, aluminium chips, carbon fibre, steel fibres, steel wool, carbon nanofibre, and the replacement of some fraction of aggregates using conductive particles such as steel slag. Gomis et al. also mentions using carbon nanotubes.

Cost is a large factor in the choice of addition or substitution, beyond the effect on resistivity. Depending on the proposed application the effect on durability and thermal properties may also be important. Replacing a fraction of typical aggregates with conductive particles will add cost, as will any addition in the cement paste. Carbon nanofibres and nanotubes in particular have an extremely high cost per unit mass compared to many of the other suggested substances. Adding steel fibres or wool to the cement paste may be cost-effective even in large concrete elements, but as J. Wu et al., (2015) mentions they are vulnerable to corrosion, which increases resistivity. Conductive additions in general may necessitate additional controls in the process of manufacturing concrete, since they can be damaging to electrical circuits. For example, the Carbon Fibre Powder (CFP) used by the project requires that equipment be protected to a standard of IP65 against dust. Carbon based additions also have additional health risks when compared to working with conventional concrete components, which must be addressed with appropriate Personal Protective Equipment (PPE).

Modelling of conductive concrete

Percolation theory and effective medium theory are both useful areas of mathematics for understanding the effects of conductive additions on the electrical properties of cementitious materials.

Effective medium theory is concerned with the modelling of properties of composite materials based on known properties of their constituent elements. Suryanto et al. (2016) gives an effective medium theory expression for the electrical conductivity of a composite containing randomly oriented short fibre additions, reproduced in Eq. 3.1:

$$\sigma_e = \sigma_m \left(1 - \frac{\phi(\sigma_m - \sigma_a)[(\sigma_a - \sigma_m)(S_{11} + 2S_{33}) + 3\sigma_m]}{3(\sigma_a - \sigma_m)^2(1-\phi)S_{11}S_{33} + \sigma_m(\sigma_a - \sigma_m)R + 3\sigma_m^2}\right) \tag{3.1}$$

Where σ_e is the electrical conductivity of the composite, σ_m is the electrical conductivity of the matrix, σ_a is the electrical conductivity of the addition and ϕ is the volume fraction of the addition. Values of R, S_{11} and S_{33} are given below.

$$R = 3(S_{11} + S_{33}) - \phi(2S_{11} + S_{33}) \tag{3.2}$$

$$S_{11} = \frac{Ld^2}{2(L^2 - d^2)^{1.5}}\left[\frac{L}{d}\left(\frac{L^2}{d^2} - 1\right)^{0.5} - cosh^{-1}\frac{L}{d}\right] \tag{3.3}$$

$$S_{33} = 1 - 2S_{22} \tag{3.4}$$

Where L is length and d is diameter of the particle additions. Suryanto et al. also gives a version for fibres which are not randomly aligned in one plane, reproduced in Eq. 3.5:

$$\sigma_e = \sigma_m \left(1 + \frac{\phi(\sigma_a - \sigma_m)[(\sigma_a - \sigma_m)(S_{11} + S_{33}) + 2\sigma_m]}{2(\sigma_a - \sigma_m)^2(1-\phi)S_{11}S_{33} + \sigma_m(\sigma_a - \sigma_m)R' + 2\sigma_m^2}\right) \tag{3.5}$$

S_{11} and S_{33} have the same definitions as in Eq. 3.1, while R' is given below:

$$R' = (2 - \phi)(S_{11} + S_{33}) \tag{3.6}$$

Percolation theory is a field of mathematics dealing with the formation of

clusters by elements randomly distributed in some space (Stauffer and Aharony, 1994). This field has many applications far outside the scope of this work, but one application that is relevant is in the production of conductive concrete using conductive additions as described above. If the additions are randomly distributed within the concrete matrix then the formation of clusters of these additions will be a significant factor in the electrical properties of the resulting material.

The most interesting aspect of percolation theory here is the concept of the percolation threshold. Stauffer and Aharony describes this as a "critical value" of the probability that an element is present in some subdivision of the space at which a cluster of elements will provide a path from one side of the space to the other. Assuming random distribution of the addition, the volume fraction of the addition can be used in place of probability when considering conductive additions in a concrete matrix.

The expression for electrical conductivity of a composite containing conductive additions is given by Eq. 3.7 from Boland et al. (2016).

$$\sigma_e \propto (\phi - \phi_{c,e})^{n_e} \tag{3.7}$$

Where σ_e is the electrical conductivity of the composite, ϕ is the volume fraction of the addition, $\phi_{c,e}$ is the percolation threshold, and n_e is the exponent. The constant of proportionality in Eq. 3.7 is the conductivity of the addition (Huang, Y. et al., 2020).

When ϕ is greater than the percolation threshold, further increases will yield a proportionally smaller change to conductivity, for example as observed by H.J. Choi et al., (2019, Fig. 4) and others.

3.2.4 Resistivity results of existing work producing conductive concrete and cementitious materials

Gomis et al. gives d.c. resistance of mixes with different quantities of carbonaceous conductive additions. Although the other parameters of the mix are not kept constant, it is clear that even a relatively small quantity of conductive addition has a significant effect on resistance. Their standard, non-conductive mix has a resistance of 3100 Ω, while a mix containing 5% of Graphite Powder (GP) by weight has 1470 Ω and one with 0.25% of carbon nanotube addition has 1650

Ω.

Mason et al. (2002), Wansom et al. (2006), and Suryanto et al. (2017a) have all investigated the frequency response of cementitious materials with some conductive additions.

Mason et al. measured impedance spectra between 10MHz and the "Hz range" for cement pastes containing conductive fibres at 1% by weight in each case. The samples were purely cement, water, and fibres. All measurements were performed at three days hydration. They found that the addition of the fibres led to an additional bulk arc forming in the frequency response; a very significant change to the shape. They also measured d.c. resistance and found that it was not substantially changed by the addition of the fibres. The d.c. resistance also agreed well with the Re impedance at the end of the electrode arc/beginning of the bulk arc for the cement paste, taken to indicate that not enough fibres were present to form the dominant conduction path in the material.

Wansom et al. measured impedance spectra for cement paste containing carbon nanotubes (two mixes, one of 0.75% and the other 1% by weight) and methylcellulose and a superplasticiser in 0.4% and 0.5% by weight respectively. The frequency sweep was particularly large, between 0.1Hz and 30MHz. Measurements were taken at a number of time points until eight hours after mixing, and then again after demoulding at one day. The measurements at one day are of most interest here as they are more comparable to the results described in Chapter 6. Similarly to Mason et al., they found a second bulk arc when additions were present in some cases. In others another feature is evident, resembling a "dog-leg" in the electrode arc, where the gradient is much smaller.

Suryanto et al. used electrochemical impedance spectroscopy to assess the effects of different quantities of fly-ash. Fly-ash is a replacement material for Portland cement, the use of which can reduce the embodied CO_2 of a concrete structure. Electrochemical impedance spectroscopy allows the characterisation of the fly-ash in terms of its unburned carbon content, which affects its suitability as a cement substitute. This work studied cement pastes containing six fly-ashes in four different replacement percentages, including one 0% reference cement paste. Nyquist plots are presented from 100Hz to 10MHz. The shape of the frequency response is undoubtedly changed by the addition of the fly-ash, and the changes become more pronounced as more conductive material is present.

The fly-ash creates a "plateau" region, similar to the dog-leg feature in the work of Wansom et al., between the electrode and bulk arcs which can take different shapes depending on the quantity of unburned carbon. Higher quantities of the conductive material result in the plateau region becoming more pronounced and shaped more like the second bulk arc in Mason et al.'s work.

All three of these studies into the frequency response of conductive cementitious materials found significant changes as a result of the conductive additions. These changes in shape presumably demonstrate a change in the predominant conduction paths within the cement matrix. It should be noted that the frequency response results presented in these studies are for relatively small changes to overall conductivity compared to some of the materials presented by Gomis et al..

Other considerations in using conductive additions in concrete

The use of any conductive addition or substitution in concrete will almost inevitably increase the cost of the final product by some amount. Even in cases where the conductive material is inexpensive, it will add some amount of complexity to the supply chain and manufacturing process. A detailed assessment of the increase in cost resulting from the use of conductive additions or substitutions in construction is out of scope for this review, but it is instructive to compare the off-the-shelf price per kg of some of the materials suggested by Pan et al., Gomis et al. and others. Pricing for a selection of materials is given by Table 3.1.

Table 3.1: Example pricing of materials proposed for increasing the conductivity of concrete. All prices exclude UK VAT.

Material	£/kg	Source
Carbon Black	£5.30/kg	5kg @ £26.66, Mistral Industrial Chemicals
Aluminium Powder	£12.10/kg	5kg @ £60.50, Easy Composites
Graphite Powder	£11.65/kg	2.4kg @ £27.95, Easy Composites
Carbon Fibre Powder	£18.29/kg	17.5kg @ £320.00, Easy Composites
Carbon Nanofibers	£3800/kg	0.025kg @ £95, Sigma-Aldrich
Carbon Nanotubes (multi-walled)	£25700/kg	0.01kg @ £257.00, Sigma-Aldrich

A number of types of carbon nanotubes are available; Gomis et al. specifies the multi-walled variety. Clearly there is large variation in the quantities of materials being sold, and as with any purchase of material the cost per kilogram will depend in part on the quantity being procured. However it is clear from the

findings shown in Table 3.1 that the variation in price among conductive materials is substantial, and in particular the large resistivity reductions from the use of carbon nanofibres and carbon nanotubes reported by Gomis et al. come at a large financial cost.

Some conductive additions undoubtedly pose additional manufacturing challenges relative to structures using conventional concrete. CFP and GP as well as carbon black all have some level of additional health risks associated with them relative to typical concrete components, which may need to be mitigated through the use of additional PPE. As mentioned above, conductive additions in a powder form will pose some level of risk to electrical equipment, requiring them to be dust-proofed to a higher standard than otherwise necessary. Finally, conductive additions will in some cases affect the workability of the concrete, for example the addition of graphite powder has been found to cause a large decrease in workability requiring further additions to the mix (Wang, D. et al., 2019). Each of these effects will vary in scale depending on the material used, which will have to be accounted for when deciding on the material to use.

Conductive additions and substitutions may have some implications for concrete strength. Chen et al. (2017) tested the compressive strength of four concrete mixes containing varying amounts of 6mm carbon fibres and graphite at 7 and 28 days hydration, and found an increase in strength related to the quantity of carbon fibres. No mix containing graphite without the carbon fibres was tested, but increasing the quantity of graphite powder does not appear to have an effect of compressive strength from the published results. Similarly, Shengxi et al. (2011) found increasing the quantity of steel fibres in the concrete mix to increase its compressive strength. (Xu et al., 2015) performed compressive and flexural strength tests on cement paste containing multi-walled carbon nanotubes, and found a 6.25% increase in compressive and 7.5% increase in flexural strength at 28 days from with the addition of 0.025 weight % of the carbon nanotubes, and further strength increases with higher quantities. These results are consistent with the concept of fibre-reinforced concrete, in which fibres bonded into the concrete matrix lend extra strength. Conversely, Liu et al. (2019) found that increasing the weight % of graphite powder decreased both compressive and tensile strength. Liu et al. proposes reduced frictive resistance to force between graphite particles and the rest of the concrete matrix, low bond strength between graphite particles

and cement, and the necessary increase in water quantity as reasons for this.

The effect of any conductive addition or substitution on the durability of a structure built with it is of course of critical importance. Carriço et al. (2018) examined the durability of concretes reinforced with multi-walled carbon nanotubes, some with weight % 0.05 and one with 0.1%, according to a number of criteria. These included the absorption of water (and thus vulnerability to freeze-thaw cycling), resistance to carbonation, and resistance to chloride penetration. The carbon nanotube reinforced concrete performed better than reference concrete according to all of these criteria, though the authors note that in some cases the performance improvement was modest. Xin et al. (2012) reports improved resistance to freeze-thaw cycling in carbon fibre reinforced concrete. A literature search found no reporting on the durability of graphite powder infused concrete, though in a related development Miguel-Ángel et al. (2016) did find it feasible to use a graphite powder infused cement paste as a coating on a concrete structure to facilitate the application of anti-corrosion treatments. Abbas et al. (2015) found that increasing quantities of steel fibres in ultra-high performance concrete generally improved durability, although Frazão et al. (2015) did not report significant changes to durability characteristics when changing the dosage of steel fibres in self-compacting concrete.

There is increasing demand for the design of structures to account for what will happen when they reach the end of their useful life, in large part due to concerns surrounding lifetime carbon emissions(Alwan et al., 2017). It is necessary to consider the effects of any conductive addition or substitution on the process of deconstruction of the structure, and the potential for recycling its components. This is of special interest when conductive materials have been used, simply due to the extra cost of manufacturing. Kunieda et al. (2014) investigated the potential for recycling of fibre-reinforced concrete, including steel fibre-reinforced concrete. The typical method for recycling concrete involves crushing it and using it to replace aggregates in the concrete matrix. Kunieda et al. crushed concretes reinforced with steel and polymer fibres, and found that the size of the fragments produced by the crushing reduced with an increase in fibre content. It should be noted that this relationship was only observed in the polymer fibre cases since a single steel fibre-reinforced concrete was crushed, but there is no reason to expect that the steel fibre would cause a different outcome. They also

performed water absorption tests, which they explain are useful for evaluating the quality of a recycled aggregate, which returned an outcome of "low quality" in all cases. They did not attempt to produce any concrete using the recycled aggregates and there does not appear to be any further research on the topic. A literature search found no research into the use of other conductive concretes as recycled aggregates.

3.3 Cracking in concrete

Cracking in concrete is often unavoidable. There are a number of mechanisms by which cracks form, and those cracks may be a threat to structural durability depending on a number of factors.

Concrete is far stronger in compression than in tension. Tensile cracks are therefore expected and not necessarily a great concern. A crack caused by compressive loading is much more likely to be a serious problem.

This section gives a brief overview of the causes, effects, and classification of cracks, as well as the development of Self-Healing Concrete (SHC) which originally motivated this project.

3.3.1 General causes of cracks

Cracks in concrete occur either before or after hardening, with generally different causes in each case.

Cracks occurring before hardening are generally caused by shrinkage of the concrete, because of either the thermal environment or loss of liquid water as the concrete hydrates. These risks can be mitigated somewhat by site practices ensuring an optimal curing process and protecting the concrete from thermal extremes.

Post-hardening cracks may have a wider variety of causes. As with pre-hardening cracks, shrinkage is a potential cause. Otherwise post-hardening cracks are generally caused by the environment of the structure, through chemical attack or thermal stresses, or by inadequate design for mechanical loading.

These causes may also compound each other. For example a pre-hardening shrinkage crack may provide a means of ingress for water, leading to expansion

from freeze-thaw cycles. The Concrete Society (2010) provides a detailed treatment of the various classifications and causes of pre and post-hardening cracks, with a general "family tree" reproduced in Fig 3-4.

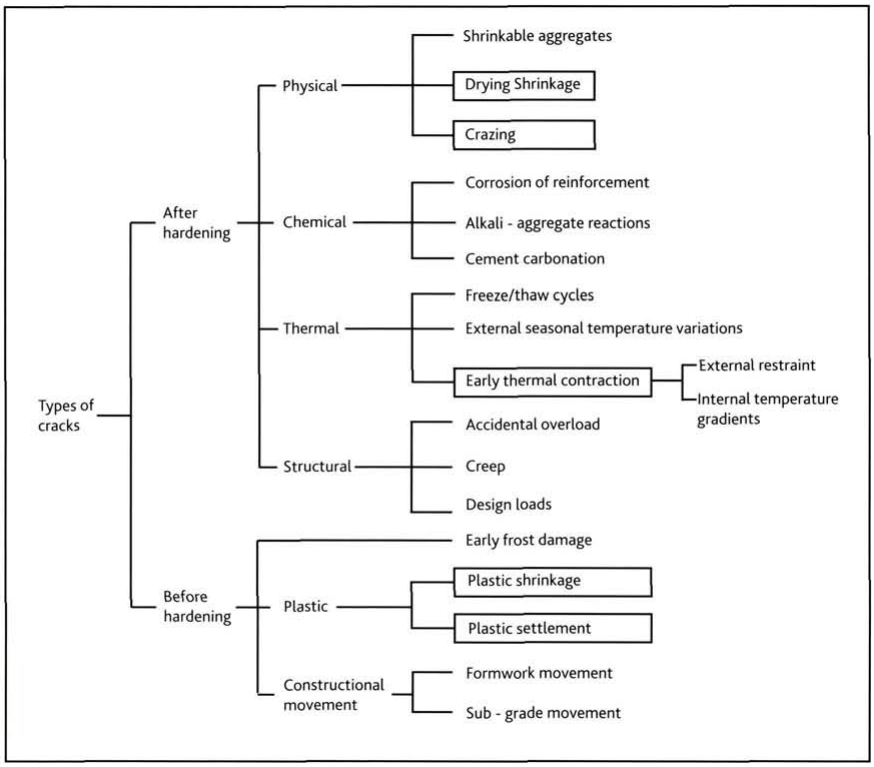

Figure 3-4: Categories of cracks in concrete. From The Concrete Society (2010).

Crack size and location is related in all cases to the loading of the structure and the design of its reinforcement; see The Concrete Society (2010, Section 3.2) for more detail on this.

3.3.2 Effects of cracks

Some level of tensile cracking is almost inevitable in any concrete structure, and this is often accounted for at the design stage. The majority of these cracks are likely to be quite small and structurally harmless. When a crack in a concrete element is problematic, it is for one of the following reasons:

- The crack is considered aesthetically unacceptable.

- The crack immediately compromises the load bearing capacity of the element.
- The crack is liable to fill with water and the structure is in an environment that makes it vulnerable to freeze-thaw cycles.
- The crack allows the intrusion of substances which can chemically attack the steel reinforcement or cement.

The presence of cracks may also indicate problems with the concrete rather than specifically being a problem. For example the presence of shrinkage cracks can be the result of improperly cured concrete. Stress cracks will form due to failure to either calculate or design for the loads on the structure. In these cases the crack does not necessarily have a negative effect, but the underlying cause indicates a problem with the structure.

Cracks that are merely ugly obviously require no specialised techniques to identify. A crack compromising load bearing capacity of an in-use structure is very unusual and will only occur as a result of serious errors in the design or construction process. Dangers of freeze-thaw cycles and chemical attack can also be present in the absence of cracks; cracking exacerbates the issue. In the case of chemical intrusion, the concerns surround chlorides and sulphates attacking the cement paste. If a crack is present this exacerbates the problem, making it more likely that reinforcement may be exposed to attack.

3.3.3 Existing methods for classifying cracks

Cracks formed after hardening are generally more serious in themselves, as well as indicating problems with the structure since this type of crack is often the result of an inadequacy of the design for the loads or environment that the structure is experiencing. Therefore being able to distinguish between pre and post-hardening cracks is potentially valuable.

These is not currently any accepted way of describing cracks other than by their observed width on the surface of the concrete, a measurement which may not be representative or repeatable (The Concrete Society, 2010, p.13), so categorisation is still done by visual inspection and surface measurement. There is also no recommended method for measurement in the building codes. This means

that there is a degree of subjectivity to any crack classification. An experienced engineer may have the knowledge to identify types of crack from its location and appearance, particularly with some information about locations of features such as joints or reinforcement. The permissible size of a crack depends on the risk factors for the structure generally, and on the location of the crack on the structure. Cracks are assumed to be a potential risk to durability if they are more than 0.3mm wide, and watertightness is also assumed based on crack size as well as concrete thickness and water depth.

There is a preference to err on the side of caution in cases when the danger posed by a crack is uncertain. More sophisticated methods for classifying cracks have the potential to assist in the characterisation of cracks and the risks they pose, so that engineers can make informed decisions on ignoring, repairing, or discarding concrete structural elements. Because of the limitations of methods for classifying cracks, there is a tendency to misidentify harmless cracks as structural ones, and discard perfectly usable concrete (The Concrete Society, 2010, p.1). This is one potential use for Electrical Property Imaging (EPI) and other NDT technologies as they provide more information than a visual inspection of the crack at the surface.

3.3.4 Self-healing concrete

Considerable research activity surrounds SHC, which is a potential method for mitigating the risks of cracks without requiring human attention. (De Belie et al., 2018) reviews the numerous approaches for producing these concretes. Seven examples of cracks produced to study a bacteria based SHC and given 165 days to heal by Alazhari et al. (2018) are shown in Fig. 3-5.

As described in Section 1.1, there is a concern that with many of these methods the SHC mechanism is most effective at the surface. Most of the work that De Belie et al. cite shows results photographically (one exception is in J. Wang et al., (2014), whose work performing X-Ray CT on SHC is discussed in Section 3.4.1) and the possibility remains of subsurface voids not visible from the surface being created by the process as shown in Fig. 1-1, which was one of the original motivations for this work.

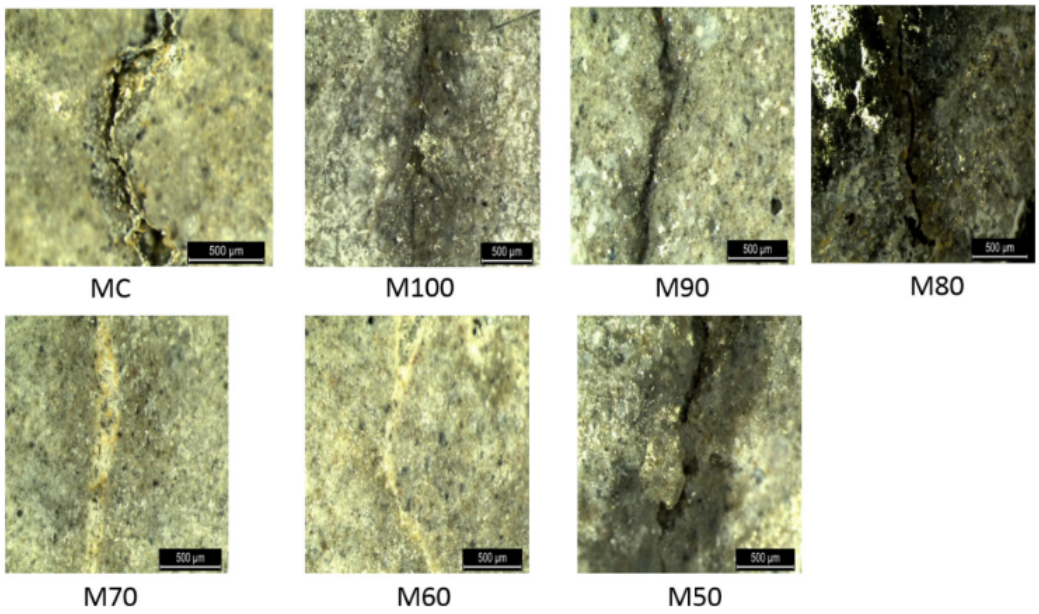

Figure 3-5: Cracks in SHC after 165 days healing. Different cracks contained different concentrations of bacterial spores. MC and M100 are controls and show no healing. M50, M80 and M90 similarly show no healing. The SHC has healed successfully in M60 and M70. From Alazhari et al. (2018).

3.4 Integrity assessment of concrete

In situ integrity assessment methods for concrete can be divided into two broad categories. Here NDT is used to mean the assessment of some aspect of the structure at a single point in time. This category includes many of the more established assessment methods, such as the use of rebound hammers. SHM is used to mean the long-term assessment of a concrete structure, possibly using either integrated sensors or some combination of sensors and modifications to the concrete material.

It is difficult and unnecessary to make solid distinctions between these two categories - for example NDT performed repeatedly over a longer period may be described as SHM - but this section groups assessment methods into one or the other for the sake of clarity. This section concentrates on methods for assessing cracking, methods that use measurements of the electrical properties of the structure, and methods involving modification to concrete.

3.4.1 Non-destructive test for concrete

NDT for concrete is, unsurprisingly, an area of considerable research activity. In addition to crack assessment, NDT methods for assessment of hydration levels and moisture content, mechanical properties, and even measuring mechanical stress have been investigated.

The majority of work in concrete integrity assessment has been in NDT on structures not designed with features to facilitate assessment. Detailed information on the internal configuration of structural elements cannot be assumed in these cases, as structures may be old and records may be unavailable. NDT equipment is necessarily more versatile than that designed to interface with a more co-operative structure.

Covermeter

A cover meter is used to determine the distance between rebar and the concrete surface. The cover meter is usually a handheld device, operating by inducing and measuring either eddy currents or a magnetic field in the reinforcement (The Concrete Society, 2000, p.38).

The cover meter is a well established tool which when used properly gives the location of reinforcement with a useful degree of accuracy. However it is only really useful for quality control and in cases where records of the structure's design and construction are unavailable, and doesn't provide information about the condition of the structure.

Rebound hammer

A Rebound or Schmidt hammer is used to determine concrete strength (Gorse et al., 2012, p. 342) by propelling a spring loaded mass into the surface of the concrete and measuring the distance rebounded by the mass. This can be used to infer the energy absorbed by the concrete surface, which can then be used to indicate hardness, resistance to penetration, and compressive strength of the concrete under test.

The rebound hammer is another standard tool, also useful for quality control. Information from surface testing is only applicable to around 30mm depth, but this information can be useful in itself and empirical relationships between the

properties being measured and others may be developed. Testing at multiple sites can give an indication of uniformity across the build (The Concrete Society, 2000, p.37) .

Thermography

Thermography is the use of temperature sensing equipment to detect areas of different temperature on the surface of concrete. If the whole surface is subject to the same heating, it can be concluded that temperature differences are the result of discontinuities, including air voids, within the concrete. This method can be used to find the general area of discontinuities but not the size or depth. The nature of the discontinuity cannot be determined beyond some inference from the relative temperature of the region. Surface quality and weather conditions may also have a strong effect on the outcome of measurements and affect the usefulness of the technique (The Concrete Society, 2000, p.42).

Electrical property measurements

Measurement of the electrical properties of concrete has been used as a method for assessing various characteristics related to its structural performance. In these cases electrical property measurements are recorded and used to estimate some other characteristic, typically by comparing those measurements with established data.

Dérobert et al. (2017) has examined using resistivity and capacitance measurements to evaluate levels of chloride contamination in otherwise undamaged concrete. Resistivity and capacitance measurements, as well as a commercial Ground Penetrating Radar (GPR) system, were applied to three different concretes. The concretes were tested for strength and porosity, and then different concrete samples were contaminated to different degrees using a sodium chloride/water solution. Given proper calibration, these measurements were found to be very sensitive to chloride concentration and reasonably sensitive to porosity.

Fares et al. (2016) studied using capacitance measurements from a relatively small number of electrodes to generate a capacitance profile within a material using the same mathematical regularisation principles employed by EPI. This information can be used to infer the quantities of water and ionic substances

within the concrete, which in turn can indicate the level of corrosion of reinforcement and vulnerability of the structure to freeze-thaw cycles as well as other health problems. By setting up a capacitive circuit and measuring its resonance frequency the capacitance of the concrete under test is inferred. Use of different electrode pairs, which can perform this measurement incorporating different depths of concrete, a permittivity profile of the concrete can be produced. This appears to be reasonably sensitive to changes to the permittivity at depths of up to 100mm.

Forde et al. (1981) measured the resistivity of various cement and concrete mixes during the hydration process, finding that resistivity is heavily influenced by factors of the mix design. If this information is known then the changes in resistivity can be used to estimate the stage of hydration of the concrete being measured, which is itself a good indicator of mechanical properties.

Ground penetrating RADAR

GPR is a technique commonly used in geophysics which has also been proposed for inspection of concrete, for example by Amer-Yahia and Majidzadeh (2012). In this technique radar waves are transmitted into the body being measured, where changes in the electrical properties cause the waves to be reflected. The reflected waves are measured by the equipment, and using the change in one of a variety of wave characteristics depending on the system, a distance to the material interface can be inferred.

In the case of concrete NDT, the interface would be concrete/air or concrete/metal. Amer-Yahia and Majidzadeh's work focused on the potential of using GPR for verifying that insulated concrete foam, which is difficult to evaluate using other methods because of its insulation, is setting correctly without voids. Amer-Yahia and Majidzadeh had success in detecting most voids, but found that the method was relatively poor at detecting voids smaller than 20mm, which limits its usefulness in crack characterisation. The output of the GPR is also not easy to interpret, and could cause voids near to rebar to be missed.

Dérobert et al. (2017) assessed the use of GPR for measuring chloride contamination and compared it to the efficacy of electrical property measurements. GPR was found, along with the measurement of resistivity and permittivity, to be very sensitive to chloride content.

X-Ray

X-Ray imaging is a well known technique often used in medicine and other fields. In X-Ray imaging, X-Rays are projected through an object and captured by a detector on the other side. Different features in the object will absorb different amounts of X-Ray, and this will be represented in the intensity captured by the detector. In X-Ray Computed Tomography (CT), the X-Ray projector is moved around the object and many images taken, with a 3D representation of the object being reconstructed from the results of all of the projections.

X-Ray CT is a mature imaging method, and it produces very high resolution 3D images, much higher than anything achievable using EPI methods. X-ray CT has been used in proving self-healing concrete performance (Wang, J. et al., 2014) as well as internal imaging of a concrete cylinder during loading (Yuan, Q. et al., 2015). Images produced in both cases are extremely detailed and very good for the purpose of assessing crack healing. An example is shown in Fig. 3-6, from J. Wang et al., (2014).

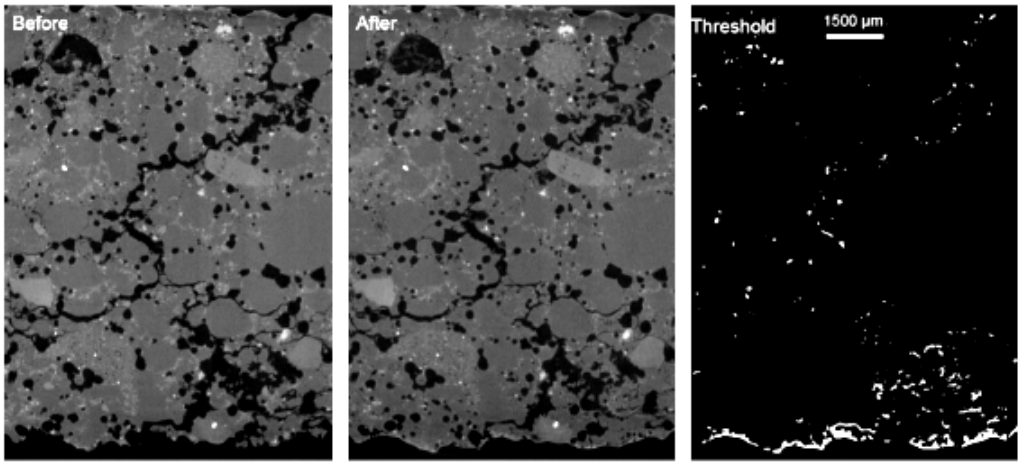

Figure 3-6: X-Ray CT showing before and after self-healing has occurred. Bottom of the image shows sample surface. From J. Wang et al., (2014); this image has had brightness and contrast increased from the original to aid legibility when printed.

However, X-Ray imaging has disadvantages for application on concrete. X-Ray equipment is extremely expensive to buy and operate, with EPI equipment being much cheaper. 2D X-Ray imaging also requires access to both sides of the object being imaged, and X-Ray CT needs access to the entire outside of the

object. This is in contrast to EPI, which can operate on an open domain. These requirements also limit the permissible sample size, with J. Wang et al's cylinders being 8 mm wide and 10 mm tall.

Ultrasound

Ultrasound operates on a similar principle to GPR, in that high-frequency sound waves are transmitted into a body and returning waves measured. A wide range of approaches have been taken in using ultrasound for concrete NDT.

Aggelis et al. (2012) used ultrasound transducers from a single side of concrete to assess internal cracks. Steel fibre-reinforced concrete samples were cracked on one side using a three-point bending machine. Sensor pairs were applied to the non-cracked side of the samples. By sending a surface wave (which will penetrate down into the concrete to some degree) from one sensor to the other and measuring the wave velocity and amplitude the damage from a crack can be assessed. These measurements appear to be consistently sensitive to the presence of subsurface damage close to the surface. However the technique does not provide more information about the crack, and is limited in the effective depth.

Demčenko et al. (2016) used ultrasound to measure the layer thickness of concrete. The stated application of this is the assessment of deteriorated layers that occur in concrete buried in certain soil environments. Layer measurement like this is a similar application to the work of Fares et al. (2016) using capacitance measurements. The ultrasound measurements can provide high spatial resolution even when three layers are present.

Kozlov and Kozlov (2015) published a review paper on the use of ultrasound for concrete NDT. They suggest that the composition of the concrete has a strong influence on the optimal frequency range and configuration for ultrasound imaging. Rucka and Wilde (2015) applied ultrasound to concrete blocks while subjecting them to a bending test. They were able to monitor the propagation of cracks from the concrete surface. However their experimental setup involved ultrasound transducers permanently installed in recesses in the concrete, which acted as stress raisers during the bending test and ensured that cracks occurred directly over the transducers. The careful preparation required is limiting for in situ health monitoring as cracks may occur anywhere on the surface of the concrete.

A commercially available device, the "A1040 Mira" (Acoustic Control Systems, 2014), is marketed for concrete inspection. It appears that no references to the device exist in academic literature, and as a device intended for a niche application no independent assessment of its performance could be found. The manufacturer claims to be able to provide imaging at depths of up to 600mm. It is unclear what resolution the device can provide.

3.4.2 Structural health monitoring for concrete

SHM refers to the monitoring a structure over a long period of time. This may be done by integrating sensors with the structure, modifications to the properties of the concrete itself, or simply by repeated NDT measurement. This section deals with the first two subcategories of SHM methods. Simple SHM methods, such as the strain gauge, have been in use for many years, but the use of more complex systems of integrated sensors and the development of concrete with properties facilitating assessment is more recent. Structures with health monitoring features are often described as being "self-sensing", and concrete which has been made with intrinsic modifications to facilitate health monitoring may be called "self-sensing concrete". Han et al. (2015) gives a good overview of methods of SHM for concrete.

The majority of work done on long-term in situ SHM for concrete has used sensor equipment integrated into the structure. Incorporation of instrumentation in structures as they are built could provide a quicker and more reliable method of inspection of the structure than the more traditional methods described in section 3.4.1. "Integrated" here refers to methods of SHM where sensors would be attached to the structure for its whole service life.

Mounting sensors in the structure during construction potentially gives more freedom in configuration and arrangement, which is especially advantageous in EIT where contact impedance and model accuracy are important. EIT could be applied in this space if the use of integrated sensors becomes more widespread.

Xue et al. (2014) determined that it is feasible to monitor the health of pavement using an integrated sensor system. They used a variety of sensors, along with a wireless data logger, mounted under a section of road which was in use by vehicles. This appears to be a particularly hostile operating environment, and

the system performed well. Niederleithinger et al. (2015) successfully embedded ultrasound sensors in concrete during lab experiments. They have also embedded the same sensors in in-use structures, but have not yet published their findings from that work. Most of these sensors are more sophisticated, and presumably more fragile, than the electrodes which would need to be embedded for EIT.

Strain gauges

Measurement of strain can be useful for assessing movement in structures, or determining mechanical properties of a material or structural element in the lab. Strain gauges used for SHM use a number of mechanisms.

In a mechanical strain gauge two points on the gauge are securely fastened to the structure, and allowed to move independently of each other. Strain is given by the distance between the points, which may be measured by a variety of methods giving different levels of resolution. For example visual measurements using a standard or vernier scale, or electronic measurement with equipment such as a linear encoder. Electrical strain gauges use a specially shaped electrical resistance element bonded to the surface and connected to a circuit measuring its resistance. Changes to the shape of the element caused by structural strain alter its resistance, and strain is inferred from this measurement.

Strain gauges allow the monitoring of crack size over time. Strain gauges can be installed for low cost if a simple mechanical type is permissible. In a crack monitoring application, this is likely to be the case since a resolution of better than 0.1 mm would not be necessary. Lifespan principally depends on the adhesive used, and how effective it is under the conditions that the device is installed in.

Chew et al. (2018) used fibre optic strain gauges to measure strain in a concrete beam subjected to a bending test. These were found to provide a very high degree of precision, much greater than necessary for crack monitoring. This type of sensor is also presumably much more expensive and fragile than the more conventional types, and as such is best suited for determining mechanical properties in a lab.

Digital video monitoring

Computer vision techniques can be used for measuring strains, including those induced by cracking. This is commonly employed in laboratory experiments assessing the mechanical properties of a material, such as bending and compressive tests.

A number of researchers have also investigated the practicality of using video monitoring on actual structures (Feng and Feng, 2018) and found them to be workable for the measurement of structural parameters such as frequency response characteristics and deflection under load. Monitoring of surface cracks seems to be an obvious possibility, but Feng and Feng also list instances of researchers using the displacement and frequency characteristics along with computational simulation methods to detect non-visible damage to the structure.

This technology could provide information on the health status of certain types of structure that exhibit significant deflections under load, such as high-rise buildings and bridges, with relatively few sensors. However once a problem is detected using this method it still needs to be diagnosed, requiring inspection or other SHM equipment. For smaller scale monitoring where a single camera would replace fewer sensors, relatively extreme bandwidth and computation requirements (even for basic 2D strain measurements) put the technology at a disadvantage. In all applications the system is sensitive to weather conditions, movement of the camera and any kind of damage to the lens.

Piezoelectric transducers

The piezoelectric effect is a phenomenon observed in piezoelectric materials in which these materials generate some amount of electrical charge when a stress is applied. If the charge is measured then the stress can be inferred. Piezoelectric materials also exhibit the reverse piezoelectric effect, in which the application of an electrical charge results in mechanical force.

Tseng and Wang (2004) used a network of piezoelectric transducers bonded to concrete elements to detect damage in a concrete beam. By using a transducer to produce and then measure vibrations in the beam, simulated damage was detected and the distance of the damage from the transducer inferred. Tseng and Wang suggest that this could be used to detect damage at up to 500mm from the

transducer. This method can only track changes occurring after the transducer has been attached, but this is achievable for a structure designed with SHM in mind. Kim et al. (2014) used embedded piezoelectric sensors to monitor concrete strength during the curing process. This method was successful in estimating the strength of the concrete, but it is not known how the shape of the concrete element, or features such as reinforcement and voids would affect the accuracy.

Acoustic Emissions monitoring

Acoustic emissions monitoring involves listening for sound being produced within a body, typically in the ultrasound frequency range (Prem and Murthy, 2017). Receivers used in active ultrasound applications can therefore be used.

Acoustic emissions are produced by the development or propagation of a crack. The method can be applied similarly to various structural materials including non-cementitious ones. By using multiple sensors the location of the emission can be estimated.

This is a method for determining that cracks are forming. It is less useful for locating and characterising cracks. While it has been successful in the lab, in a functional structure it is less likely to be useful because of the risk of false positives

Intrinsic self-sensing concrete

"Self-sensing" concrete is concrete where composition has been altered in some way to facilitate health monitoring. These materials belong to the ever-growing constellation of "smart" concretes. A structure making use of self-sensing concrete must also incorporate equipment to provide an interface with the material; this may take the form of integrated sensors similar to those used in conventional concrete. In general self-sensing concrete is made by controlling the concrete's electrical properties using methods described in section 3.2.3.

Self-sensing is one of the main reasons for producing conductive concrete.. Happily, some of these modifications may also confer structural advantages. Wen and Chung (2003), Nguyen et al. (2014) and others have investigated the potential of fibre-reinforced concrete as a self-sensing material. Concrete reinforced with fibres made from materials including steel and carbon fibre has been studied for

purely structural purposes independently of self-sensing applications.

Nguyen et al. (2014) reports strong correlation between resistivity of Steel Fibre-Reinforced Concrete (SFRC) and the level of microcracking present in the material, and can therefore be described as self-sensing. Unlike strain-sensing in other self-sensing materials, resistivity correlation in fibre reinforced concrete may continue to operate after cracks have appeared if there is still continuity in the fibres.Nguyen et al. also found that the fibre type does have an effect on the change in resistivity that needs to be considered. This would cause difficulty in instances where details of the construction are not known. Chen et al. (2017) also achieved good correlation between strain and resistivity in conductive concrete made using carbonaceous powders.

3.5 EIT for Concrete

Relatively little work has been done on using EIT specifically for concrete. Most of the work that does exist can be divided into two categories, with some work overlapping. Firstly some work is concerned with either imaging of internal voids, cracks, and discontinuities. Distinguishing metal reinforcement has been less of a priority. Secondly, other work investigates moisture transit through cementitious materials, which is particularly interesting from the perspective of durability and chemical attacks as discussed in Section 3.3.2. Of course there is also some work which does not fit into either of these categories.

The use of EIT and Electrical Resistance Tomography (ERT) in civil engineering is not exclusive to concrete. ERT has been used for geophysics applications, such as the work by Martínez-Moreno et al. (2018)

EIT and ERT are often used interchangeably in scientific literature. The distinction is discussed in Section 2.2.1. Here the terms are used to remain consistent with the publications being described.

Hou, T. C. and Lynch (2008) studied using EIT for detecting crack damage and strain fields in fibre reinforced concrete samples using fine sand as an aggregate. Measurements were taken using standard current generation and data acquisition equipment, as opposed to a dedicated EIT machine. This can result in noisier readings than would be obtained with an EIT machine but this can be addressed by taking large numbers of measurements and averaging them. Little

detail is provided on electrode contact, but it seems to use colloidal silver paint similarly to (Hallaji et al., 2015). Electrodes were attached to concrete blocks during tensile and bending tests. Conventional strain gauges were also used as a comparison for the results. Imaging of strain fields and cracks produced good results. However, in the strain field imaging case it seems that experiments with fine aggregate may not be representative of results that could be expected when using more typical coarse aggregates. This is because on the small scale, the strain will distribute evenly when using the sand aggregate. With a coarse aggregate the majority of the strain will occur in the cementitious part.

Karhunen et al. studied the feasibility of using EIT for crack detection in early hydration concrete, and obtained good results imaging plastic inclusions and cracks in slabs (Karhunen et al., 2010a) and cylinders (Karhunen et al., 2010b). These results were achieved using Time Difference Electrical Impedance Tomography (TDEIT), with a KIT4 EIT machine as described by Kourunen et al. (2009). Karhunen et al. was able to image inclusions with good position and shape accuracy, although it was found that reconstructing an accurate value for inclusion conductivity was difficult due to the model not accounting for the contact impedance of between it and the concrete. It would seem that due to the variety of conditions that may be encountered while imaging actual concrete, as well as the number of different types of inclusions that a user may be looking for, including contact impedance data in a model would be impractical. This could present a problem for distinguishing between different inclusions using time difference imaging. The difficulty in reconstructing conductivity did not lead to any difficulty in locating inclusions.

Ammari et al. (2014) performed numerical simulations of time difference imaging at different excitation frequencies on concrete. Their findings indicated that reconstructing the permittivity parts of an image as well as the conductivity might provide useful information. Additionally, their simulations showed that in time difference imaging the chosen excitation frequency affects the quality of the reconstruction. From the study it appears that in cases where inclusions both more resistive and conductive than the background are present, performing complex image reconstruction and using as large a range of frequencies as possible gives the best chance of distinguishing everything of interest in the body.

Hallaji and Pour-Ghaz (2014) applied a sensing skin to the surface of concrete,

and used it to image surface cracks. The skin was made of silver colloidal paint, and applied to concrete samples before cracks were induced to get difference measurements. This method avoids difficulties in making electrode contact, but requires the application of the sensing skin to the surface. The durability of the skin has not been studied.

Seppänen et al. (2017) returned to the sensing skin concept as a means of simultaneously imaging chlorides and surface cracks. This was achieved using a more sophisticated sensing skin consisting of two conductive layers separated by an insulating layer. Both layers were bonded to the concrete surface, and would be damaged by surface cracks in the same way as in Hallaji and Pour-Ghaz (2014). However, only the inner layer would have its conductivity affected by chlorides at the concrete surface. The resistive regions of the outer skin are taken to be cracks, and by essentially subtracting the inversion of the outer skin from the inner one the regions of chlorides are identified. The inversions show the shapes and positions of cracks and chlorides at the surface well, and the system distinguishes between cracks and chloride regions very well.

Smyl et al. (2018) continued with the use of sensing skins, using the concept to work on inversion algorithms. Algorithms in EIT tend to spatially smooth conductivity discontinuities, making the change in conductivity between two regions more gradual. This is not a problem in applications such as monitoring of moisture transit, where the conductivity distribution is generally quite likely to be smooth. But as Smyl et al. note, it poses a problem when attempting to accurately reproduce the shape of a crack, and a greater problem when attempting to accurately reproduce a number of cracks in close proximity. Performing imaging on the conductive sensing skin rather than on the concrete itself, their approach uses structural modelling to determine three "regions of interest" which are ranked by the likelihood of cracking occurring within them. This information is incorporated into the inversion by simply assuming that the conductivity change outside of the region of interest is zero. They also use an approach called non-linearised difference imaging, which involves reconstructing the conductivity distribution of the background simultaneously with the post-cracking distribution since the conductivity distribution of the background may be inhomogeneous. An isotropic Total Variation (TV) method (see Section 2.4.3) is used for regularisation, and it is this that provides the improvement in reconstructing sharp changes in con-

ductivity. The approach to inversion provides good distinction between cracks in a relatively complex (>12 distinct cracks) simulated crack network. The process was tested on much less complex crack networks in physical experiments, where it performs very well on crack orientation and location. In a real structure such clear imaging of surface crack networks would make it easier to distinguish between cracking and chloride ingress, so in a sense the system provides an alternative to the work of Seppänen et al. (2017). For subsurface cracks the ability to image in such detail is potentially very valuable, especially for monitoring the performance of SHC, since in this case a visual inspection of the crack network is not possible.

A sensing skin provides a means of concrete imaging which avoids some of the difficulties of directly imaging concrete which come from the resistivity of concrete and the problem of making good contact between the electrodes and the material. In most cases cracks will form at the surface of the concrete, and sensing skins do an excellent job of imaging those cracks. However the motivation for this project was principally the imaging of subsurface cracks that may form when using SHC (see Section 1.1) for which a sensing skin is not useful.

Reichling et al. (2014) were able to achieve good imaging of a bar of reinforcement in a concrete beam by using a single line of electrodes on one side of a concrete beam, by using a resistivity meter designed for geophysics applications. This is a rare example from the literature the open domain capability of EPI being applied to concrete. The system was not tested on reinforcement deeper than approximately 50mm.

Hallaji et al. (2015) used EIT to monitor moisture flow through a block of cement paste for different moisture sources. The cement block is intended to be particularly porous, and electrodes are made of colloidal silver paint on the edges of the block. These are then attached to the EIT device using bolts screwed through a frame surrounding the block. The EIT in this case was performed on a square body, and the progress of moisture through the block was also tracked visually and with neutron radiography imaging for comparison. The resistivity reconstructions in this case compare well to the other methods used to track the moisture. One of their results is shown in Fig. 3-7.

Smyl et al. (2016) continued the work of Hallaji et al. on monitoring of moisture transit by using 3D EIT to monitor the absorption of plain water and

water containing iohexol, a substance used to improve contrast in radiation based imaging. The EIT results were compared to X-Ray CT images. Though as expected the spatial resolution of the 3D EIT is much lower than the X-Ray, EIT is much more sensitive to smaller changes to fluid concentration.

B.S. Huang et al., (2016) used four cylinders with different quantities of conductive additions, and found that decreasing the resistivity of the concrete resulted in better ERT images.

Suryanto et al. (2017b) used ERT to image the distribution of moisture in a concrete cylinder. The cylinder had some surface damage from demoulding. An automatic system was used to take measurements over 20 hours while water was absorbed by the cylinder. The ERT measurements showed the water behaving moving into the damaged region at a higher rate, which is consistent with expectations.

Capozzoli and Rizzo (2017) attempted to locate steel, aluminium and plastic pipes as well as damage in a simulation of a segment of road. In addition to an ERT system made made from a geophysics resistance measurement device, GPR was also used. This was another example of ERT being used on an open domain, and as in Reichling et al. (2014) the depth at which the ERT could resolve features was limited. The GPR worked on features at depths of around 1000mm, whereas the ERT was functional down to around 240mm. Some allowances had to be made for the impedance of the materials; ERT was not successful when electrodes were applied to asphalt but it did work when used on concrete.

It appears that more experimental work has been done on monitoring of moisture transit than on crack detection and characterisation. Naturally the requirements of the application tend to inform the choice of algorithm. Algorithm development is generally done by researchers with mathematical rather than engineering backgrounds, and typically takes individual requirements (such as the time required to arrive at an inversion, or reconstructing accurate conductivity values) of some application and provides improvements on those lines. Imaging of moisture transit and cracks have different requirements, with the biggest difference being moisture transit requiring smooth conductivity transitions and cracks requiring sharp ones. This has led to crack imaging work favouring TV, whereas moisture transit work tends to use Tikhonov regularisation (TK-R) or similar inversion algorithms.

3.6 Conclusions

Cracking in concrete is an area in which NDT and SHM techniques could serve a useful purpose by providing more accurate and consistent methods of classification, to give engineers a better idea of the implications of a particular crack.

EIT may not be an obvious technique for use in concrete due to the high resistivity of the material, but given specialised equipment and the increased interest in self-sensing concrete it could be a valuable tool for not only crack detection and assessment but also monitoring of moisture transit and chemical attack.

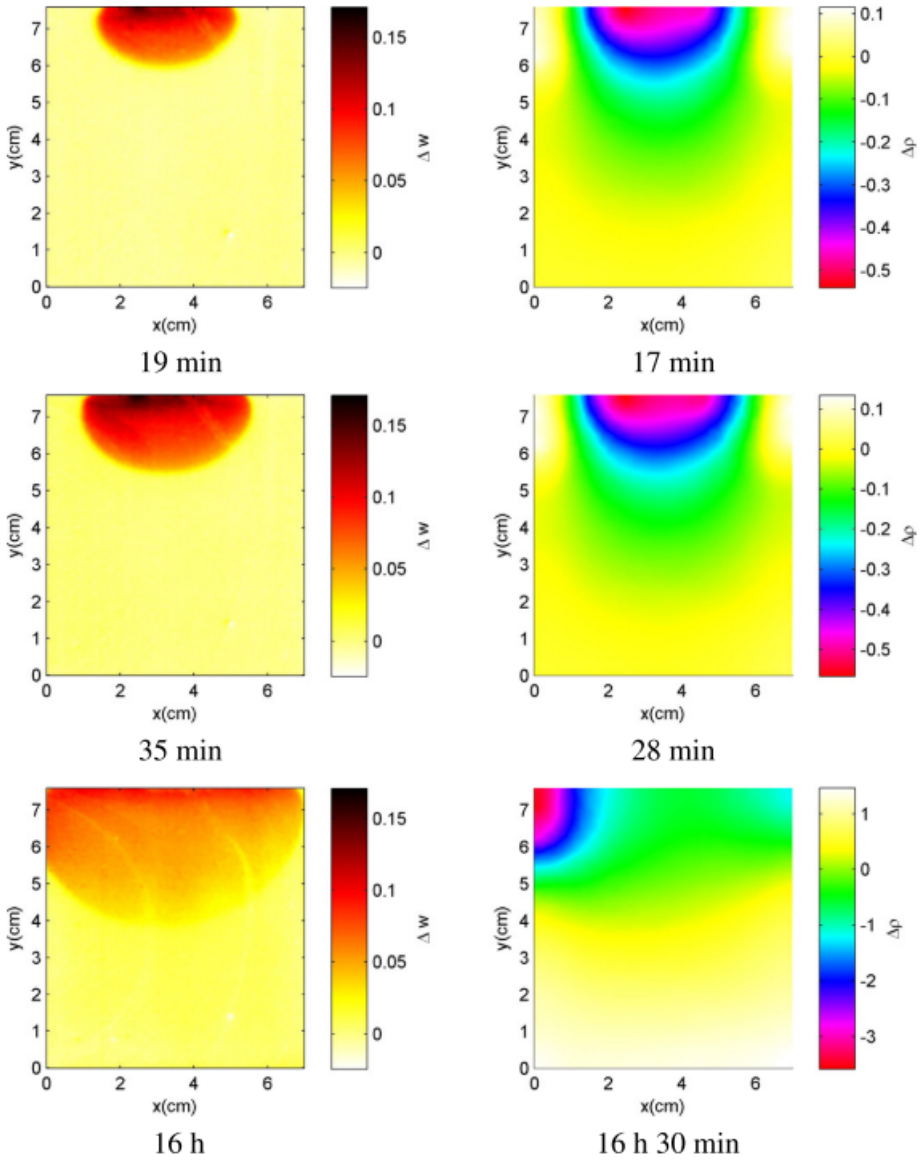

Figure 3-7: Neutron radiography (left) and EIT imaging (right) of moisture transit through a square cement paste sample using a water source 1/3 the width of the sample in the top centre of the block. From Hallaji et al. (2015).

4 | Experimental programme, equipment, materials and methods

This chapter describes the programme of work and gives information on the contents of the later chapters. It also serves as a reference on the equipment, materials and methods used throughout the project.

Chapters 5 and 7 presented in the traditional format, and their associated methods are given in this Chapter in Sections 4.3 and 4.5 respectively.

Chapters 6 and 8 are presented in journal paper format and as such contain their own methods sections. Because this chapter is meant to serve as a reference, these methods sections are also presented here as they are in the papers, with some additional information included where appropriate, in Sections 4.4 and 4.6 respectively.

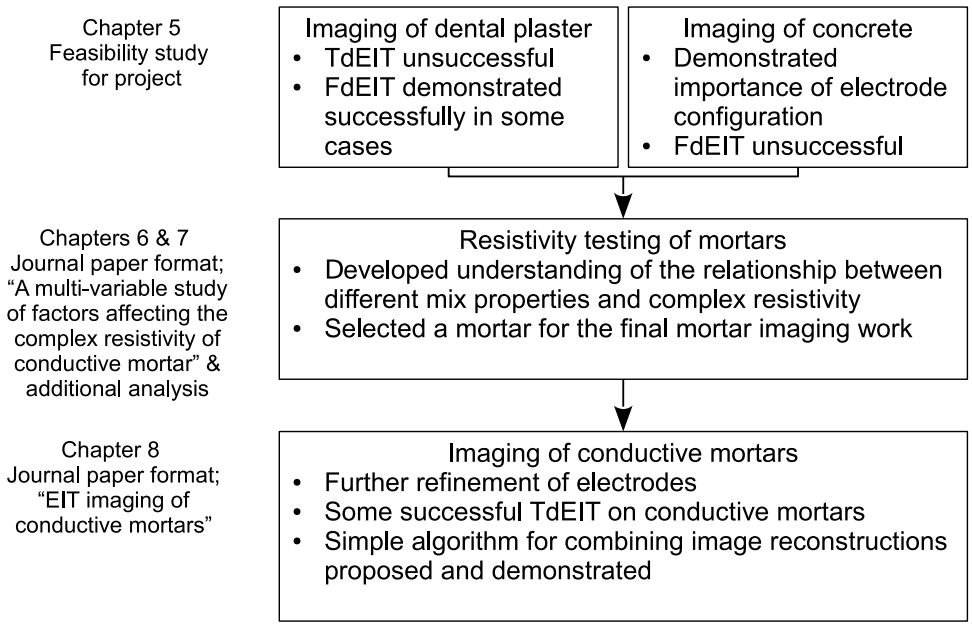

Section 1.3 gives a broad overview of the decisions about direction that were taken during the project, whereas this chapter describes the methods used to achieve the objectives.

4.1 Summary of experimental work undertaken

The project had three objectives, given in Section 1.2 and restated here. Each objective was achieved through experimentation.

4.1.1 Objective one

Assess the feasibility of using Electrical Impedance Tomography (EIT) on concrete using the available equipment

Firstly, EIT was performed on some dental plaster cylinders manufactured specifically for the project. Plaster was used as it was expected to be less challenging to work with than concrete, while being more representative of cementitious materials than working on a saline phantom. This work is described in Section 4.3.1 and its outcome is described in Section 5.1.

Following the work on dental plaster cylinders, EIT was attempted on concrete cylinders. This work is described in Section 4.3.2 and its outcome is described in Section 5.2.

These two experiments taken together fulfilled objective one.

4.1.2 Objective two

Investigate the electrical properties of concrete containing conductive additions, and thus determine how best to produce a concrete that can be imaged using the available equipment

Objective two was fulfilled though a comprehensive experiment examining the effects of conductive additions and other aspects of mix design on mortar resistivity, described in Chapter 6 which presents the paper "A multi-variable study of factors affecting the complex resistivity of conductive mortar". Methods for this work are also reproduced in Section 4.4. Some further work on understanding the electrical properties of the mortars produced for that paper is described in Section 4.5 with outcomes in Chapter 7.

4.1.3 Objective three

Develop a methodology for performing EIT imaging on this conductive concrete with the available equipment

The final objective was fulfilled through EIT imaging work on conductive mortar cylinders produced using the knowledge gained from the completion of objective two. Four cylinders were produced, three of which had resistive inclusions with one homogeneous to use as a background. The imaging study on the conductive mortar is described in Chapter 8 which presents the paper "EIT imaging of conductive mortars". Methods for this work are also reproduced in Section 4.6.

4.2 Electrical equipment

Two electrical instruments were used in this research. All EIT measurements were recorded using a KHU Mark 2.5 EIT machine. Impedance measurements including all of those used for the mortar resistivity experiment as well as some supplemental work were done using the Agilent E4990A impedance analyser.

4.2.1 KHU Mark 2.5 EIT machine

All EIT measurements were performed using the Kyung-Hee University Mark 2.5 EIT machine (KHU Mk 2.5) EIT machine, which is described in more detail by Oh et al. (2011) and Wi et al. (2014). This was used because it was the EIT hardware available to the project, and is similar in configuration to other EIT devices used in research. EIT devices are typically expensive instruments, and the construction of new electrical equipment was outside the scope of the project. An image of the unit used in this project is given in Fig. 4-1.

The KHU Mk 2.5 operates on the current injection principle, where a desired current is selected and the voltage of the source is increased until the desired current is reached. This is a result of its origin as a medical research system; driving a current more than 100mA can be dangerous to a patient. Data on the maximum voltage and current which the KHU Mk 2.5 can operate at have not been published, but the fact that the machine was designed with medical imaging in mind suggests a low capacity for both.

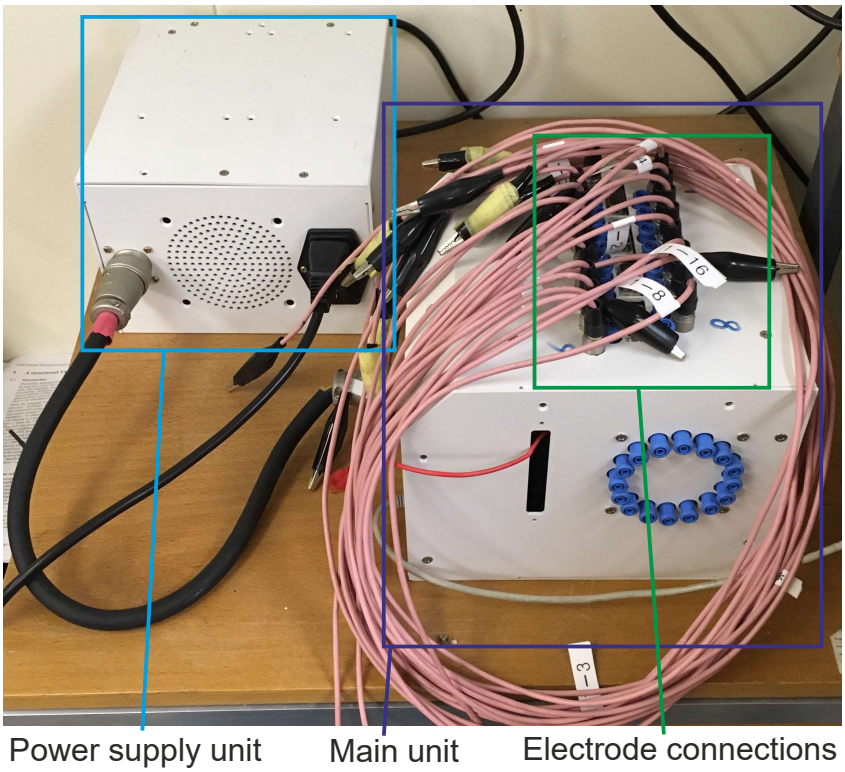

Figure 4-1: The KHU Mk 2.5 used in the project.

The KHU Mk 2.5 is described by Oh et al. as a parallel EIT machine, meaning that it can inject and measure on multiple channels simultaneously. The machine has sixteen channels. It attaches to electrodes with sixteen cables and one grounding cable ending in banana plugs - these were the connected to crocodile clips for this project. It is capable of variable current injection patterns controlled by scripts, and operates on an adjacent measurement protocol.

The KHU Mk 2.5 is able to operate at frequencies between 10Hz and 500kHz. It maintains an Signal to Noise Ratio (SNR) above 75dB and Common Mode noise Rejection Ratio (CMRR) above 80dB across this range (Oh et al., 2011). This does not account for averaging of measurements, which can further improve performance - due to the static nature of concrete testing this is trivially easy to achieve. It is fully capable of measuring phase difference for spectral imaging. The KHU Mk 2.5 is a high-performance system from the perspective of noise performance.

Data capture using the KHU Mark 2.5

Data capture using the KHU Mk 2.5 was done in all cases in a manner conventional for EIT. The four point, stimulation pair/measurement pair configuration (as mentioned in Section 2.3) was used in all cases. The KHU Mk 2.5 records "self-measurements", in which the stimulation and measurement pair share an electrode. These measurements were always discarded as this was found to produce better results.

Each imaging experiment used a different set of electrodes. The work done on dental plaster and concrete (Chapter 5) illustrated the need for care in the choice and positioning of electrodes, in order to avoid producing significant conduction paths around the outside of the body and to maintain good position agreement with the computer model. The electrode configurations for each imaging experiment are described in their relevant chapters. Several measurement arrangements were tested in the conductive mortar imaging work in Chapter 8. These are also described in Section 4.6.3. Figs. 4-2 and 4-2 show photographs of the two types of electrodes used as part of this work, which were not included in the journal paper due to limitations on number of figures. One set of the gel electrodes manufactured for the project is shown in Fig. 4-2. The silver paint electrodes which provided the final images are shown close-up in Fig. 4-3.

4.2.2 Agilent E4990A Impedance Analyser

The Agilent E4990A impedance analyser was used to provide complex impedance measurements, primarily for the work on mortar resistivity (Chapter 6) but also for some preliminary and test work. This instrument features four BNC connections on the front panel for use with standard shielded oscilloscope probes. The model used by the project had a frequency range of 20Hz to 20MHz. An image of the Impedance Analyser (IA) used in the project is given in Fig. 4-4.

Data capture using the Impedance Analyser

Measurements to determine material such as those performed for the investigation into mortar resistivity were done using the IA. All of these measurements used the four-terminal pair probe configuration from Agilent Technologies (n.d.) section 3.1.4. since it provided a relatively simple means of setting the connection up

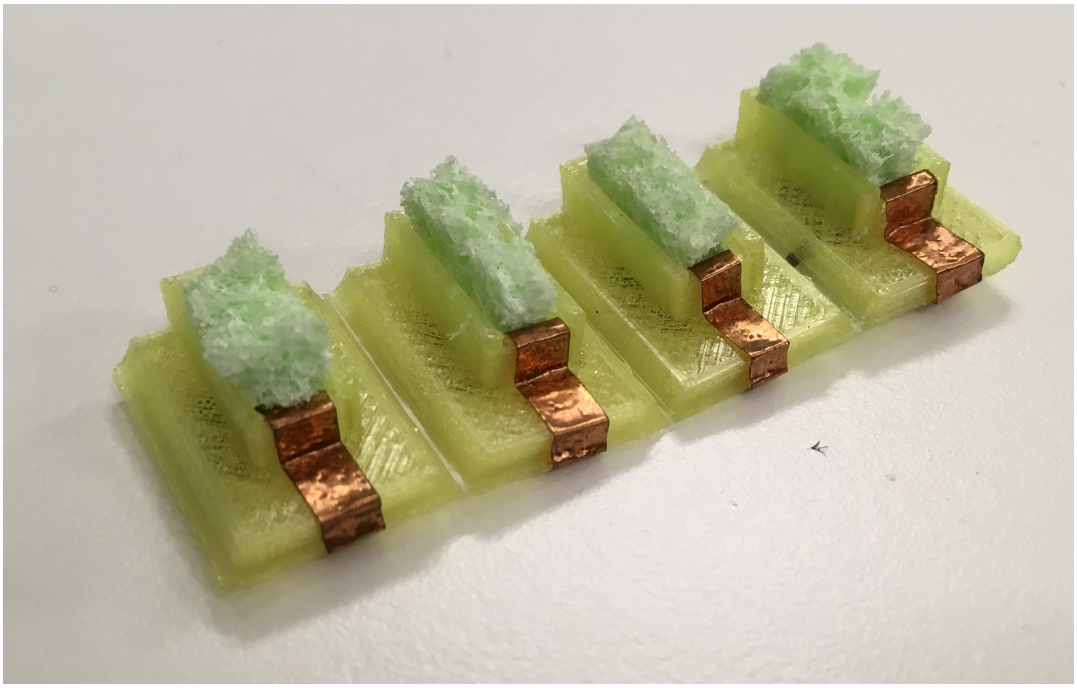

Figure 4-2: A set of 3D printed sponge-gel electrodes.

that would be not limit the frequency range of the testing. This method involved two points of contact with the part under test. The IA has a high and low supply terminal, and a high and low measurement terminal. In this connection method, both of the high terminals are connected, as are the low terminals. This is in contrast to the connection method used by the KHU Mk 2.5, in which each of the four terminals is connected to the part under test at a different point.

Probes capable of reliable measurement above 10MHz were not available, but such high frequencies were not necessarily relevant to the project since EIT typically only uses kHz range measurements. The probes in use had standard hook ends, which were connected directly to the electrodes on the material under test. In the resistivity investigation these electrodes consisted of stainless steel plates connected to short lengths of multi-core wire. The connection was made by soldering the wire to copper tape which was stuck to the steel, with the connection being verified by the continuity test of a multimeter. At other times when the IA was used it was connected to off-the-shelf Ag/AgCl gel electrodes.

Figure 4-3: Close up of the final electrode configuration.

4.3 Materials and methods used in initial work imaging plaster and conventional concrete

Methods for the first two sets of experiments are presented in this Section. Results of these experiments are presented in Chapter 5. The work on dental plaster was intended to broadly investigate the general feasibility of the rest of the project, and some decisions were made to prioritise quick completion. The attempts to image concrete were then meant to see if good results could be obtained under conditions more representative of a real Non-Destructive Testing (NDT) scenario. These were distinct experiments, but the results are presented together since in combination they fulfilled the first objective of the project.

However because of the differences between the materials and experimental arrangements, the materials and methods are separated in this Section. The first experiment, involving dental plaster, is covered by Section 4.3.1 and the second, involving concrete, is covered by Section 4.3.2. The bulk of the experimental work on the concrete cylinders was done on electrode attachment and image reconstruction. Much of the experimental work in this project involved some iteration and trial and error, and this experiment was a particularly extreme example of this. This section presents the final methods used before the project moved on.

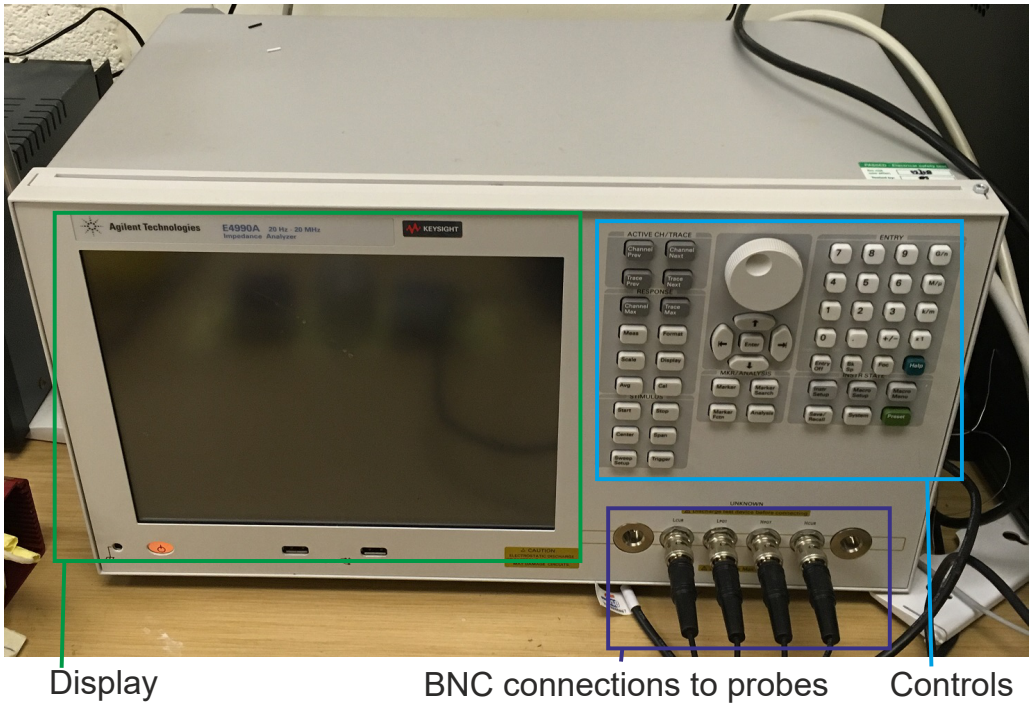

Figure 4-4: The IA used in the project.

4.3.1 EIT imaging of dental plaster cylinders

The results of the work on imaging of dental plaster cylinders are presented in Section 5.1.1.

Materials

A dental plaster mix was substituted for concrete in the initial imaging work. This substitution was made because working with dental plaster was more convenient than concrete in a number of ways - it hardens very quickly; expands on hardening (making the process of casting in electrodes trivially simple); doesn't need to be specified; and is easy to mix to the point of homogeneity. The electrical properties of the plaster were not measured as the purpose of the work was simply to start by performing EIT on a material closer to concrete than a saline phantom.

The dental plaster used was "Dentstone KD" made by Saint-Gobain (Saint-Gobain Formula, n.d.), used due to availability. It has a nominal water to plaster ratio of 30% by mass, which was adhered to for this work. Dental plaster was mixed by hand and according to the manufacturer's instructions provided by

Saint-Gobain Formula (n.d.).

Preparation of cylinders

Electrodes were cast directly into the plaster in order to reduce contact impedance and control the electrode position conveniently. Air inclusions were used exclusively, and constant cross-sections were maintained in each sample so that a 2D image reconstruction could be performed. The electrodes were stainless steel shims, located using laser cut wooden jigs held in place above the cylindrical moulds while the plaster was poured. The electrodes interfaced directly to the plaster, which held them firmly in place without the need for an adhesive. No relative movement was observed after hardening.

Five cylinders were produced. Four of these contain resistive inclusions (1 to 4) while the homogeneous cylinder (H) was produced to use as a background for Time Difference Electrical Impedance Tomography (TDEIT). The cylinders are shown from above in Fig. 4-5.

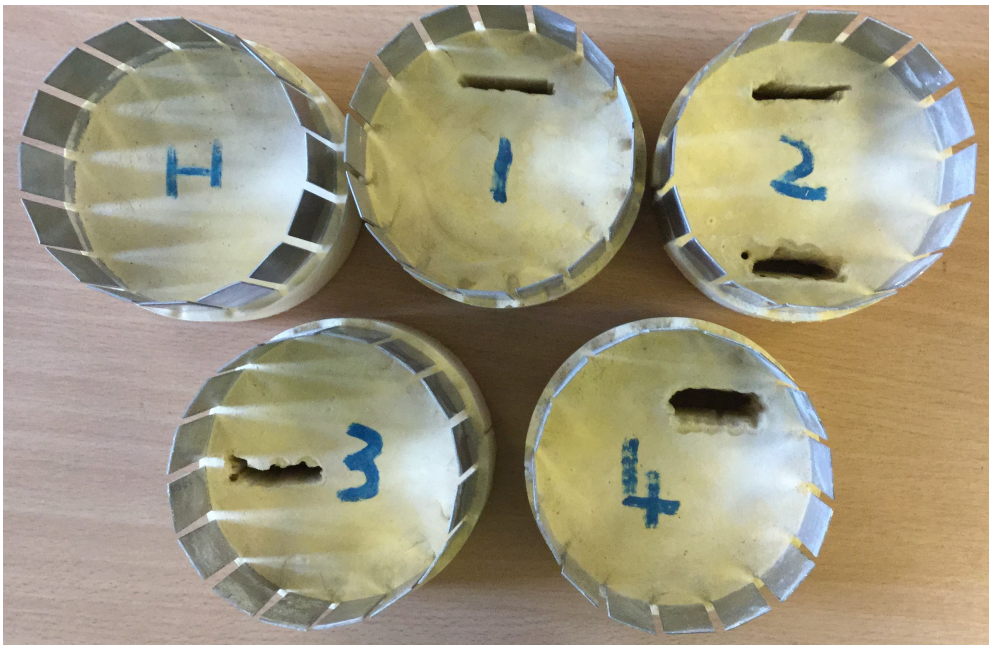

Figure 4-5: The five plaster cylinders, shown from above.

Modelling accuracy of the cylinders was not ideal due to some out of plane curvature in the steel shims caused by the manufacturing process. The wooden jigs had to be sized to accommodate this, and the result was that electrode

position was not as tightly constrained as had been planned. Electrodes were therefore less evenly placed than in the initial design.

The process of positioning the electrodes before pouring the plaster mix also resulted in reduced amounts of plaster around the outside of the samples because of its viscosity. In one case this led to the plaster coming off as the sample was removed from the mould, exposing two of the electrodes from the outside of the cylinder.

Finally it was found that a mould release agent intended for concrete will not work with plaster, since concrete contracts while it hardens whereas plaster expands. Therefore the air cavities were produced using a power drill and a saw, and the cavities were larger and less even than planned. This can be seen in Fig. 4-5.

No information on a curing regime was provided by the manufacturer of the plaster; the stated total setting time is 23 minutes. The cylinders were left in a room at approximately 19°C for three days before measurements were taken; this room was not humidity controlled. After three days it was assumed that the liquid water content of the plaster would be small, but given that this was not measured, it is possible that it had some effect on the results of this initial experiment. The electrical properties of the plaster were also not measured at this point, on the assumption that air would be several orders of magnitude more resistive than the plaster, and since accurate reconstruction of true conductivity values (as opposed to relative differences across the cross-section) was not a focus for the project.

Performing EIT measurements

Measurements were recorded three days after casting of the cylinders. All measurements were recorded using the KHU Mark 2.5 equipment described in Section 4.2.1. Leads were clipped directly to the steel electrodes, as shown in Fig. 4-6.

All of the measurements used adjacent stimulation/adjacent measurement. Measurements were recorded at 10, 50 and 100 kHz. Five sets were taken at each frequency for averaging. Other frequencies were not used due to the KHU Mk 2.5 software consistently indicating a contact impedance test fail.

Figure 4-6: One of the plaster cylinders attached to the EIT machine for measurements.

Modelling and image reconstruction

Electrical Impedance and Diffuse Optical image Reconstruction Software (EIDORS) was used for all computation in this experiment. Inversion was done using the EIDORS default method. Initially TDEIT was attempted; following the low quality of these results Frequency Difference Electrical Impedance Tomography (FDEIT) was also applied.

All combinations of frequency difference were attempted, along with varying values of the hyperparameter α. Data was scaled such that each pair of frequency datasets had the same mean value, to account for the KHU Mk 2.5 measuring different magnitudes at different frequencies. This was done after reading the data into the program and did not affect the saved data. A value of $\alpha = 0.005$ was used as a starting point since it had provided good outcomes in some familiarisation work done using the equipment with a saline phantom. Following this starting point, different values of α were tested. Of those values $\alpha = 0.001$ and $\alpha = 0.005$

are presented in Section 5.1.1. This informed future work, which generally (but not exclusively) used α values between 0.001 and 0.01.

Section 3.5 discusses a number of previous applications of EIT on concrete and mortars. This includes some notes on the algorithms that have been used by previous investigators, some of which are also described by Section 2.4.3. The inversion algorithm used here is an L_2 norm based method, more typically used for moisture transit imaging, rather than a Total Variation (TV) L_1 norm based method as used for crack imaging by Smyl et al. (2018) and others. This decision was made because of the relative simplicity of implementing L_2 norm based methods. While a TV method would be expected to provide better detail of the inclusion due to its promotion of sharp conductivity changes, the more basic method was expected to provide satisfactory results considering the size of the inclusions relative to the body. Therefore the extra effort of implementing TV was not necessary.

4.3.2 Initial imaging using concrete

The results of the initial work on imaging of concrete cylinders are given in Section 5.2.

Materials

Cement All cement paste was made with a Portland fly ash cement (CEM II/B-V 32.5N) conforming to BS EN 197-1.

Fine aggregate Fine aggregates were an alluvial sand and Marlborough grit aggregates conforming to BS EN 12620. Grading of fine aggregates is given in Fig. 4-7.

Coarse aggregates Coarse aggregates were 10mm crushed limestone, conforming to BS EN 12620. Grading of the coarse aggregates is given by Fig. 4-7.

Concrete mix proportions The concrete used in the work described by Section 5.2 was composed of the aforementioned components. The mix proportions are given by Table 4.1:

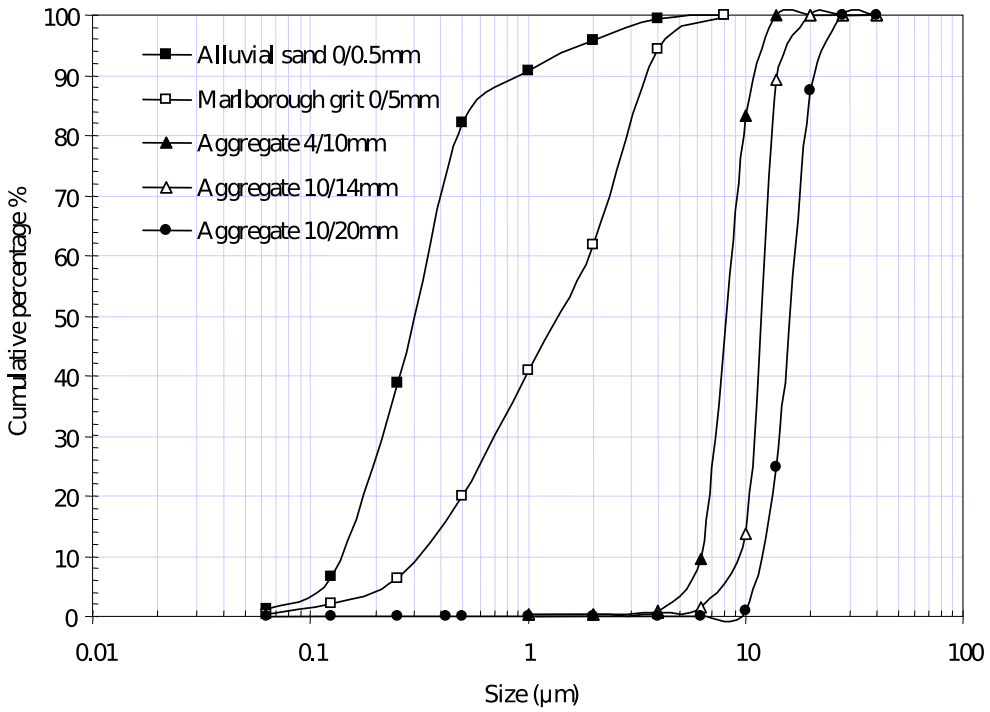

Figure 4-7: Grading of aggregates used to produce the concrete cylinders. This graph has been reproduced from Ioannou (2012).

Table 4.1: Mix proportions concrete samples used in testing.

Material	Density (kg/m^3)
Water	206
Cement	516
Coarse aggregates	877
Grit	645
Sand	180

Production of the concrete cylinders

Three concrete cylinders containing inclusions were available for this experiment. These cylinders were inherited by the project, and had been cast approximately three years prior to the experiment being performed. These mature concrete cylinders presented an opportunity to apply EIT on concrete whose electrical properties had stabilised. After moulding, the cylinders were placed in a controlled environment room (20°C, 40% RH) for 24 hours. They were then demoulded at 24 hours and stored in water at 20°C until an age of 35 days. They were then allowed to dry naturally and stored in an uncontrolled environment until being used in this experiment.

Geometry of the concrete cylinders

Each cylinder was slightly differently sized, and they also had different cross sections. One contained a relatively resistive inclusion and two contained relatively conductive inclusions. Each contained a long region of constant cross-section starting from the top of the concrete; enough that image reconstruction was attempted using the 2D approximation. Figure 4-8 gives a top-down view of the samples showing the cross section.

Figure 4-8: The three concrete samples.

Table 4.2 gives the sizes and locations of the different inclusions; everything is assumed to be circular.

Table 4.2: Geometrical data for the concrete samples used in testing.

	Plastic pipe	Single metal bar	Two metal bars
Overall diameter	150 mm	152 mm	153 mm
Inclusion dimensions	I.D. 32.5mm O.D. 36.2mm	O.D. 13mm	O.D. 5mm
Inclusion location(s)	40mm from edge	50mm from edge	45 mm and 85mm on a line roughly normal to edge

Investigation of factors affecting impedance across electrode pairs

A number of configurations of electrode that had been used in EIT on concrete have been described in the literature. Once a decision on the basic type of electrode to use had been made, some experimentation was done to determine how the electrodes could be applied to give the best results. This was generally

intended to be a more "realistic" application of EIT than the work on dental plaster, hence the use of existing cylinders. This meant that electrodes could not be moulded in to the cylinders as they had been previously. It was decided to use circular electrodes applied to the cylinder surface. These were to be arranged in a single ring parallel to the cylinder ends. The inclusions were arranged such that the cross-section of the cylinders was constant throughout, as in the work on dental plaster. However, the electrodes not being connected to the full height of the cylinder potentially renders this arrangement more vulnerable to problems if the conductivity of the concrete were to differ along the cylinder height near the electrode ring. Although the use of the smaller electrodes introduces the possibility of these 3D effects, they were considered extremely unlikely and the experiment was treated as a 2D problem, as in Suryanto et al. (2017b).

Karhunen (2013, p.39) makes reference to having used two types of electrode in experiments on concrete. Of the two types, the ones based on a conductive gel are said to be less prone to problems caused by concrete absorbing liquid than the ones based on a conductive liquid. On this basis it was decided to use gel electrodes to achieve contact with the concrete. A sixteen electrode pattern was used as in the plaster experiments. Silver-silver chloride electrodes designed for medical ECG machines were bought off-the-shelf for the sake of convenience. These electrodes provided easy connection to the KHU Mk 2.5 using the machine's crocodile clips, and were strongly self-adhesive. The contact part of the electrodes consisted of a circular sponge of approximately 20mm diameter, which held the gel.

In preliminary testing, impedance between electrodes was found to be very high. Some brief testing was done to see if this could be reduced without changing the materials. A smaller homogeneous concrete cylinder was prepared for this purpose. The cylindrical shape was used simply because of available moulds, and the smaller size was desired to reduce the base level of impedance across the electrodes. The smaller size of the cylinders made it impossible to accommodate enough electrodes to use readings from it as a background. During this testing the smaller cylinder was between one and two weeks old, and was thus less resistive than the other concrete. This was done to ensure that the IA would be able to produce meaningful results to compare in spite of its relatively low voltage.

Concrete is a porous material, and can absorb liquids. Karhunen (2013) de-

scribes encountering problems with conductive fluid being absorbed when using wet electrodes, and low impedance conduction paths being produced at the surface of the concrete body. Karhunen apparently did not encounter the same difficulty when using gel, but there was still some question as to how much of an effect the transit of the gel in the concrete might have on the impedance between two electrodes.

Test of impedance magnitude across gel electrodes over time Two electrodes were attached to either side of one of the homogeneous concrete cylinders, and the impedance across them measured using the IA. The IA was used to measure the magnitude of the impedance between the electrodes across a frequency range of 10kHz to 500kHz, and the measurements were repeated over the course of two days at intervals of several hours. Over this time concrete cylinder was kept in an air conditioned room, although temperature and moisture content were not measured. The measurements were taken manually so as not to leave the IA on for extended periods, so intervals were irregular.

Test of application of pressure to electrodes Finally, another test was performed using the IA to determine how much improvement adding pressure to the electrodes might reduce impedance across electrodes. Investigators such as Hallaji et al. (2015) applied some amount of pressure to their electrodes through some mechanism. There are several reasons that the pressure might have some effect. Gel or wet electrodes tend to consist of a conductive fluid stored in a sponge, which is then applied to the boundary. Pressure applied to these sponges would simply promote the flow of the fluid to some degree. In any case, compressing the concrete will reduce impedance by reducing the size of pores and reducing the amount of air that the current must travel across. Neither of these causes seemed likely to have a large effect on impedance but anything that might reduce impedance would be welcome so a test was performed.

Two pairs of electrodes were applied to opposite sides of one of the homogeneous concrete cylinders. One of the pairs was compressed using a G-clamp, with pieces of wood used to distribute the force and prevent the metal clamp from shorting the two electrodes.

The results of both of these experiments are shown and discussed in Sec-

tion 5.2.1.

Performing EIT measurements

Without casting the electrodes into the samples as in the plaster cylinders, controlling their position was more difficult. Following the observations about excessive electrode size form the previous experiment, some simulations were performed with EIDORS to try to establish an electrode length:body diameter ratio which would avoid concentrating the electric field around the outside of the body. In this case the result was that an electrode length of around 10mm would be sufficient to ensure good distribution of the electric field. Because this was smaller than the actual sponge diameter, the electrode positioning could be done quite simply. Belts made of Mylar were laser cut to a length specific to each sample, with circular holes cut to allow sixteen gel electrodes to be equally spaced on the body. The initial experimental setup is shown by figure 4-9.

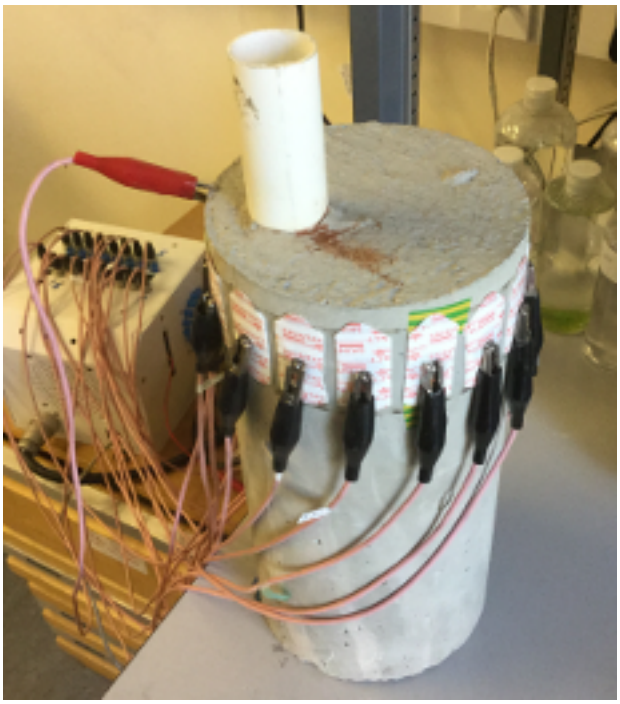

Figure 4-9: A concrete sample connected to the KHU Mk 2.5.

Other than the gel from the electrodes, the cylinders were completely dry when tested. Twenty readings were taken at each frequency for averaging. Adjacent stimulation/measurement patterns were used.

Modelling and image reconstruction

The computational part of the experiment was generally similar to the plaster experiment. EIDORS was used for modelling and Tikhonov regularisation (TK-R) was used for the inversion. TK-R was used in this case for the inversion. TV was not used for the same reasons as in the work on dental plaster described in Section 4.3.1; given the size of the inclusions the sharp conductivity discontinuities reconstructed by TV was not expected to provide an improvement proportionate to the extra work of implementing it.

Only FDEIT was attempted due to unavailability of a blank background, all frequency combinations were used, and a number of hyperparameters were tested in each case. As in the dental plaster work, data was scaled such that each pair of frequency datasets had the same mean value to account for the KHU Mk 2.5 measuring different magnitudes at different frequencies.

4.4 Materials and methods used in the investigation into conductive mortar resistivity

This section gives materials and methods for the investigation into conductive mortar resistivity (Chapter 6) which fulfilled objective two of the project. This investigation was intended to produce information useful in deciding how to produce mortar to be used for EIT, both inside and outside the context of this project. Some of the materials used carried safety risks beyond those typically used in mortar production, and much of the procedure for producing the mortars was intended to minimise those risks as far as possible. This section is largely identical to Section 6.3 since the chapter is presented as a complete and self-contained journal paper. Some additional information included here that could not be included in the journal paper is indicated by italics.

4.4.1 Materials

The aim of this research was to investigate how mortar resistivity changes with the presence of a carbonaceous material (CBM) addition whose only purpose was to reduce resistivity magnitude. Two other factors common to all mortar mixes

- relative quantities of different aggregates, and water to cement ratio - were also considered. No plasticisers were used.

A Portland fly ash cement, CEM II/B-V 32.5 N conforming to BS EN 197-1, was used for all mortars. Two natural fine aggregates conforming to BS EN 12620 of differing particle size distribution were used to assess the effect of fineness of fine aggregate. The grading of both fine aggregates is shown in Figure 1. The finer of the two aggregates was an alluvial sand (s), whilst the coarser fine aggregate was a Marlborough grit (g). The two fine aggregates were combined in g/s ratios of 0.6 to 1.2. This represents a change in fineness (expressed as percentage passing the 500 μm sieve) of 36.5% to 50% by mass. Grading of the aggregates is given in Figure 4-10:

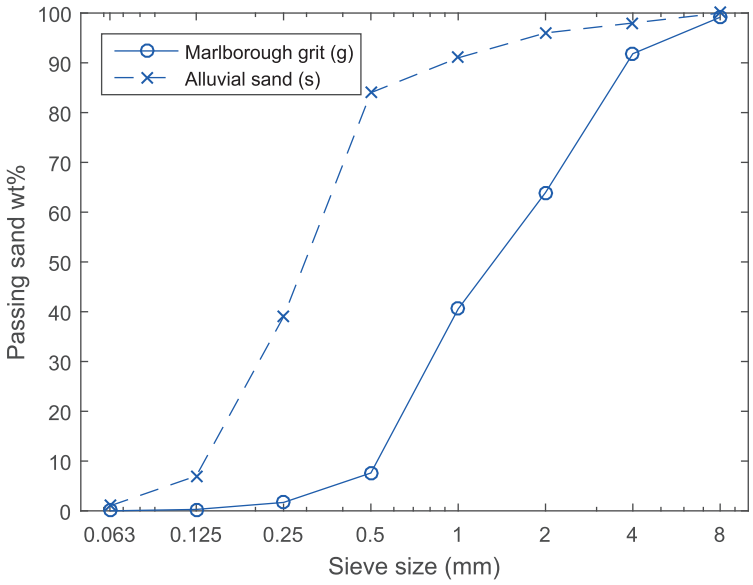

Figure 4-10: Particle size distribution of the fine aggregates.

The CBMs selected were: milled carbon fibre powder (CFP) and graphite powder (GP). The CFP was typically greater than 5 μm in length and less than 3 μm in diameter. The particle density was approximately 1800 kg/m^3. The particle size of the GP was such that 85% passed a 44 μm sieve. The particle density was approximately 1900 kg/m^3. *Conductivity of the CBMs was not provided by the manufacturer and was not measured due to the safety concerns described below.*

Working with these carbonaceous powders presents health risks beyond those

usually encountered when preparing cementitious materials. The Material Safety Data Sheets (MSDS) were obtained for both CFP and GP from the manufacturer. These indicated essentially the same safety considerations for both materials: protection of skin, eyes, and the use of a dust mask to prevent skin, eye and respiratory irritation. In practice, both materials were found to become airborne very easily. The powders were supplied in large tubs; opening the lid to a tub was enough to produce a small dust cloud. Therefore the personal protective equipment was used at all times when handling the powders, and other measures were taken to reduce the amount of powder that became airborne, as described in Section 4.4.2.

Details of the 24 mixes used are given by Table 4.3. *One cube was manufactured per mix. Table 4.4 is included to aid reproducibility, and gives the mixes with the quantity of each dry material as a percentage of the overall mass of dry materials. Note that WPCM is a percentage of the overall material mass including water, so differs from the weight percentage of dry material for each CBM.*

				Mass ratios relative to cement			
Mix ID	CBM	WPCM	g/s	w/c	s/c	g/c	CBM/c
1	None	0	0.8	0.70	1.67	1.33	0.00
2	None	0	0.8	0.80	1.78	1.42	0.00
3	None	0	0.8	0.90	1.89	1.51	0.00
4	None	0	0.6	0.80	2.00	1.20	0.00
5	None	0	1	0.80	1.60	1.60	0.00
6	None	0	1.2	0.80	1.45	1.75	0.00
7	CFP	1	0.8	0.90	1.73	1.42	0.05
8	CFP	3	0.8	0.90	1.63	1.42	0.14
9	CFP	5	0.8	0.98	1.54	1.42	0.24
10	CFP	9	0.8	1.06	1.30	1.42	0.48
11	CFP	4	0.8	1.04	1.44	1.33	0.22
12	CFP	5	0.8	1.17	1.63	1.51	0.26
13	CFP	4	0.6	1.14	1.76	1.20	0.24
14	CFP	5	1	1.11	1.36	1.60	0.24
15	CFP	5	1.2	1.08	1.21	1.75	0.24
16	GP	1	0.8	0.90	1.73	1.42	0.05
17	GP	3	0.8	0.90	1.63	1.42	0.14
18	GP	5	0.8	0.90	1.54	1.42	0.24
19	GP	9	0.8	1.14	1.30	1.42	0.48
20	GP	5	0.8	0.95	1.44	1.33	0.22
21	GP	5	0.8	1.00	1.63	1.51	0.26
22	GP	4	0.6	1.16	1.76	1.20	0.24
23	GP	5	1	0.90	1.36	1.60	0.24
24	GP	5	1.2	1.08	1.21	1.75	0.24

Table 4.3: Table of mixes tested.

				Weight percentage of dry material (%)			
Mix ID	CBM	WPCM	w/c	% Sand	% Gravel	% Cement	% CBM
1	None	0	0.70	41.66	33.33	25.01	0.00
2	None	0	0.80	42.32	33.87	23.81	0.00
3	None	0	0.90	42.93	34.35	22.72	0.00
4	None	0	0.80	47.62	28.57	23.81	0.00
5	None	0	0.80	38.10	38.10	23.81	0.00
6	None	0	0.80	34.63	41.56	23.81	0.00
7	CFP	1	0.90	41.18	33.87	23.81	1.14
8	CFP	3	0.90	38.90	33.87	23.81	3.43
9	CFP	5	0.98	36.61	33.87	23.81	5.71
10	CFP	9	1.06	30.90	33.87	23.81	11.43
11	CFP	4	1.04	36.03	33.33	25.01	5.62
12	CFP	5	1.17	37.13	34.35	22.72	5.80
13	CFP	4	1.14	41.90	28.57	23.81	5.71
14	CFP	5	1.11	32.38	38.10	23.81	5.71
15	CFP	5	1.08	28.91	41.56	23.81	5.71
16	GP	1	0.90	41.18	33.87	23.81	1.14
17	GP	3	0.90	38.90	33.87	23.81	3.43
18	GP	5	0.90	36.61	33.87	23.81	5.71
19	GP	9	1.14	30.90	33.87	23.81	11.43
20	GP	5	0.95	36.03	33.33	25.01	5.62
21	GP	5	1.00	37.13	34.35	22.72	5.80
22	GP	4	1.16	41.90	28.57	23.81	5.71
23	GP	5	0.90	32.38	38.10	23.81	5.71
24	GP	5	1.08	28.91	41.56	23.81	5.71

Table 4.4: Table of mixes tested in terms of weight percentage of dry material.

4.4.2 Preparation of mortar specimens

A series of 24 mortar mixes were produced. Ratios of the different fine aggregates were intended to correspond to the range of fine aggregate finenesses used in concrete. *Water to cement ratios were chosen largely for practical reasons with a high water content used to maintain workability, which was found to be decreased by the presence of CBM, to facilitate mixing.* The sand to cement ratio ranged from 3 to 3.4 in all mixes and the w/c ratio ranged from 0.7 to 0.9 for the non-conductive mortars and from 0.9 to 1.2 for mortars containing CBM. Higher w/c ratios were used for the CBM mortars because it was found that this was

necessary to maintain consistence and properly mix the materials. Whilst it may have been possible to use lower w/c ratios by use of water-reducing admixtures, as will be likely when conductive concrete is produced for practical applications, this would have increased the complexity of the mixes and may have obfuscated the effect of w/c on conductivity in this parametric study.
CBM was added to the mortars in proportions of 1 to 9% by mass of mortar; which represents approximately 5 to 32% by mass of cement + CBM.
Mixing was carried out by hand. Prismatic specimens of 40 x 40 x 48mm were cast for each mix. Slight variations in length were allowed and accounted for in electrical property calculations. Fine aggregates and cement were mixed together before the addition of water. The manner in which the CBM was added differed when using CFP or GP. CFP preliminary mixes with relatively low WPCM showed that initially dispersing the CFP in water was a viable way of reducing some of the safety risks associated with the powder. When making the higher WPCM mixes this practise was found to lead to flocculation of the powder and extra physical mixing had to be done to mitigate this effect. In contrast the GP was found to float in the water, so was added directly with the fine aggregates and cement, with the safety risks being addressed with personal protective equipment.
The specimens were placed in a controlled environment room (20°C, 40% RH) for 24 hours. All specimens were demoulded at 24 hours and stored in water at 20°C until an age of 35 days.

4.4.3 Electrical measurements

Measurements were taken using an Agilent E4990A impedance analyser. Each mortar cube was removed from the water and surface dried using a cloth before measurements were taken. Surface temperature was not controlled when out of the water. These temperatures were not used in the analysis but are included in the online data for the study.
Measurements were taken at 7, 14, 21, 28, and 35 days after casting the mortar. Stainless steel electrodes were clamped to the cubes and connected to the impedance analyser using the four-terminal pair probe configuration described by Agilent Technologies (n.d.) section 3.1.4, as shown in Figure 4-11.

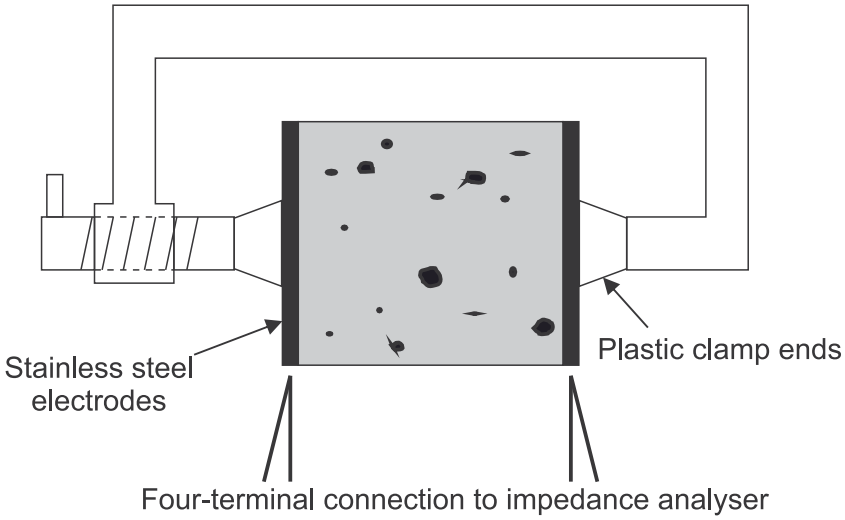

Figure 4-11: Mortar cubes as clamped and connected to measurement equipment.

The initial set of measurements was taken at 200 frequencies within the 20Hz-20MHz range, using a linear frequency sweep. For subsequent measurements the scheme was changed to use 1000 frequencies in a logarithmic sweep to better represent the response at lower frequencies. A complete measurement set for each cube took no more than two minutes. Measurements above 10MHz were found to be significantly affected by the measurement probes in use. These were discarded.
Some particular combinations of mixes and times have not been presented in this paper where they are not pertinent to comparisons being made, but all of the data produced for the research is available online - see the data access statement for details.

4.5 Materials and methods used to perform further analysis on the conductive mortars

Further analysis was performed on the conductive cubes (following the publication of the work) to better understand the effects of varying mortar mix parameters on resistivity. Since fully hydrated concrete was of primary interest for the EIT application all of this work was done using the measurements taken at 35 days hydration. No new experimental work was performed; all the materials and ex-

perimental methods applying to the initial work investigating conductive mortars apply here. All of the cube numbering has also been carried over. This section describes the methods used for the further analysis.

4.5.1 Equivalent circuit analysis

Equivalent circuit analysis, as described in Section 3.2.2, was used to compare the relative effects of each mix parameter.

The analysis was performed using EISAnalyser software described in Pomerantsev (2005, pp. 89-102). Fitting was done using the Powell algorithm implemented in the software. This is an iterative algorithm, and varying numbers of iterations were used to obtain a good fit to the measured data. The number of iterations used is given along with the calculated component values in Table 7.1. A number of equivalent circuit models applicable to conductive cementitious materials have been proposed, including by Torrents et al. (2001), Woo et al. (2003), Cruz et al. (2013), and Suryanto et al. (2016). The model used here was that developed by L. Zhang et al. (2017), chosen because it provided the best fit for the data. The circuit is given by Fig. 4-12.

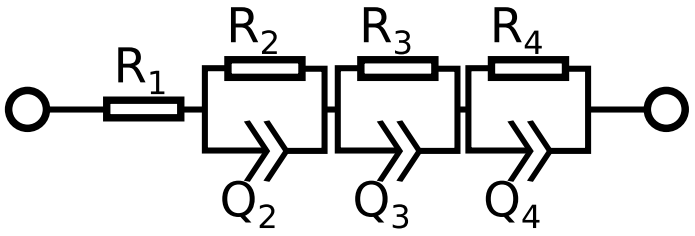

Figure 4-12: Diagram of the equivalent circuit, after L. Zhang et al. (2017).

L. Zhang et al. give an explanation for the physical meaning of the components, with R_1 representing the resistance of the fluid solution in the pores (this assumes a saturated mortar, which the cubes were when measured), R_2Q_2 representing the effects of the cement matrix excluding the additions, R_3Q_3 representing the effects of the electrodes, and R_4Q_4 representing the effects of the cement matrix in series with the additions.

Unlike the initial investigation into these conductive mortars, this analysis used impedance measurements ($|Z|$) rather than resistivity ($|Z|\cdot$m). This is because using impedance was necessary for the equivalent circuit modelling process

to produce meaningful values for the equivalent circuit. Resistivity for each mix was calculated and used to scale the impedance to that of a 40 x 40 x 48mm specimen (each specimen had the same cross-sectional area, and 48mm was the average length) and this was used to calculate the equivalent circuit parameters.

Results of this analysis are given in Section 7.1.1 and discussed in Section 7.2.1.

4.5.2 Fitting conductivity values to a theoretical model

The effective medium theory approach for predicting electrical conductivity as given by Suryanto et al. (2016) was applied to the conductive mortars, to see if they would behave as expected. This is described in Section 3.2.3 and Eqs. 3.1 and 3.5.

Some physical information on the conductive additions is required by this method; length L and diameter d of the particles, as well as the conductivity σ_m. This information was not measured for safety reasons discussed above, but some information relating to Carbon Fibre Powder (CFP) was available. The MSDS obtained from Easy Composites (n.d.*c*) states $L > 5$ μm and $d < 3$ μm, with an aspect ratio A greater than 3. For σ_a Wypych (2016, pp. 252-255) suggests a conductivity value of $6{\cdot}10^4$S/m for milled carbon fibres, but this can apparently vary depending on manufacturing processes.

In Suryanto et al., σ_m was taken at the point between the interface and bulk arcs for the control mix in which $\phi = 0$. Next they took conductivity values from another interface (at a frequency "f_c") between arcs that appeared at higher frequencies in their data as σ_e and compared these to simulated values, testing the versions of the equation for randomly and less-randomly oriented particles.

σ_m using this method was taken from the control mix 3 at $f_c = 25$kHz, giving a value of 0.017 S/m. σ_e was taken from the $\phi = 1.1\%$ CFP mix number 7 at $f_c =$ 320kHz, giving 0.045 S/m. Initially it was attempted to use Eq. 3.1 with known σ_e, σ_m, ϕ, L and d (assuming $A = 4$) to solve for σ_a, since it was not known how applicable the value from Wypych (2016) was. This produced results that were not physically reasonable. However, examining the equation with Wolfram Mathematica demonstrated two things: firstly that at low volume fractions the result σ_e has a relatively low sensitivity to changes to σ_a, and secondly that the sub-equation for R could be rewritten in terms of L/d, so if σ_a were known it could

be solved for the particle aspect ratio A.

Therefore the approach was changed. R was rewritten in terms of aspect ratio A. Because of the low sensitivity of the equation to σ_a, it was reasonable to trust the $6{\cdot}10^4$S/m value and it was used in Eq. 3.1. The "brentq" function in the "scipy" Python library was then used to solve for A. This resulted in an aspect ratio of 38.4. This was higher than expected, but appeared to be physically reasonable - Wypych (2016) gives A for milled CFP at 6-30. It was also only slightly lower than the A of the additions used by Suryanto et al. (2016). Therefore based on their findings, the version of the model for use with non-randomly oriented additions (Eq. 3.5) was also used and compared. Finding values experimental values of σ_e in the same way Suryanto et al. was impossible to do precisely in some cases since no interface between higher frequency arcs could be discerned. σ_e values were estimated by inspecting the Nyquist plots for changes in gradient. In some cases a value could not be discerned with any confidence and these mixes were not used in the analysis.

Ultimately this process was only applied to CFP mixes, in the absence of a trustworthy value for σ_a and because distinctive arc transitions were indistinguishable in almost all of the associated Nyquist plots.

Finally the same method was applied to Graphite Powder (GP), assuming the same σ_a as for CFP. The eventual procedure was:

1. Determine σ_m and σ_e by inspection of experimental data for the $\phi = 0\%$ and $\phi = 1\%$ mixes respectively.

2. This data along with the σ_a from the literature was used to solve both Eqs. 3.1 and 3.5 to find values of A for CFP, in cases assuming random and non-random orientation of additions.

3. These values of A were used to predict σ_e for a variety of ϕ.

4. Experimental values of σ_e were obtained by inspecting Nyquist plots for the higher ϕ mixes.

5. Experimental and predicted values were graphed and compared.

Results of this are given in Section 7.1.3 and discussed in Section 7.2.2.

4.5.3 Percolation

Some work was also done to attempt to determine whether or not the conductive additions in the mortars had achieved percolation as described in Section 3.2.3 and at what quantity of additions this would be expected to happen. It is important to note that when the mixes were designed, quantities were assigned by weight because of course this is much more convenient to work with during manufacturing. When considering percolation, volume percentage (also called volume fraction) rather than weight percentage of the conductive additions must be used. Densities of the components that were used to calculate these are as follows: sand at $2650^{kg}/_{m^3}$, grit at $2700^{kg}/_{m^3}$, cement at $3150^{kg}/_{m^3}$, water at $1000^{kg}/_{m^3}$, CFP at $1800^{kg}/_{m^3}$ and GP at $1900^{kg}/_{m^3}$. Volume percentages of the conductive additions for each of the mixes containing conductive additions used in the percolation analysis are given by Table 4.5.

	CFP density $^{kg}/_{m^3}$		GP density $^{kg}/_{m^3}$
Mix 7	1.1	Mix 16	1.0
Mix 8	3.3	Mix 17	3.1
Mix 9	5.3	Mix 18	5.2
Mix 10	10.0	Mix 19	9.3

Table 4.5: Table of volume percentages of conductive additions in the mortar mixes containing them.

Firstly the conductivity of mixes was graphed against the quantity of conductive additions for inspection. Next, this data and $\sigma_a = 6{\cdot}10^4$S/m was used to fit Eq. 3.7, finding $\phi_{c,e}$ and n_e. Fitting was done with the "leastsq" function in the "scipy" Python library, but the results were not physically feasible and are not presented. The graphs are given in Section 7.1.4 and discussed, along with the failure to fit the data to the threshold equation, in Section 7.2.3.

4.6 Materials and methods used in the imaging of conductive mortar cylinders

This section gives materials and methods for the imaging of conductive mortar cylinders (Chapter 8) which fulfilled objective three of the project. This work

was focused on imaging from the perspective of industrial NDT, particularly in the image reconstruction methods. Safety was again a concern as it was when the mortar cubes were produced, and the procedure that he been found to be safe previously was used again. As with the previous section, this is reproduced from Section 8.2 since the chapter is presented as a complete and self-contained journal paper. As in Section 4.4, any additional information included here that could not be included in the journal paper is italicised.

4.6.1 EIT equipment

Impedance readings were taken using a KHU mark 2.5 EIT machine described by Wi et al. (2014) and using the standard control software provided with the machine. The KHU mark 2.5 is a PC-based system, consisting of an analogue measurement module, a digital control and network module, and the power supply.

The KHU series of EIT devices has been developed from the perspective of medical imaging rather than structural health monitoring or industrial process imaging. This requires that the current source be limited to low amperage for reasons of patient safety.

4.6.2 Conductive mortar cylinders

The mortar used a Portland fly ash cement, CEMII/B-V 32.5N. Fine aggregates used were an alluvial sand (s) and Marlborough grit (g), both conforming to BS EN 12620. The g/s ratio used was 0.8. The mortar's electrical resistivity was reduced by the addition of Graphite Powder (GP) such that the Weight Percentage of Carbonaceous Material (WPCM) was 5%. According to the manufacturer, the GP particles were sized such that 85% passed a 0.044mm sieve. Particle density was roughly 1900 kg/m^3. GP was used to represent fine sand for the purposes of calculating g/s. The composition of the conductive mix was based on earlier experiments into mortar conductivity and had a w/c ratio of 0.95, GP/c ratio of 0.22 and an overall aggregate (s+g+GP) to cement ratio of 2.77. It was not intended to closely represent a mix that might be used in a structural application.

The choice of mixing method was guided by the need to minimise the safety risks that carbon powders pose to humans and electrical equipment. *The mix-*

ing process was basically the same as the one for GP from Section 4.4.2. GP was mixed by hand with fine aggregates and cement powder, and water added afterwards. Moulds were made by cutting plastic pipes in half lengthways and reassembling them with tape. The water content of the mortar was unusually high since it was found that this was necessary to ensure that the components mixed properly with the water in the presence of the GP.

Three cylinders were investigated. These were of approximately 120mm height and 65mm nominal diameter. Each had a different defect created during casting using wooden inclusions, with the wood removed to produce air-filled voids. The inclusions were aligned with the long cylinder axis as far as possible, so that cross section was constant for 80% of the cylinder height. The diameter of all cylinders was 65mm. Cross sections of each cylinder are given by Fig. 4-13.

After moulding, the cylinders were stored at 20°C and 40% RH for 24 hours. They were then demoulded after 24 hours and kept in 20°C water for around six months before being allowed to air dry for the first set of tests. A more comprehensive drying protocol was not used since natural air drying better represents the actual conditions under which EIT might be used for structural health monitoring.

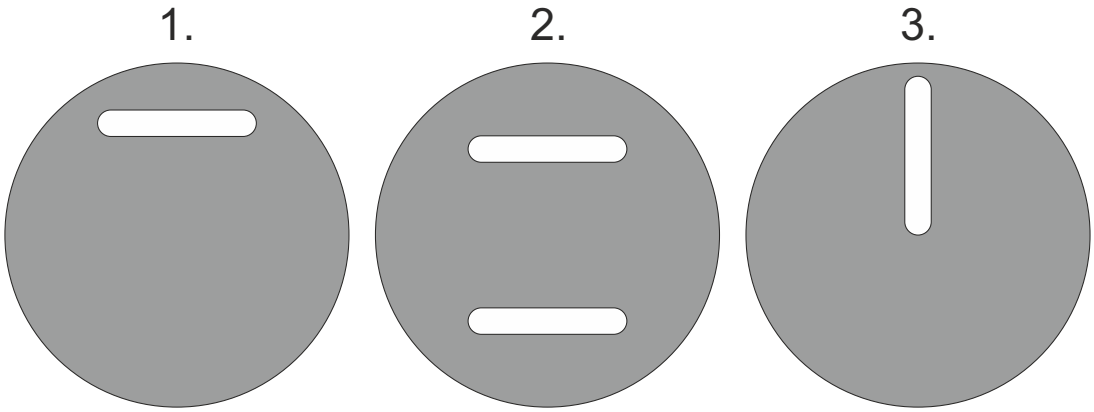

Figure 4-13: Diagrams of all mortar cylinders.

Testing of this conductive mortar versus a conventional mortar of the same mix parameters showed a reduction of real resistivity magnitude of over 50% at the frequencies used in this study. The real resistivity of the mortar at 1 kHz (at which the most useful imaging results were obtained) was 37 Ω·m.

4.6.3 Interfacing the cylinders and EIT equipment

Preliminary work found that the results of imaging attempts were very sensitive to the approach to connecting the EIT hardware and the mortar cylinders. Three measurement configurations were tested.

The first approach (method A) was to use electrodes consisting of sponges soaked in a conductive electrode gel. The small size of the mortar cylinders prevented the use of readily available commercial gel electrodes. To produce electrodes of the necessary size sponges were soaked with a medical electrode gel and located using 3D printed jigs. Copper tape was used as an intermediary between the sponge and the clips from the connection cables of the EIT system. The sponges were left attached to the mortar surface for four hours between the initial application and the measurements being taken to allow the gel to penetrate the mortar to some degree and reduce overall impedance across electrodes. *A photograph of one of the sets of sponge electrodes is given by Fig. 4-2.*

In method B electrodes consisted of colloidal silver paint applied to the surface of the mortar, similarly to Hallaji et al. (2015). The connection to the EIT system was made by securing one end of a short length of multi-core wire to the painted electrode. The other end of the wire could then be attached to the connection cable of the EIT system. This produced a lower impedance connection between the electrode and the EIT system than the gel electrodes. Particularly useful was the ability to use a basic multimeter to verify continuity between parts of the electrode to ensure the integrity of each electrode. The same process was used to verify that each electrode was properly connected to the EIT system before measurements were taken.

Finally in method C, the cylinders were immersed in water to reduce the overall impedance of the mortar. It was found that the painted silver electrodes would survive the immersion reasonably well, and any erosion could be easily repaired by applying more paint. Cylinders were allowed to sit in water for seven days until saturation, and surface water was removed with a cloth before measurements were taken. Otherwise the process was identical to method B. *A photograph some of the painted on electrodes electrodes is given by Fig. 4-3.*

Results using the method A were poor and did not produce usable inversions. Problems encountered during cylinder preparation included verification that the

sponge was properly located and seated, and ensuring continuity from the electrode to the EIT system. Method B was easier to control and required less experimental work than the first. In spite of this it did not produce usable data when used with the available EIT equipment. Method C was a minor variation on method B in terms of preparatory work, but produced usable data.

Karhunen et al. (2010a) had success using gel to make contact between concrete and electrodes. It is possible that better results could have been obtained here if the electrodes used were refined further. This was not undertaken in this instance since the third method was shown to work quite successfully. The results presented here should not discourage the use of gel electrodes in other work.

4.6.4 Image reconstruction in EIT

Here follows a basic description of the mathematical process of image reconstruction in electrical property imaging - for a more detailed treatment see Holder (2004). The fundamental goal of EIT is to infer a conductivity distribution σ within a medium Ω from voltage measurements $\mathbf{V}$ taken on the medium boundary $\partial\Omega$. This is in practice difficult to do well but the basic principles of image reconstruction can be understood intuitively.

EIT image reconstruction uses a sensitivity matrix (taking the form of $\partial V/\partial\sigma$ it is often referred to as "the Jacobian") relating the effect of each voltage measurement in $\mathbf{V}$ to each element in σ.

Reconstructing σ from $\mathbf{V}$ is an example of an ill-posed inverse problem. The difficulty comes from the fact that significant variations in σ can produce variations in $\mathbf{V}$ which are significant compared to the resolution at which measurements can be obtained. This means that for a given $\mathbf{V}$, there may be no unique σ. The image reconstruction algorithm must determine the most plausible σ possible with the collected data.

Many algorithms have been developed to find solutions to inverse problems. Tikhonov regularisation is particularly common in EPI, and is the method used for all image reconstructions in this work. It balances the influence of the noisy measured data against an assumed solution or type of solution ("prior"). In the case of Tikhonov regularisation this assumption is of a uniform distribution of resistivity, expressed by an identity matrix. The regularisation parameter (or

hyperparameter) α is used to control the relative influence of the data and the prior. *As elsewhere in the project, TK-R is used over TV because the inclusions were large enough that the benefits of TV were outweighed by the effort of implementing it.* This results in the Tikhonov functional which is to be minimised, shown in Eq. 4.1 from Kirsch (2011, p.37), in EIT terms.

$$||J\sigma - \mathbf{V}||^2 + \alpha||\sigma||^2 \tag{4.1}$$

Once the sensitivity matrix J is obtained, Tikhonov regularisation calculates the conductivity of the physical body from the measured data as shown in Eq. 4.2:

$$\sigma = (J^*J + \alpha L)^{-1}J^*\mathbf{V} \tag{4.2}$$

Where α is the regularisation parameter which is chosen before performing the calculation and L is the regularisation matrix, which for Tikhonov regularisation is an identity matrix of the necessary dimensions. However if information is already known about what σ should be, L can be modified to favour or penalise particular elements. This can also produce results which are misleading - see the section "Cheating with EIT" in Adler and Lionheart (2006) for more details.

A limitation of this method in the context of mortar and concrete NDT is the need for the user to choose and appropriate hyperparameter α. The quality of reconstruction when conductivity is so low relative to the available equipment is strongly dependent on the choice of the hyperparameter, as described in section 8.3. Additionally it does not appear that there is a reliable best setting for a given experimental configuration. This is an area where further work is needed before the technique can be applied to mortar and concrete bodies in which locations of defects are not known.

An image can be reconstructed from a single set of measurements (absolute imaging) but this is difficult in practice as it requires perfect correspondence between the computer model and experimental setup. Much more common is difference imaging, in which $\mathbf{V} = \mathbf{V}_1 - \mathbf{V}_2$ where $\mathbf{V}_1$ and $\mathbf{V}_2$ are two different sets of voltage measurements. Different voltage measurements may be the result of frequency dependent behaviour of materials within the boundary, as used in Frequency difference EIT (FdEIT) or some time-variance as in Time difference EIT (TdEIT).

The difficulty in time difference imaging is ensuring that the change which is interesting to the user is the only one represented in the measured data. For example, changes in the electrode position around the cylinder, changes in the impedance between the electrodes and the medium, or changes in the body shape (possibly as the result of introducing a crack) will all change the measurements in ways which may obfuscate the interesting feature. Some of these difficulties can be mitigated if FdEIT can be used, since in this case an image can be produced with two sets of data taken within a few minutes of each other. However FdEIT requires that the background and feature to be distinguished exhibit sufficiently different frequency dependence in their conductivity. It also is more sensitive to errors between the physical experiment and computer model than TdEIT.

For this work, a method equivalent to TdEIT was used. While there was no actual time variance in any of the cylinder cross sections, a plain background cylinder provided data that was compared to readings from the cylinders with inclusions. This method was used as opposed to physically modifying the cylinders to avoid producing GP dust, which requires some safety protocols. Image reconstruction was done in Matlab using functions from the EIDORS library (Adler and Lionheart, 2006) and the Distmesh FEM meshing tool (Persson and Strang, 2004), which provide tested and verifiable software for EIT imaging.

Two hyperparameters were used and the results compared to the known cross-section of the cylinders; the differences in results arising from these changes are shown and discussed. Additionally a simple method for combining the results of multiple image reconstructions, described in section 4.6.5, was applied and compared to the results of the individual image reconstructions.

4.6.5 Combining images produced using different reconstruction parameters

The following describes a simple method for combining several image reconstructions at different parameters into a single image.

This method is based on the observation that less noise-dominated (higher α) image reconstructions often give good contrast between an inclusion and noise-related artefacts, but are less useful for assessing the actual size and details of the inclusion. Conversely an image reconstructed with a lower α often has better

detail of the inclusion but more erroneous high contrast regions caused by noise. These noise regions cannot necessarily be distinguished from actual inclusions using only information present in a single image reconstruction. With this in mind a simple algorithm was developed to combine the relatively reliable low noise images with the higher detail of the high noise images, to improve usability and reduce the sensitivity to user selection of parameters.

The algorithm process is outlined below. The implementation used in this work was done in MATLAB and based on the EIDORS library, as with all of the image reconstruction. The process is based on repeated image reconstructions on the same FEM mesh, which is simplified by the EIDORS default behaviour of caching and reusing meshes unless the user requests a recalculation. It would be possible to apply the method to dissimilar meshes provided they had very similar levels of coarseness by correlating elements in each mesh based on their location, but this was not necessary for this work.

$\sigma_{n\ large}$ produced by retaining a percentage of the highest and lowest valued elements within each σ_n and setting all others element values to zero.
for *each element within the mesh* **do**
  if *Current element value is non-zero in each* $\sigma_{n\ large}$ **then**
    Element added to σ_{all}
  end
  if *Current element value is non-zero in any* $\sigma_{n\ large}$ **then**
    Element added to σ_{any}
  end
end
(Note that σ_{all} is a subset of σ_{any})
Set $\sigma_{combined} = \sigma_{all}$
while *new connected elements were found on the last iteration* **do**
  for *each element in* σ_{all} **do**
    if *element in adjacent to one in* $\sigma_{combined}$ **then**
      Element from σ_{all} added to $\sigma_{combined}$
    end
  end
end
Elements from $\sigma_{combined}$ shown on original mesh

Algorithm 1: Basic process for combining the results of several independent image reconstructions.

5 | Results of initial work imaging plaster and conventional concrete

This chapter describes and discusses the results of the initial work on imaging of dental plaster and concrete cylinders. The experimentation was intended to partially establish feasibility of Electrical Impedance Tomography (EIT) for concrete, or at least to show if the idea was completely infeasible given the available equipment, in service of the project's objective one.

Since it was known from the literature that EIT could be used on concrete, the experiment was primarily intended as a test of the available equipment and to develop a better understanding of the experimental challenges that would be encountered in the project. A secondary goal was reproduction of Frequency Difference Electrical Impedance Tomography (FDEIT) images.

5.1 EIT imaging of dental plaster cylinders

Initial imaging work was performed on dental plaster casts. The intent of the experiment was to produce images from four dental plaster cylinders containing resistive inclusions. This experimentation produced some reasonably good images and was an opportunity to develop understanding of the general process of EIT, particularly the relevant software and available equipment. This section describes the methods used in the work, followed by results and discussion. An illustration of the configurations of each of the plaster cylinders is given in Fig. 5-1.

Cylinder preparation was the bulk of the experimental work. Once this had been completed, data collection and image reconstruction were done using more standardised methods. The materials and methods used are described in detail in section 4.3.1.

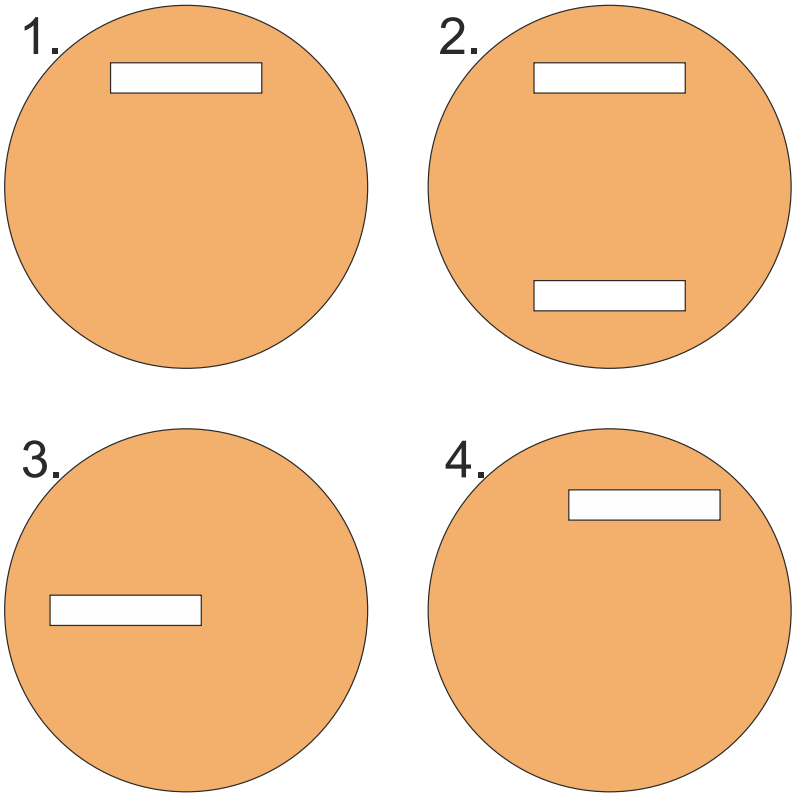

Figure 5-1: Numbered plaster cylinder cross sections.

5.1.1 Results

This experiment produced image reconstructions using Time Difference Electrical Impedance Tomography (TDEIT) and FDEIT.

Time difference imaging

A homogeneous cylinder was produced to serve as a background in order to facilitate TDEIT. Expectations for the quality of this were low due to some inconsistencies in electrode configuration resulting from the manufacturing, described in section 4.3.1. Measured frequencies were 10kHz, 50kHz and 100kHz. Representative results showing the difference between cylinder 1 and the homogeneous cylinder at 10kHz and 50kHz are shown in Fig. 5-2.

Discussion of the results is given in Section 5.1.2.

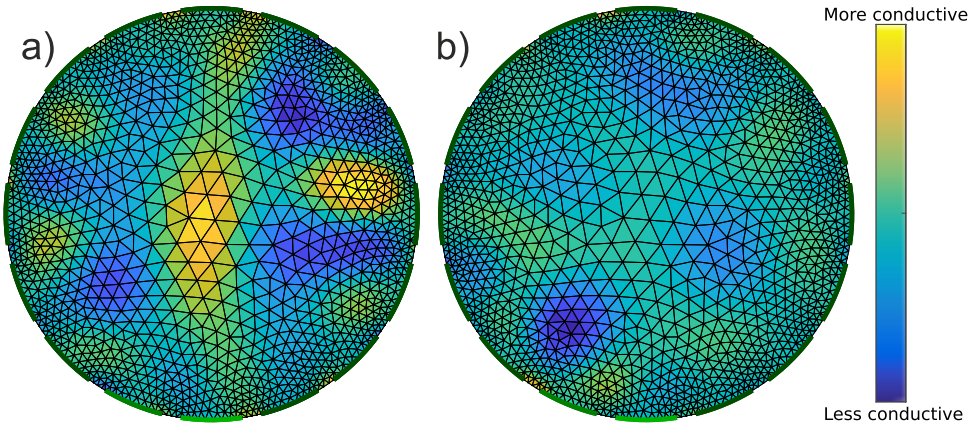

Figure 5-2: Examples of time difference imaging on the plaster cylinder 1. Image a) shows 10kHz, b) shows 50kHz. Both use $\alpha = 0.001$.

Frequency difference imaging

FDEIT was attempted since it would be less sensitive to electrode positioning errors. Fig. 5-3 shows four image reconstructions of cylinder 1 to illustrate some of the effects of changes to α as well as the result of using a larger frequency difference. Figs. 5-4, 5-5 and 5-6 show two frequency differences for cylinders 2, 3 and 4 respectively. Each of these images uses $\alpha = 0.001$.

5.1.2 Discussion and outcomes of EIT imaging on plaster cylinders

TDEIT was unsuccessful on in the dental plaster. Neither of the images in Fig. 5-2 reflects the actual cylinder, and this is representative of the other images that were obtained. This failure was expected to some degree due to the errors between electrode locations on the background and inclusion cylinders. It is also possible that the issue was exacerbated by plaster inhomogeneities.

In contrast several of the FDEIT images on the same cylinders are good representations. Images a), b) and c) from Fig. 5-3 all show resistive regions in the correct position and orientation, close to the first electrode and with the long axis of the region running roughly tangential to the boundary. The size in all cases is incorrect to some degree, with the slot width being exaggerated and the length too short in image b). Images a) and c) use the same data with α being lower in a) resulting in a more noise dominated image. As a result

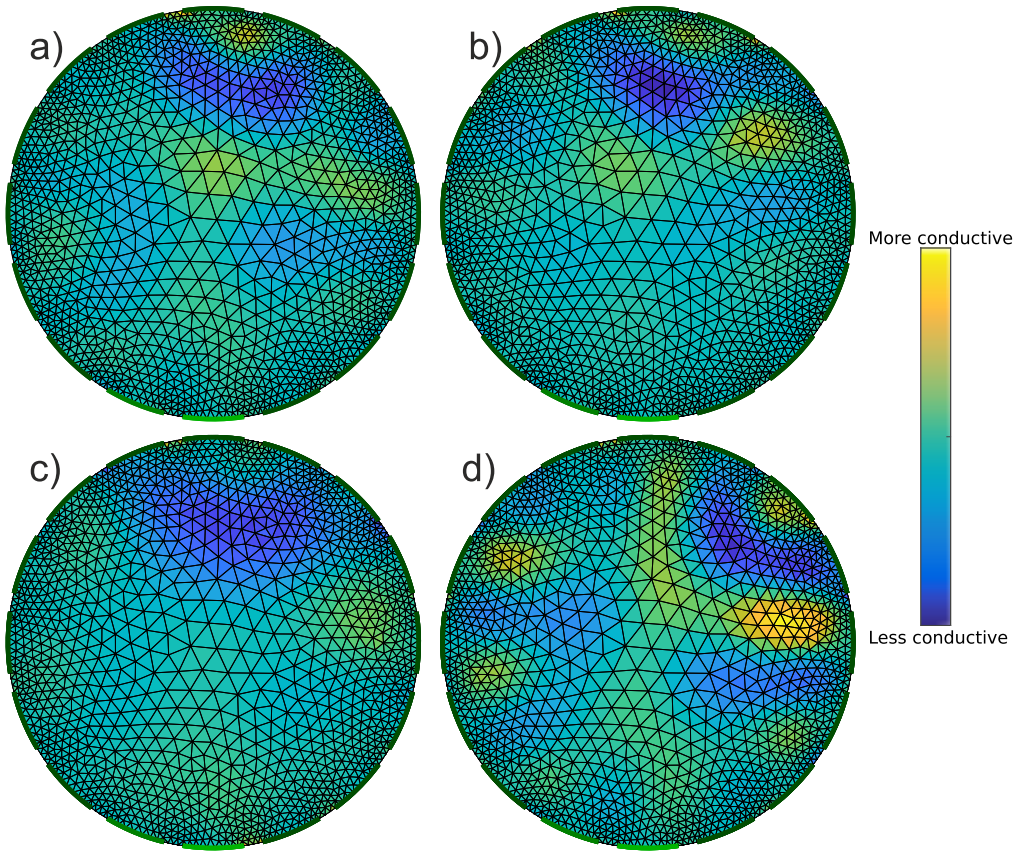

Figure 5-3: FDEIT on plaster cylinder 1. Image a) shows 10kHz vs 50kHz with $\alpha = 0.001$, b) shows 50kHz vs 100kHz with $\alpha = 0.001$, c) shows 10kHz vs 50kHz with $\alpha = 0.005$, d) shows 10kHz vs 100kHz with $\alpha = 0.001$.

image a) is a clearer representation of the slot size than c), but also includes several erroneous conductive regions which would potentially be misidentified by an observer without knowledge of the cylinder.

The images of cylinder 2 are not useful, and in fact are quite misleading. Neither of the slots are shown, but several erroneous regions are shown in both a) and b). It is interesting that image b) appears to be roughly the negative of image a) in terms of conductive vs. resistive regions. This would be expected in the case of a highly non-linear impedance frequency response. For example if $\mathbf{V}_{50kHz} > \mathbf{V}_{10kHz}$ and $\mathbf{V}_{50kHz} > \mathbf{V}_{100kHz}$ then in the ideal case the $\mathbf{V}_{diff}$ between 10kHz and 50kHz would be the negative of that between 50kHz and 100kHz, multiplied by some scale factor related to the difference between the impedances at 10kHz and 100kHz, resulting in the negative image. However none of the other

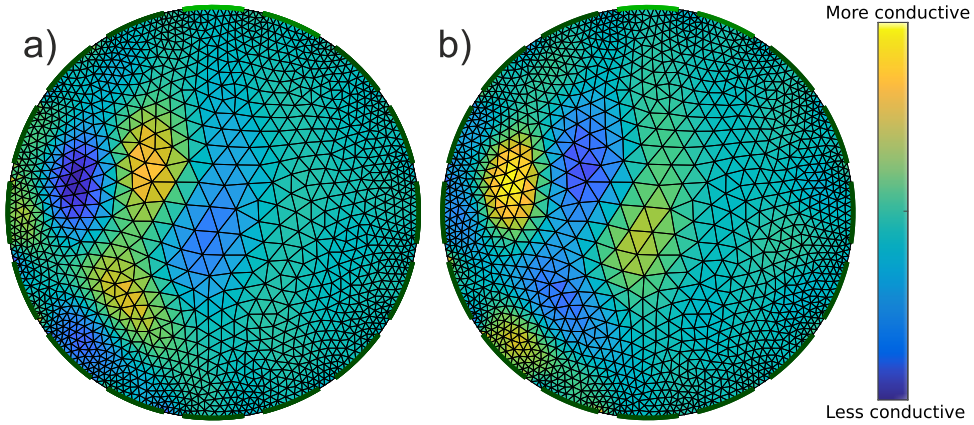

Figure 5-4: Plaster cylinder 2, a) shows 10kHz vs 50kHz, b) shows 50kHz vs 100 kHz. Both use $\alpha = 0.001$.

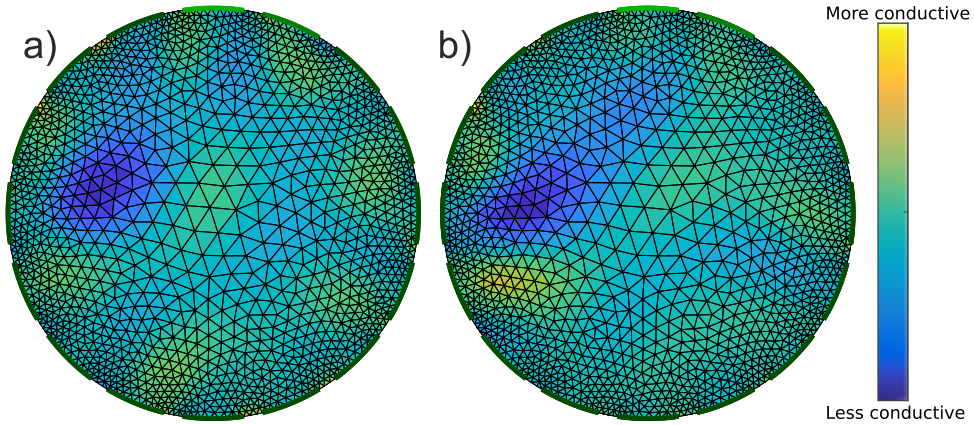

Figure 5-5: Plaster cylinder 3, a) shows 10kHz vs 50kHz, b) shows 50kHz vs 100 kHz. Both use $\alpha = 0.001$.

cylinders exhibit the same behaviour in the two frequency differences, and it is unknown what exactly caused the effect in this case.

Both of the images of cylinder 3 shown in Fig. 5-5 show the location and orientation of the inclusion well, although the size and shape are distorted. Image a) also doesn't show any significant erroneous regions.

Finally the images of cylinder 4 in Fig. 5-6 do not show any significant contrast in the appropriate location. Image b) appears to show a faint resistive region in the wrong place.

The experiment demonstrated FDEIT working on plaster. It also demonstrated some of the difficulties of applying EIT, even in a laboratory setting.

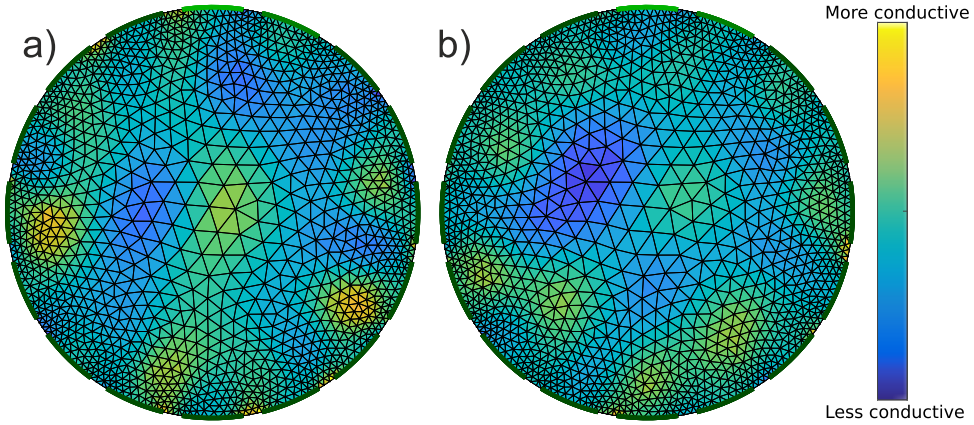

Figure 5-6: Plaster cylinder 4, a) shows 10kHz vs 50kHz, b) shows 50kHz vs 100 kHz. Both use $\alpha = 0.001$.

Some good images were obtained for cylinders 1 and 3. Cylinders 2 and 4 were not successfully imaged.

The experiment also showed the sensitivity of the results to choice of hyperparameter and frequency combination. This is an obstacle to adoption of EIT. However, it was observed that for the good images (one and three) the majority of parameters would produce something reasonable, and that the inclusion would generally be shown much more intensely than any noise until a very small hyperparameter was used. Some work has been done on using multiple images to alleviate this issue, described in Chapter 7.

Differences between the computer model and physical experiment also led to inaccuracies in images. Cylinder 2 was particularly uneven in its electrode positioning and this likely accounts for the failure to produce useful images of it.

Data was only obtained at three frequencies because of limitations of the Kyung-Hee University Mark 2.5 EIT machine (KHU Mk 2.5) and the electrode configuration. Comparing the two frequency difference images for each cylinder as well as the 10kHz vs 100kHz image for cylinder 1, it appears that larger differences and differences at higher frequencies do not necessarily produce better images. Therefore there is no reason to expect that data at higher frequencies would have produced better results in this case.

The electrode size was chosen from the perspective of manufacturing. Simulation using Electrical Impedance and Diffuse Optical image Reconstruction Software (EIDORS) suggested that the gaps between the electrodes were small

enough that the low impedance of the conduction path around the outside of the body would have distorted the results due to a lack of current penetration into the centre.

Going forward, the intention was to attempt to perform EIT on more realistic samples. The use of a dental plaster in place of concrete and the casting of electrodes into the samples were intended to improve the chances of obtaining good results. The use of FDEIT appeared to be feasible, and observations about the effects of electrode position and sizing were useful in subsequent work.

5.2 Initial imaging results using concrete

Following the imaging work on plaster cylinders, attempts were made to image three cylinders made from concrete. The intent of this experiment was to assess the possibility of using the available equipment for more realistic imaging. Therefore the cylinders and the circumstances of the measurements were intended to more closely represent an industrial use of Non-Destructive Testing (NDT). The bulk of the experimental work here was done on electrode attachment and image reconstruction.The materials and methods used are described in detail in section 4.3.2.

The cylinders had been manufactured several months beforehand and were as such close to or at the maximum resistivity that they would achieve (see section 3.2). Each cylinder had some configuration of either resistive or conductive inclusions (steel reinforcement or plastic piping) cast into them and did not incorporate electrodes in the same way that the plaster cylinders did. Less representative of an industrial usage case was the cylindrical shape, which is the ideal shape for EIT.

This work was useful for developing some understanding of electrode behaviours, but was ultimately unsuccessful in producing EIT images.

5.2.1 Results

Two distinct types of experiment were performed using these concrete cylinders. Experiments were done to optimise the way the electrodes were applied to the cylinders, followed by attempts at imaging them. Results of the electrode work

are presented first since they informed the method for the image reconstruction attempts.

Investigation of factors affecting impedance across electrode pairs

Two experiments were done to provide data to optimise the electrode configuration. The first test looked at the effects of pressure on the contact impedance, and the second looked at variation of contact impedance with time after the application.

Test of impedance magnitude across gel electrodes over time In the test on impedance across two gel electrodes over time, all of the measurements showed the same shape of the impedance frequency response but the magnitude of the impedance did vary significantly. A graph showing the magnitude of the impedance measured at 5kHz is presented in figure 5-7.

Based on these results it appeared that the optimal time to take measurements would be around 22 hours from the initial application of the electrodes.

Test of application of pressure to electrodes Another test was performed to determine whether or not added pressure would reduce the impedance across electrodes. Impedance across two gel electrode pairs was measured over time, one with some clamping pressure and one without. The measurements taken over the course of a few hours showed that the force did reduce the overall impedance across the electrodes. The results of the test are shown by figure 5-8.

The test showed some reduction in impedance from the pressure on the electrodes. The actual clamping pressure was not known, and the method of clamping used would not be practical for use on a full 16 electrode setup - a custom clamping jig would have to be produced.

The results of these tests influenced the procedure for subsequent tests.

Results of imaging on concrete

A background for these concrete samples was not available, so only FDEIT was attempted. Some representative results are given by Figures 5-9 to 5-11. While results were also obtained at using different reconstruction parameters they were of no better quality and are not presented here.

5.2.2 Discussion and outcomes of experiments on concrete cylinders

The EIT imaging attempts on the concrete cylinders available to the project were unsuccessful. The impedance of the concrete cylinders in use was much higher than that of the plaster cylinders, and it was concluded that this was the most likely cause of the difficulty of producing images. Other investigators who had some success performing EIT on concrete describe using early age concrete, which in general has lower resistivity (see Section 3.2.2) than the mature concrete used in the study.

The observations on electrode impedance were useful in later experimentation. However, the difficulty in obtaining useful results in a relatively realistic usage case using the available equipment informed the decision to proceed with investigations into concrete resistivity and imaging of conductive concrete.

5.3 Conclusions

The results presented in this chapter are grouped together because of their role in influencing the later direction of the project. The failure of the concrete imaging work to produce usable image reconstructions presented several options for subsequent work, and the study of conductive mortars was performed in order to facilitate EIT on the available equipment. The observations on electrode configuration and arrangement, and the image reconstruction process informed the later imaging work that was carried out, in the measurement configuration, data inversion, and observations on the effects of α led to the combination method proposed in section 8.2.5.

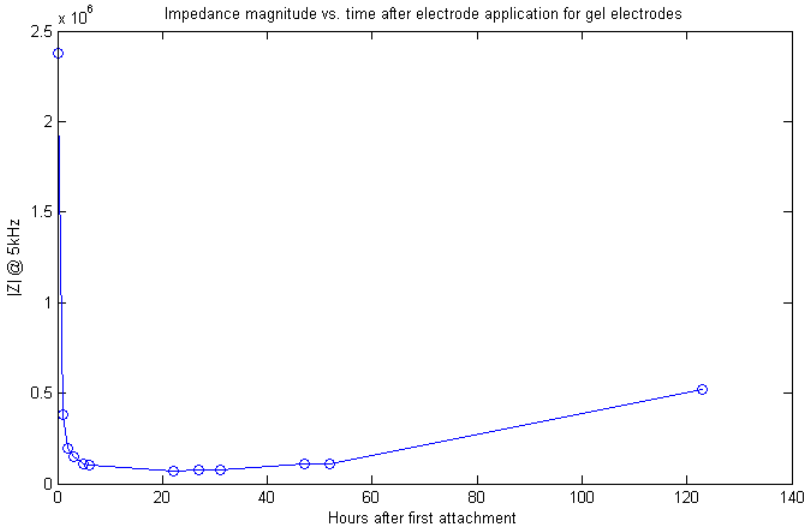

Figure 5-7: Impedance magnitude at 5kHz against time since electrode application.

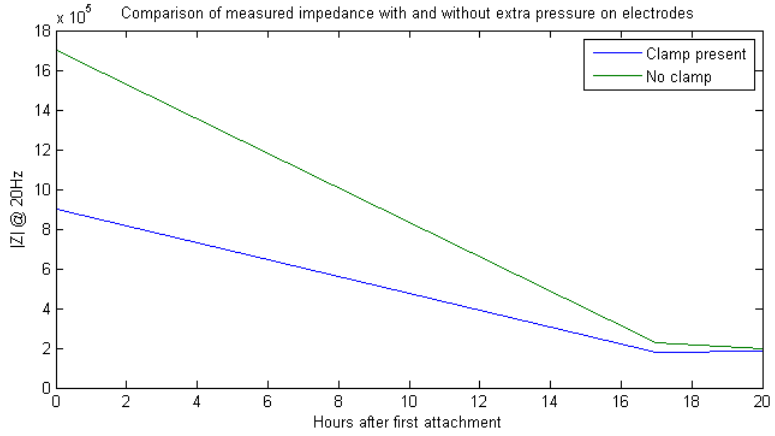

Figure 5-8: Impedance magnitude at 20Hz against time since application for two pairs of electrodes.

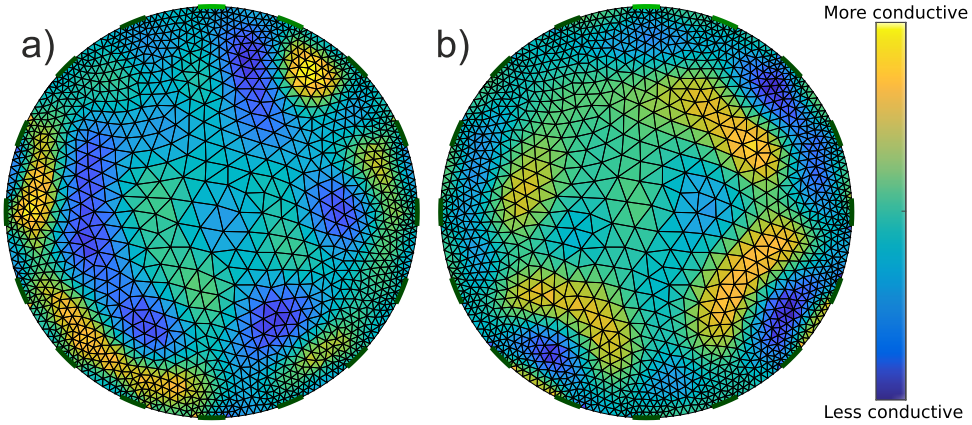

Figure 5-9: FDEIT image reconstruction of the concrete with the plastic pipe. Image a) shows 10kHz vs 50kHz, b) shows 100kHz vs 250kHz. Both use $\alpha = 0.001$.

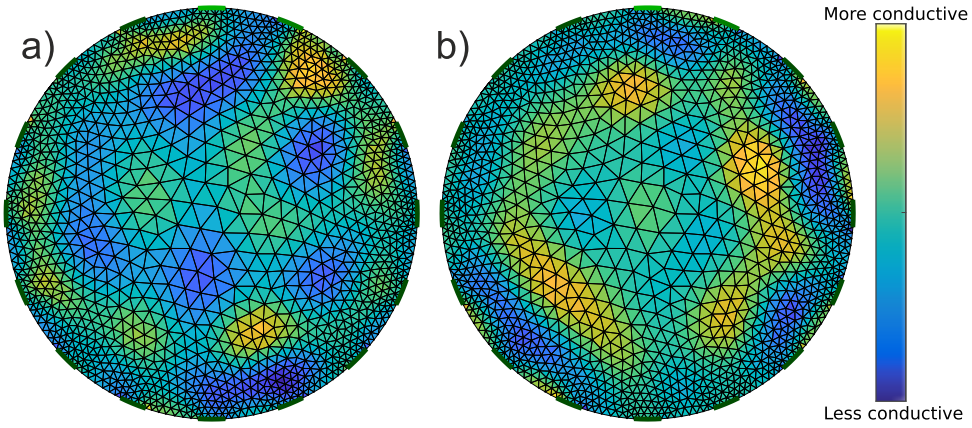

Figure 5-10: FDEIT image reconstruction of the concrete with one piece of metal reinforcement. Image a) shows 10kHz vs 50kHz, b) shows 100kHz vs 250kHz. Both use $\alpha = 0.001$.

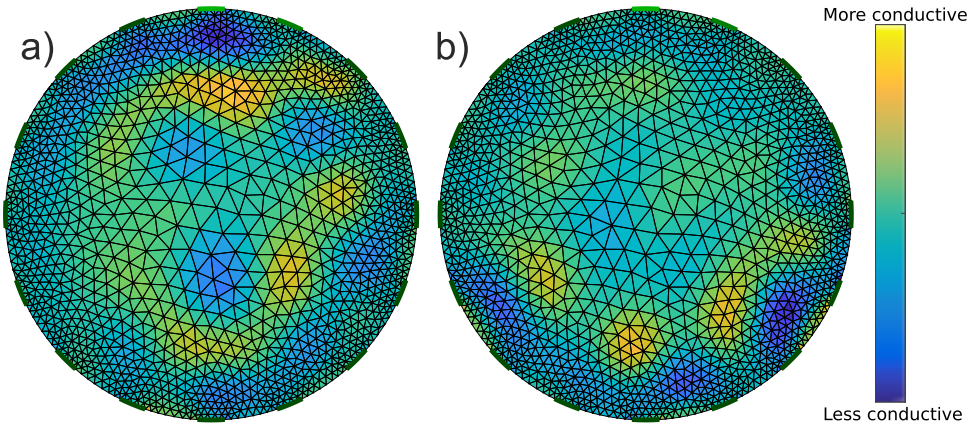

Figure 5-11: FDEIT image reconstruction of the concrete with two pieces of metal reinforcement. Image a) shows 10kHz vs 50kHz, b) shows 100kHz vs 250kHz. Both use $\alpha = 0.001$.

6 | "A multi-variable study of factors affecting the complex resistivity of conductive mortar"

Following the difficulty in imaging of concrete, it was decided to proceed by producing conductive mortar cylinders for imaging - a decision described in Section 1.2. A literature search found some examples of this, described in section 3.2.3, where concrete resistivity was modified for various purposes using conductive additions. However no detailed information on the complex resistivity of the resultant materials was available. There was also a gap in the literature on the effects of other mix parameters on complex resistivity in mortars.

The decision was made to perform a more comprehensive investigation into complex resistivity of conductive mortars, and to publish the results to help any other investigators producing conductive mortars and concrete for any application. Because the value of the work was not restricted to facilitating Electrical Impedance Tomography (EIT), it is mentioned only briefly in the paper. This work fulfilled objective two of the project.

As mentioned in Section 1.2.1 and the paper itself, mortar was substituted for concrete for practical reasons, and this was believed to be justified since the cement paste is really the only part of a structural concrete in which the electrical properties can be controlled.

The accepted manuscript is largely unedited except to integrate it into the thesis formatting. Figures have been resized, and some of the graphs have been altered to make lines easier to distinguish. An additional paragraph discussing safety issues associated with the use of carbonaceous powders is included in the methods section. Some other additional information been added for clarity; this

is italicised to distinguish it from the published text. Some typographical errors have also been fixed. The bibliography has been integrated into that of the thesis. The methods from this paper are reproduced in Section 4.4.

This declaration concerns the article entitled:									
A multi-variable study of factors affecting the complex resistivity of conductive mortar									
Publication status (tick one)									
Draft manuscript		**Submitted**		**In review**		**Accepted**		**Published**	✓
Publication details (reference)	Magazine of Concrete Research (ICE)								
Candidate's contribution to the paper (detailed, and also given as a percentage).	The candidate contributed to/ considerably contributed to/predominantly executed the... Formulation of ideas: The idea to comprehensively study the factors affecting mortar resistivity came from S. Davey (70%) following the suggestion that conductive mortar would be of some use for the project by K. Paine (15%) and M. Soleimani (15%). Design of methodology: Methodology was designed by S. Davey (90%) with suggestions and checks from K. Paine (10%). Experimental work: All experimental work was performed by S. Davey (100%) after some advice from lab staff. Presentation of data in journal format: Data analysis and visualisation and writing was performed by S. Davey (80%). Comments were provided by K. Paine (15%) and E. Tzoura (5%) whose contribution is acknowledged in the text.								
Statement from candidate	This paper reports on original research I conducted during the period of my Higher Degree by Research candidature.								
Signed					**Date**				

The final published version is available in: A multi-variable study of factors affecting the complex resistivity of conductive mortar, Stephen Davey, Kevin Paine, and Manuchehr Soleimani. Magazine of Concrete Research 2020 72:13, 681-692.
Available online via: https://doi.org/10.1680/jmacr.18.00394

Abstract

Twenty four mortar mixes have been tested to assess the effects mix design factors on complex electrical resistivity. Of these mixes, 6 were conventional and 18 were conductive mixes containing varying quantities of either graphite or carbon fibre powder additions, which have been shown in previous studies to reduce the resistivity of cementitious materials. Complex resistance measurements from 20Hz-10MHz taken between 7 and 35 days after casting were analysed. Comparisons were made between the effects on complex resistivity of varying quantities of additions, water/cement ratio (w/c), and grit/sand ratio (g/s). In conventional mixes w/c was found to have more significance for complex resistance than g/s. Conductive additions were found to reduce complex resistivity magnitude as well as the influence of other mix factors. This novel and comprehensive comparison of the effects of three elements of mix design on complex resistance will be of use to anyone wishing to produce mortars or concrete for use in self-heating, self-sensing, or electrical property imaging contexts.

Keywords

Cement/cementitious materials; Composite materials; Electrical properties

6.1 Introduction

In some applications, it may be advantageous or necessary to design concrete with the intent of controlling its electrical properties. The resistivity of conventional concrete varies significantly with its saturation level, but for dry concrete a value of 10^6 Ω·m is typical (Hornbostel et al., 2013). This compares to metals which generally have resistivity in the order of 10^{-7} or 10^{-8} Ω·m. Therefore reducing the resistivity is likely to be the more common usage case for efforts to control the electrical properties of concrete.

One example of an application of conductive concrete is self-heating concrete, as described by Tumidajski et al. (2003), Z. Hou et al. (2010), Maleki et al. (2017) and others. In this application, the conductive concrete dissipates energy by heating when a current flows through it. The principal use for this is in de-icing

of pavement or road surfaces.

Conductive concrete has also been studied as a potential material for electromagnetic shielding by Ogunsola et al. (2009) and Khalid et al. (2017). In both studies the resistivity of the concrete was decreased by the addition of conductive materials. J. Zhang et al. (2017) demonstrated the possibility of using conductive concrete to produce grounding electrodes for use in components of power networks.

Another major application for conductive concrete is for assessment of damage via structural health monitoring – so-called "Self-sensing" concrete. Ding et al. (2015) measured the change in resistivity of conductive concrete as a method for detecting damage caused by freeze/thaw cycles, and found that the relationship between resistivity change and number of cycles was quite consistent. Their results also show that conductive additions may have desirable effects on the mechanical properties of the concrete. Chu and Chen (2016) compared the relationship between resistivity versus strain for conductive concrete during cyclic loading, showing that damage can be detected by observing changes to the resistivity.

Another potential application is the production of concrete that can be more easily imaged using electrical property measurement techniques similar to those described by Ammari et al. (2014) and Hallaji et al. (2015). This has been explored by B.S. Huang et al. (2016).

The list of substances that may be useful as additions given by Xie et al. (1995) is relatively comprehensive. More recently other carbonaceous materials have been considered, including graphite powder, carbon nanofibres and carbon nanotubes (Gomis et al., 2015) and carbon fibre reinforced polymer (CFRP) (Maleki et al., 2017). From the results presented by Gomis et al. graphite powder and carbon fibre powder have varying effects on the resistivity of cement paste depending on the moisture content of the mix, but variations in w/c in that study make it difficult to isolate the effects of the carbonaceous materials. In the same study the nanofibres and nanotubes had a profound effect with the nanotubes reducing resistance in their dry test specimens by four orders of magnitude compared to the same weight percentage of carbon fibre powder, though again the w/c ratio was not held constant.

Z. Hou et al. (2007) investigated the DC resistance of concrete with 5-10mm

long carbon fibres as conductive additions, finding that for concretes with a constant dosage of 0.73% by mass of carbon fibre, increasing the content of coarse aggregate decreased resistance. Chen et al. (2017) also used carbon fibre powder combined with graphite powder, with several different combinations of the two materials up to 7.75% by mass of cement showing around 10 to 11.5 Ω·m before any cyclic loading. This was reduced by the gradual application of a compressive stress up to 30MPa, and then consistently reduced by around 10% compared to the original value after returning to the no-load state. This represented around an order of magnitude decrease in resistivity as compared to dry conventional concrete.

Gomis et al. found that with 5% by mass of carbon nanotubes, the DC resistivity of the concrete mix was 0.23 Ω·m, and for the same quantity of carbon nanofibres 7.45 Ω·m. This is a particularly low value for a conductive concrete, but cannot be used to compare the two materials directly as other mix parameters were also varied. They also found that resistivity for the two concrete mixes were not significantly affected by moisture content, compared to the same weight percentage of carbon fibre powder and graphite powder. This suggests that the nanotubes and nanofibres were better distributed in the concrete matrix, and conduction paths were not reliant on the cement.

Steel fibres may be vulnerable to corrosion in the same way that concrete reinforcement is, which would affect their electrical properties and as such they are not preferred in this application. Carbon nanotubes have a profound effect on resistivity according to Gomis et al. but due to their present cost it is unlikely that they will be adopted for use in industrial contexts in the short to medium term. Therefore, graphite and carbon fibre powders were selected for testing in this research.

The purpose of this work was to assess the relative effects of the water-to-cement ratio (w/c), fineness of the fine aggregate and weight percentage of carbonaceous materials (WPCM) on the resistivity of several mortar mixes. Mortar has been used since it provides the dominant conduction path in concrete, particularly at lower frequencies. In each mix, two of these variables were held constant while the other was varied. Avoiding coarse aggregates eliminated the possibility of variability caused by the distribution of the aggregates, at the cost of some direct applicability to concrete. However, the data obtained remains useful in designing

conductive concretes.
In this work the complex resistance (Ω), a property of the particular component being measured, of a number of mortar cubes was measured using an impedance analyser. These resistance measurements were converted into resistivity (Ω·m), an intrinsic property of a type of material, using the physical measurements of the mortar cubes. *Complex resistance differs from simple resistance in that it accounts for difference in phase between voltage and current. Thus "Complex resistivity" is used here to specify that both the ratio of magnitudes and phase difference between voltage and current are being accounted for, and that knowledge of the dimensions of the cubes is being used to convert into an intrinsic material property.*

6.2 Research significance

In order to make an informed decision when producing conductive concrete, it will be necessary to understand the effect that choice and quantity of carbonaceous material as well as other parameters of the mix design will have on the electrical properties of the mix. This comparison of the effects of parameters of a conductive mix design on its complex resistivity will be useful for the production of conductive mortars and concretes for the applications mentioned in section 6.1.

6.3 Materials, methods and equipment

6.3.1 Materials

The aim of this research was to investigate how mortar resistivity changes with the presence of a carbonaceous material (CBM) addition whose only purpose was to reduce resistivity magnitude. Two other factors common to all mortar mixes - relative quantities of different aggregates, and water to cement ratio - were also considered. No plasticisers were used.
A Portland fly ash cement, CEM II/B-V 32.5 N conforming to BS EN 197-1, was used for all mortars. Two natural fine aggregates conforming to BS EN 12620 of differing particle size distribution were used to assess the effect of fineness of fine aggregate. The grading of both fine aggregates is shown in Figure 1. The finer of

the two aggregates was an alluvial sand (s), whilst the coarser fine aggregate was a Marlborough grit (g). The two fine aggregates were combined in g/s ratios of 0.6 to 1.2. This represents a change in fineness (expressed as percentage passing the 500 μm sieve) of 36.5% to 50% by mass. Grading of the aggregates is given in Figure 6-1:

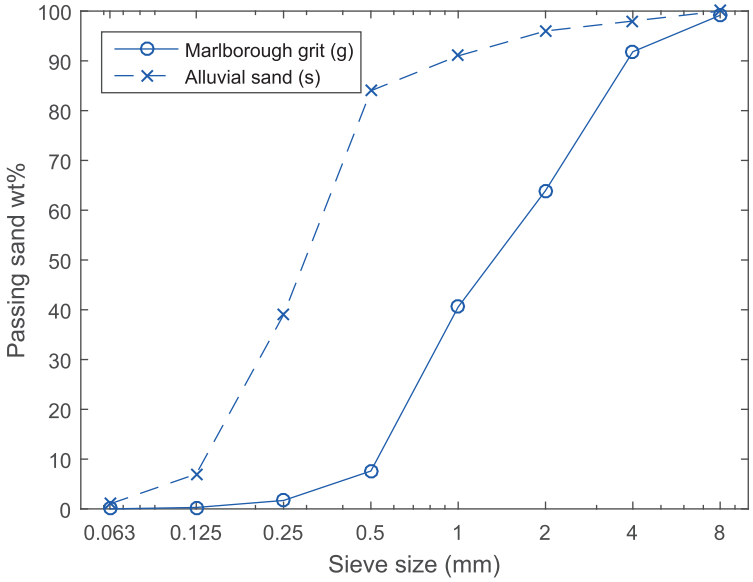

Figure 6-1: Particle size distribution of the fine aggregates.

The CBMs selected were: milled carbon fibre powder (CFP) and graphite powder (GP). The CFP was typically greater than 5 μm in length and less than 3 μm in diameter. The particle density was approximately 1800 kg/m^3. The particle size of the GP was such that 85% passed a 44 μm sieve. The particle density was approximately 1900 kg/m^3. *Conductivity of the CBMs was not provided by the manufacturer and was not measured due to the safety concerns described below.*

Working with these carbonaceous powders presents health risks beyond those usually encountered when preparing cementitious materials. The Material Safety Data Sheets (MSDS) were obtained for both CFP and GP from the manufacturer. These indicated essentially the same safety considerations for both materials: protection of skin, eyes, and the use of a dust mask to prevent skin, eye and respiratory irritation. In practice, both materials were found to become airborne very easily. The powders were supplied in large tubs; opening the lid to a

tub was enough to produce a small dust cloud. Therefore the personal protective equipment was used at all times when handling the powders, and other measures were taken to reduce the amount of powder that became airborne, as described in Section 6.3.2.

Details of the 24 mixes used are given by Table 6.1. *One cube was manufactured per mix.*

				Mass ratios relative to cement			
Mix ID	CBM	WPCM	g/s	w/c	s/c	g/c	CBM/c
1	None	0	0.8	0.70	1.67	1.33	0.00
2	None	0	0.8	0.80	1.78	1.42	0.00
3	None	0	0.8	0.90	1.89	1.51	0.00
4	None	0	0.6	0.80	2.00	1.20	0.00
5	None	0	1	0.80	1.60	1.60	0.00
6	None	0	1.2	0.80	1.45	1.75	0.00
7	CFP	1	0.8	0.90	1.73	1.42	0.05
8	CFP	3	0.8	0.90	1.63	1.42	0.14
9	CFP	5	0.8	0.98	1.54	1.42	0.24
10	CFP	9	0.8	1.06	1.30	1.42	0.48
11	CFP	4	0.8	1.04	1.44	1.33	0.22
12	CFP	5	0.8	1.17	1.63	1.51	0.26
13	CFP	4	0.6	1.14	1.76	1.20	0.24
14	CFP	5	1	1.11	1.36	1.60	0.24
15	CFP	5	1.2	1.08	1.21	1.75	0.24
16	GP	1	0.8	0.90	1.73	1.42	0.05
17	GP	3	0.8	0.90	1.63	1.42	0.14
18	GP	5	0.8	0.90	1.54	1.42	0.24
19	GP	9	0.8	1.14	1.30	1.42	0.48
20	GP	5	0.8	0.95	1.44	1.33	0.22
21	GP	5	0.8	1.00	1.63	1.51	0.26
22	GP	4	0.6	1.16	1.76	1.20	0.24
23	GP	5	1	0.90	1.36	1.60	0.24
24	GP	5	1.2	1.08	1.21	1.75	0.24

Table 6.1: Table of mixes tested.

6.3.2 Preparation of mortar specimens

A series of 24 mortar mixes were produced. Ratios of the different fine aggregates were intended to correspond to the range of fine aggregate finenesses used

in concrete. *Water to cement ratios were chosen largely for practical reasons with a high water content used to maintain workability, which was found to be decreased by the presence of CBM, to facilitate mixing.* The sand to cement ratio ranged from 3 to 3.4 in all mixes and the w/c ratio ranged from 0.7 to 0.9 for the non-conductive mortars and from 0.9 to 1.2 for mortars containing CBM. Higher w/c ratios were used for the CBM mortars because it was found that this was necessary to maintain consistence and properly mix the materials. Whilst it may have been possible to use lower w/c ratios by use of water-reducing admixtures, as will be likely when conductive concrete is produced for practical applications, this would have increased the complexity of the mixes and may have obfuscated the effect of w/c on conductivity in this parametric study.

CBM was added to the mortars in proportions of 1 to 9% by mass of mortar; which represents approximately 5 to 32% by mass of cement + CBM.

Mixing was carried out by hand. Prismatic specimens of 40 x 40 x 48mm were cast for each mix. Slight variations in length were allowed and accounted for in electrical property calculations. Fine aggregates and cement were mixed together before the addition of water. The manner in which the CBM was added differed when using CFP or GP. CFP preliminary mixes with relatively low WPCM showed that initially dispersing the CFP in water was a viable way of reducing some of the safety risks associated with the powder. When making the higher WPCM mixes this practise was found to lead to flocculation of the powder and extra physical mixing had to be done to mitigate this effect. In contrast the GP was found to float in the water, so was added directly with the fine aggregates and cement, with the safety risks being addressed with personal protective equipment.

The specimens were placed in a controlled environment room (20°C, 40% RH) for 24 hours. All specimens were demoulded at 24 hours and stored in water at 20°C until an age of 35 days.

6.3.3 Electrical measurements

Measurements were taken using an Agilent E4990A impedance analyser. Each mortar cube was removed from the water and surface dried using a cloth before measurements were taken. Surface temperature was not controlled when out of

the water. These temperatures were not used in the analysis but are included in the online data for the study.
Measurements were taken at 7, 14, 21, 28, and 35 days after casting the mortar. Stainless steel electrodes were clamped to the cubes and connected to the impedance analyser using the four-terminal pair probe configuration described by Agilent Technologies (n.d.) section 3.1.4, as shown in Figure 6-2.

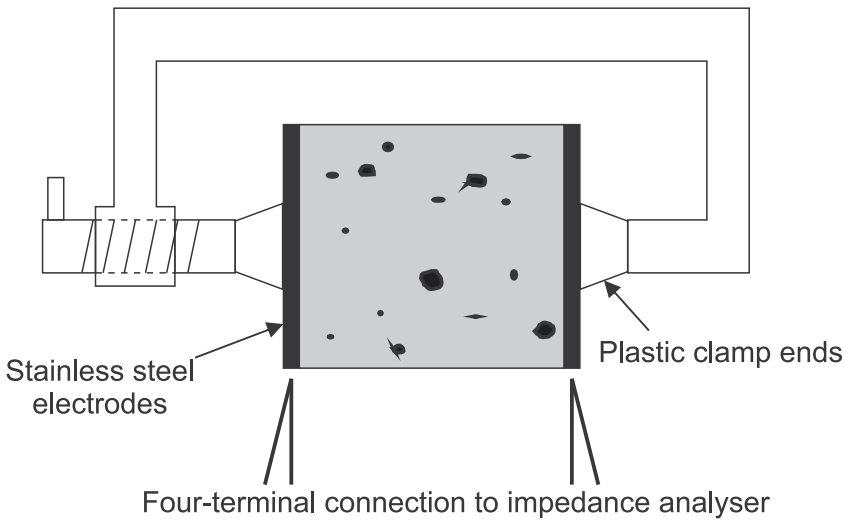

Figure 6-2: Mortar cubes as clamped and connected to measurement equipment.

The initial set of measurements was taken at 200 frequencies within the 20Hz-20MHz range, using a linear frequency sweep. For subsequent measurements the scheme was changed to use 1000 frequencies in a logarithmic sweep to better represent the response at lower frequencies. A complete measurement set for each cube took no more than two minutes. Measurements above 10MHz were found to be significantly affected by the measurement probes in use. These were discarded.
Some particular combinations of mixes and times have not been presented in this paper where they are not pertinent to comparisons being made, but all of the data produced for the research is available online - see the data access statement for details.

6.4 Results and discussion

Comparisons of measurements showing the impact of three factors on the resistivity of mortar are presented. Nyquist plots show the frequency response for some mixes, as well as graphs and tables showing variation in individual frequency resistivity values. Results are separated between those pertinent to electrical properties at 35 days, and during the hydration process.

6.4.1 Conventional mortar results

This section deals with the complex resistivity of non-carbonaceous mortar in order to provide a baseline. As the mixes were not typical of industrial mortars, and did not contain some of the materials used in commercial contexts, they cannot necessarily be taken as representative of all mortar. However they are useful as a comparison with the conductive mortars.
The complex resistivity of non-carbonaceous mortar has been studied by McCarter (1994) and others. Figure 6-4 shows the frequency response for mix 1, which exhibits behaviour consistent with that previously reported for mortar. This response consists of an electrode arc, dominated by electrode contact effects, up to a frequency of around 10kHz. Above this frequency the bulk arc is observed, which is the result of capacitive behaviour of the mortar matrix.

Mix properties of conventional mortar and resistivity at 35 days hydration

Figure 6-3 shows resistivity values for non-carbonaceous mixes at 35 days after casting. Mix 2 (w/c=0.8, g/s=0.8) is also compared to mixes 4 and 5 to consider the effects of varying the g/s ratio.

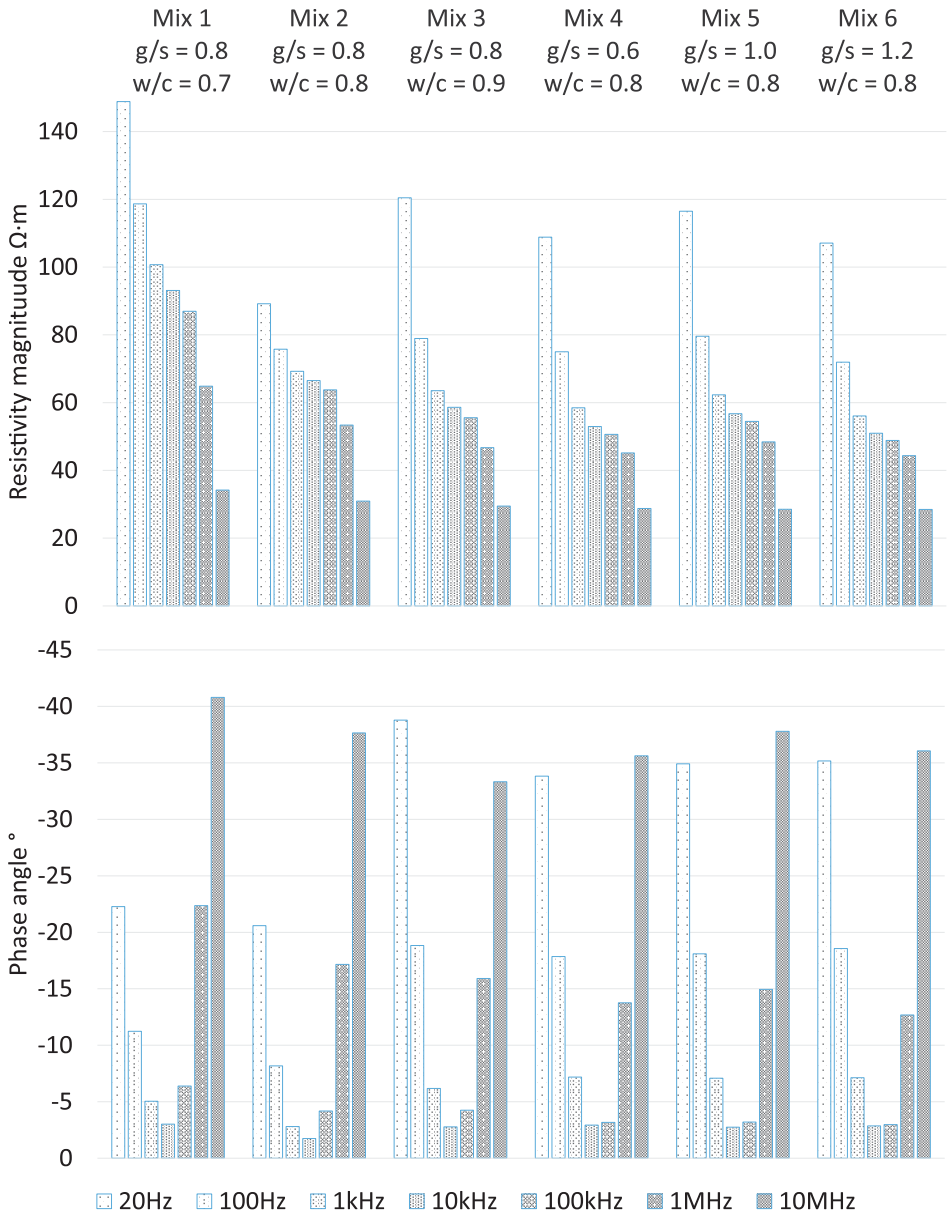

Figure 6-3: Resistivity of non-carbonaceous mixes at 35 days after casting.

Figure 6-4 shows a Nyquist plot for mix 1 taken at 35 days after the initial casting. This was a typical response for mortar, showing a clearly defined bulk and electrode arc. Figures 6-5 and 6-6 show the frequency responses for the non-carbonaceous mortar mixes taken at 35 days after casting. Different markers show order of magnitude increases in frequency, from 20Hz to 10MHz - the same markers are used in all following Nyquist plots, and measurements at these order

of magnitude frequencies are used to compare mixes.

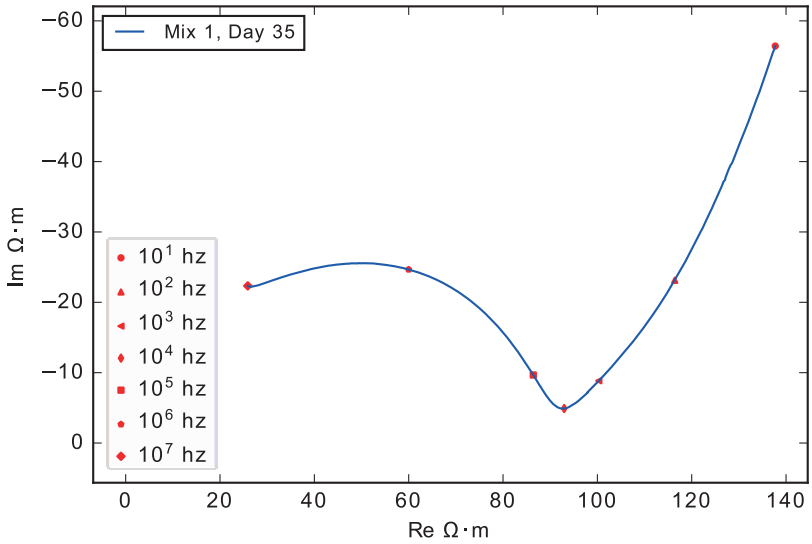

Figure 6-4: Nyquist plot for mix 1: g/s = 0.8 w/c = 0.7 WPCM = 0. Markers indicate order of magnitude change for frequency.

Varying the ratio of grit to sand in the mortar from 0.6 to 1.2, as shown in Figures 6-3 and 6-6 changed the final $|Z|$·m by an average of 2.9% *(*1.7 Ω·*m)*and a range of 3.0 percentage points *(*2.7 Ω·*m)* over the order of magnitude change frequencies with the largest *percentage change,* −4.1% *(*2.4 Ω·*m) occurring at 1kHz and the largest absolute change of* 3.1 Ω·*m (*−4.07%*) occurring at 100Hz.* For the phase shift the average was −1.2% *(*0.2°*)* with a much larger range of 11.7 percentage points *(*2.4°*)*.
For comparison, changing the water to cement ratio from 0.7 to 0.9, also shown in Figure 6-3 as well as Figure 6-5 produced an average $\Delta|Z|$·m of −29.2% *(*−27.7 Ω·*m)* and an average change in phase shift of −10.7% *(*1.3°*)*. This relatively small number of data points suggests that changes to the water to cement ratio have a more significant effect on the resistivity of mortar than altering the proportions of non-conducting aggregate components.

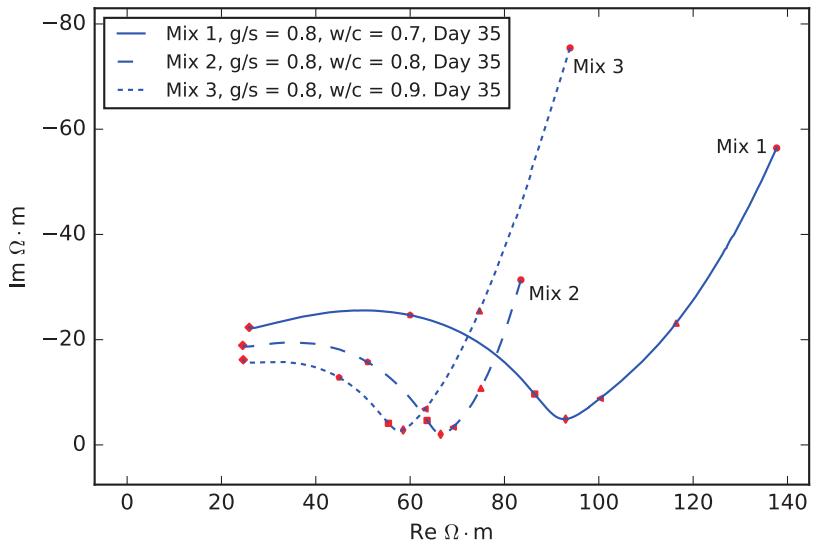

Figure 6-5: Nyquist plot showing the effect of varying w/c ratio on complex resistivity at 35 days.

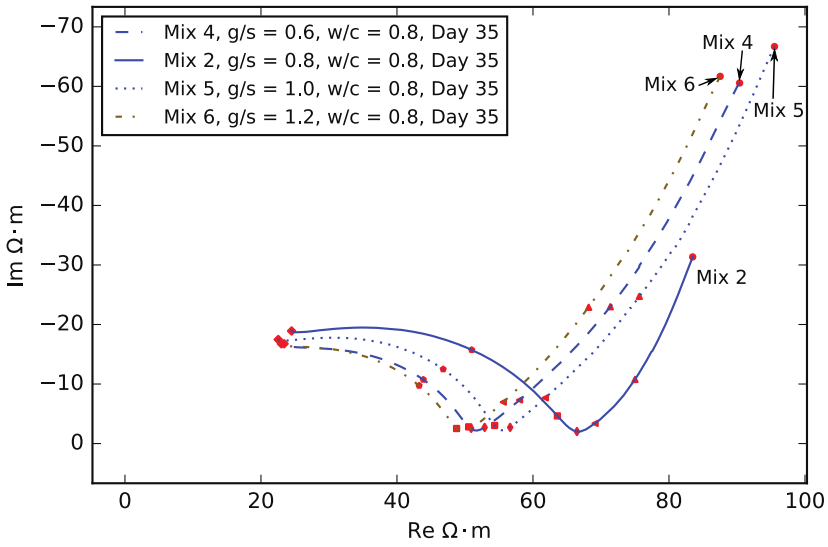

Figure 6-6: Nyquist plot showing the effect of varying g/s ratio on complex resistivity at 35 days.

Mix properties of conventional mortar and resistivity from 7 to 35 days age

Figure 6-7 shows the percentage change between measurements taken at day 7 and day 35. Fewer spot frequencies were used in the 7 day measurements than in subsequent sets. The results show that the resistivity generally increased over the course of the hydration process, although mixes 1 and 5 showed a small reduction in resistivity at low frequency. Changes to the phase angle over the hydration process were small.

Forde et al. (1981) found that the resistivity of conventional concrete and cement paste increased exponentially until around 20 days of curing, and then continued to increase linearly at a gradual rate thereafter. This study did not assess whether or not the resistivity change until 20 days was exponential.
There was a general trend towards an increase in resistivity magnitude over time, especially at higher frequencies, as observed in mixes 1 to 6. This behaviour was not always observed, and in some cases the day 21 resistivity magnitude was the highest measured, with the other data exhibiting the expected behaviour. This does not correlate with the variations in temperature measured on the cubes during testing, and may instead be the result of variation in clamping pressure on the electrodes.

6.4.2 Complex resistivity of conductive mortar at 35 days

The conductive mortar mixes were the main focus of the study. This section deals with the resistivity of the conductive mortar mixes at 35 days of hydration. Two aspects of the results are considered here: (i) the effects of different mix parameters on resistivity magnitude and shape of the frequency response in conductive mortars, and (ii) differences between the two conductive additions used. Since the differences between GP and CFP were found to be relatively similar in effects (see section 6.4.2) and GP appears slightly more often in the literature, it is presented as the "baseline" addition.

Effects of changes in WPCM, g/s, and w/c on complex resistivity

Figure 6-8 shows resistivity values for mixes with varying WPCM, measured 35 days after casting. The results consist of a general decrease in resistivity mag-

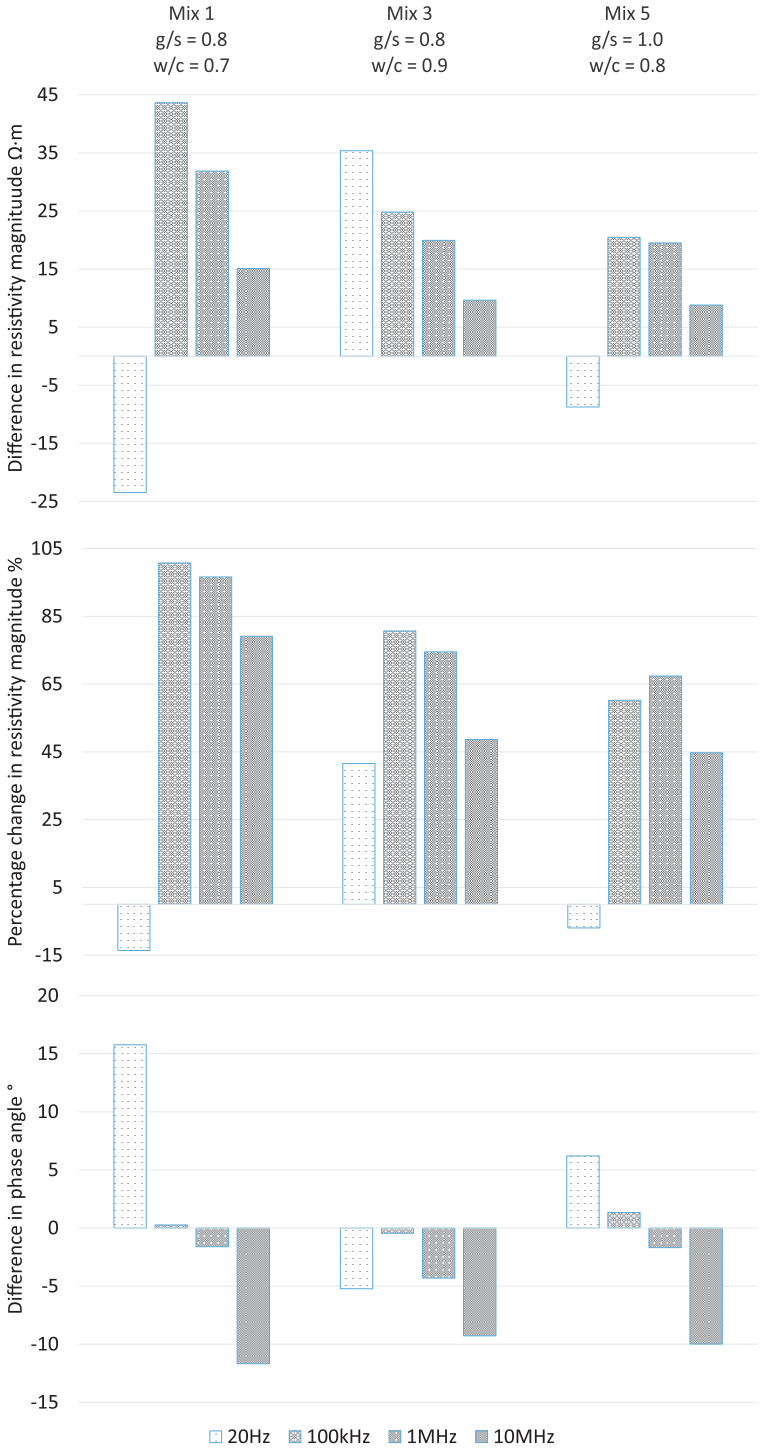

Figure 6-7: Change in complex resistivity at 7 and 35 days after casting, for mixes 1, 3 and 5.

nitude as WPCM was increased, for all frequencies. Resistivity magnitude for each mix decreased as frequency was increased in all cases. At frequencies below 10kHz the resistivity was actually increased between 1% and 3% WPCM, and at frequencies below 1kHz the same behaviour was observed between 1% and 5% WPCM.
After around 35 days of hydration previous work has shown that there is little further change to the mortar resistivity (Forde et al., 1981). Measurements from this stage were used to compare the effects of variation in the other mix parameters in conventional and conductive mixes.

Table 6.2 shows the change in measured complex resistivity caused by the maximum changes to each mix parameter. The maximum differences in w/c and g/s in the conventional mortars and WPCM in the GP mortars are presented. The changes have been averaged over the order of magnitude frequencies to compare the overall effect of each factor. W/c and g/s are compared in the conventional mortar mixes, and WPCM is compared using mortars containing graphite powder.

Table 6.2: Differences in complex resistivity over parameter changes, averaged over order of magnitude frequencies.

	w/c = 0.9 to 1.1	g/s = 0.6 to 1.2	WPCM = 0 to 1
$\Delta\|Z\|$·m	-27.72	1.73	-32.65
$\Delta\theta°$	1.28	0.16	3.62
	WPCM = 0 to 3	WPCM = 0 to 5	WPCM = 0 to 9
$\Delta\|Z\|$·m	-27.45	-40.40	-57.48
$\Delta\theta°$	-3.13	-2.15	8.90

Figure 6-9 shows the development of the frequency response across mix 3 and mixes 16 to 19, representing content of GP from 0% to 9% by mass, with less variation in other variables. In contrast, Figure 6-10 shows the variation when the GP content was kept at 4% by mass while other parameters were altered. The two graphs show stronger variation in Ω·m as a result of changes to WPCM than other parameters.

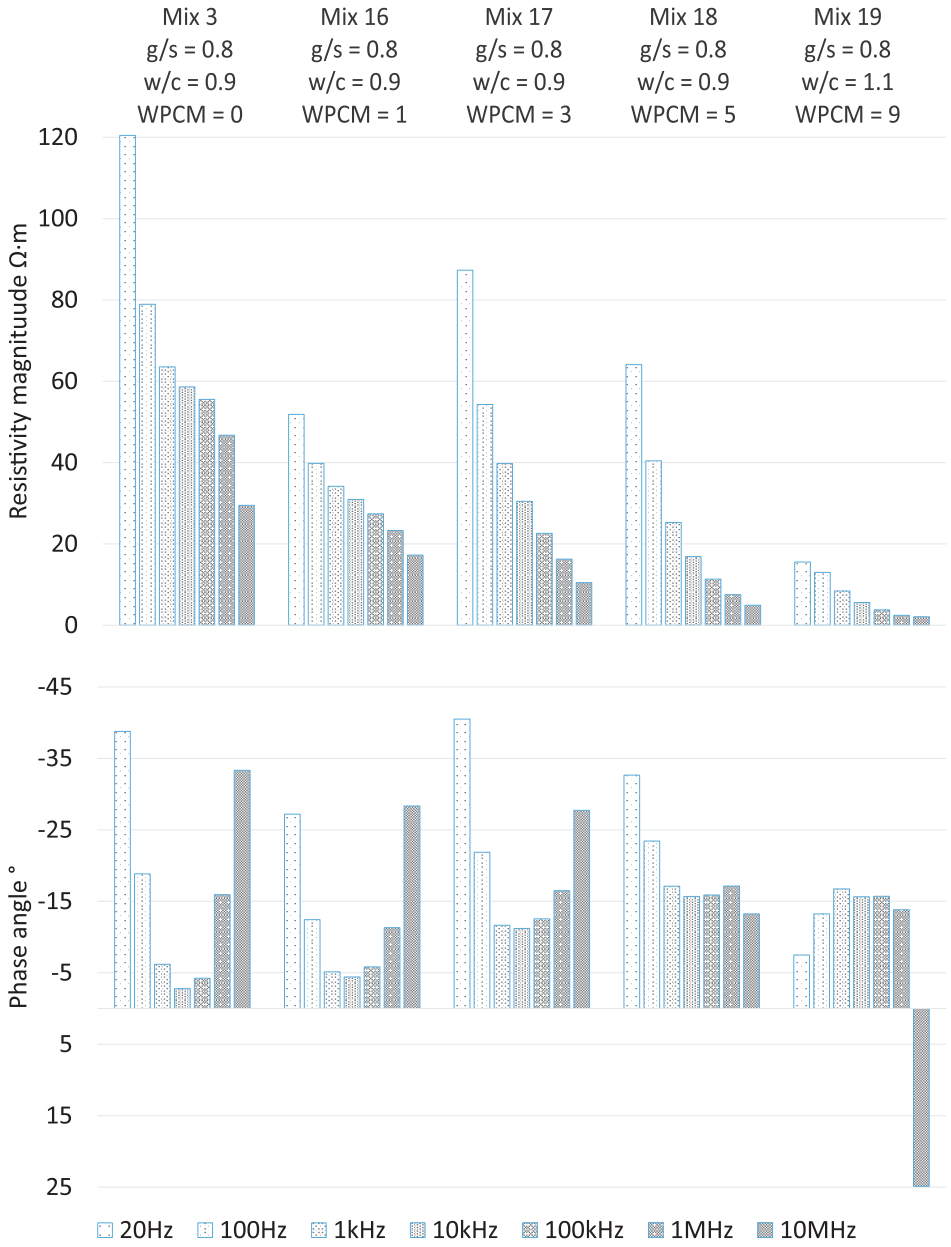

Figure 6-8: Complex resistivity of Graphite Powder mixes at 35 days after casting.

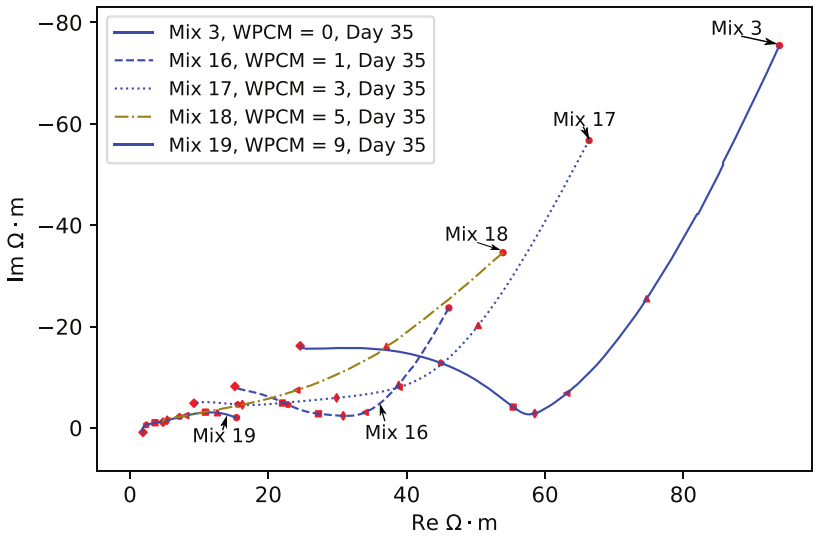

Figure 6-9: Nyquist plot showing the effect of varying GP content at 35 days.

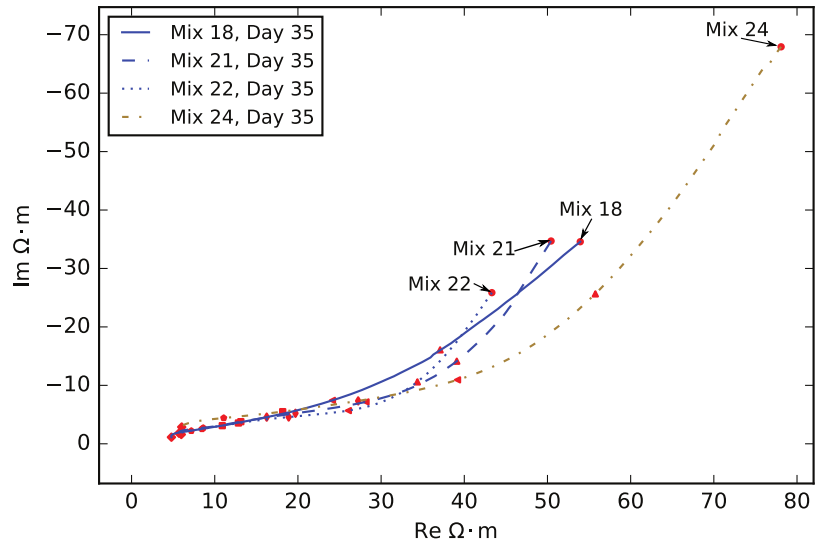

Figure 6-10: Nyquist plot showing the effects of varying w/c and g/s with constant 4% GP content at 35 days.

Figure 6-9 shows the effect of varying WPCM on resistivity for the mortars containing graphite powder. For comparison Figure 6-5 shows variation in w/c, and Figure 6-6 shows variation in quantities of grit and fine sand in non-conductive mortars. Table 6.2 is presented to give a condensed idea of the change

caused by each of the variables tested in the study.

The change from w/c = 0.7 to w/c = 0.9 produced a change from 93.1 Ω·m to 58.6 Ω·m at 10kHz. Figure 6-6 shows an unexpected effect of changes to g/s, where g/s = 0.6 and g/s = 1.2 were relatively close together and g/s = 0.8 had a somewhat differently shaped frequency response. This may be due to differences in the distribution of the grades of sand. If the results are taken to be representative, the largest change in resistivity magnitude at 10kHz was between g/s = 0.8 at 66.5 Ω·m and g/s = 1.2 at 50.1 Ω·m.

Water to cement ratio was varied from 1.0 to 1.2 (mixes 9 and 12) with a constant mass of CFP, and from 0.9 to 1.0 (mixes 18 and 21) with a constant mass of GP. In both cases the variation in measured resistivity was relatively small. Between mixes 9 and 12 the resistivity changed by an average of −3.3 Ω·m with a phase change difference of 2.4°. The difference was smaller between mixes 18 and 21, which follows from the smaller change in w/c. For this case the resistivity changed by an average of 1.0 Ω·m with a phase change difference of 0.06°. An increase of 0.2 in the w/c of the conventional mortars led to an average change of 27.7 Ω·m and 1.3°.

Varying the grit to sand ratio from 0.6 to 1.2 in mixes containing 5% CFP by mass (mixes 13 and 15) led to an average resistivity magnitude change of 0.03 Ω·m and phase shift difference of 1.7°. This average change in resistivity magnitude represented 1.2% of the $|Z|$·m for mix 13. For the same change in the GP case, the average change in resistivity was 15.8 Ω·m, with a phase shift difference of 5.6°. For comparison, the average difference in resistivity from the g/s variations in the conventional mixes was 1.7 Ω·m.

Figures 6-5 and 6-6 show the changes made to the frequency response by altering the ratios of water to cement and grit aggregate to sand in mixes with no CBMs. Figure 6-10 shows the effects of similar alterations when CBM quantity was held at 4%. Changes to w/c and g/s have very little effect on the shape of the complex resistivity frequency response of the mortar. In the non-conductive mortars this is shown by Figures 6-5 and 6-6, in which the basic electrode arc/bulk arc shape was maintained consistently in spite of changes to resistivity magnitude. In contrast, Figure 6-9 shows a large change in the shape of the Nyquist plot as WPCM was increased. The electrode and bulk arcs became less distinct until the response shape consisted of a single arc, ending in a region characterised by an

increase to imaginary resistivity with very little change to real resistivity. Figure 6-10 shows that changes to w/c and g/s had a similarly small effect on the shape of the Nyquist plot in mixes with a conductive addition.
Table 6.2 shows that at 35 days hydration the 3% WPCM graphite powder mix (mix 17) had a larger mean resistivity magnitude than the 1% mix (mix 16). Figure 6-11 shows this in more detail, and Figure 6-12 shows similar effects in the carbon fibre powder mixes. In the GP case the 1% WPCM mix had an unexpectedly low resistivity magnitude below 10kHz, and in the CFP case the same was true below 1kHz. In both cases the progression from 3% WPCM onwards was as expected i.e. a reduction in resistivity magnitude at all frequencies. The unexpected behaviour of the 1% WPCM mix may have been due to differences in the distribution of the additions within the individual mortar cubes or due to some effect of the additions on the hydration process.
Alterations made to the g/s and w/c parameters of conductive mortar have a small effect on the resistivity of the mortar, when compared to changes to the WPCM or to changes to those same parameters in conventional mortar. The practical result of this is that when considering the complex resistivity of a conductive mortar designed using carbonaceous materials, the addition is the primary concern. Further work is needed to determine if materials such as plasticisers have an effect closer in scale to that of the carbon powders than w/c and g/s.

Comparison of graphite and carbon fibre additions

Figure 6-11 shows resistivity magnitude against frequency for different weight percentage of graphite powder. Figure 6-12 shows the same for carbon fibre powder.

Figure 6-13 shows the Nyquist plots for mixes 3 and 7 to 10, representing CFP content of 0% to 9% by mass. Figures 6-9 and 6-13 can be used to compare the difference in effects on Nyquist plot shape between the two types of addition.

Figures 6-11 and 6-12 present $|Z|\cdot$m at order of magnitude change frequencies for different weight percentages of GP and CFP, while Figure 6-8 gives the complex resistivity including phase shift of the graphite powder filled cubes measured at 35 days.
The results for the graphite and carbon fibre powders were generally relatively close for the same WPCM, though this varied depending on frequency. The 9%

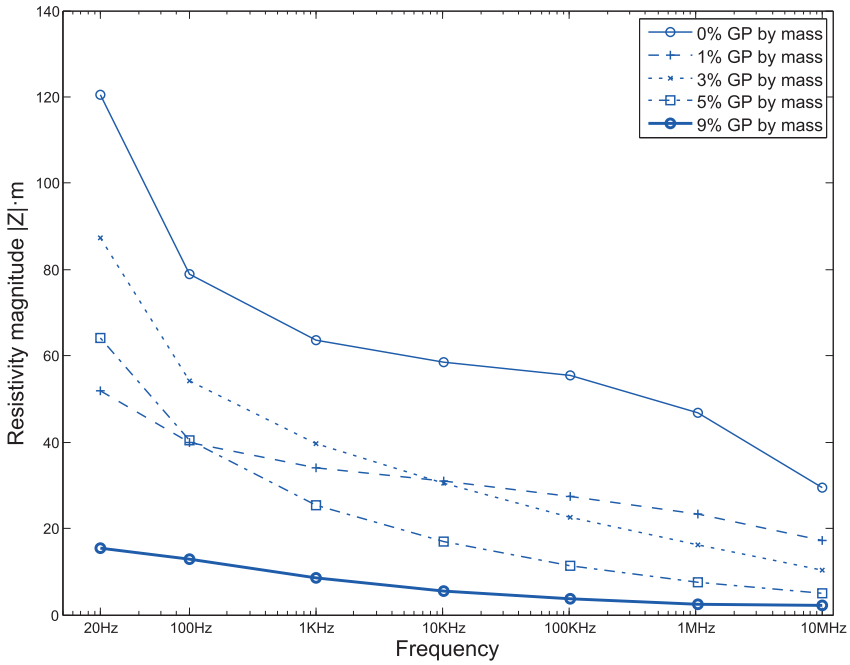

Figure 6-11: Stimulation frequency vs. resistivity magnitude for different weight-percentages of GP at 35 days.

WPCM case was the closest, with an average difference of 1.5 Ω·m across the order of magnitude frequencies. It should be noted that this still represented a significant percentage difference because of the overall low resistivity at this WPCM. The most significant difference was in the 1% case at 20Hz, in which the CFP mortar had a smaller resistivity magnitude by 25.7 Ω·m, corresponding to 49.5% of the GP resistivity magnitude for that frequency. Other than this there was only one other case (WPCM of 1% at 100Hz) of an absolute difference of more than 10 Ω·m. Differences in phase shift were also relatively small, with the largest being 12°.

The differences in spot measurements between the GP and CFP were of similar magnitude to those resulting from changes to g/s and smaller than those for changes made to w/c. It is also important to consider that the two CBMs were mixed differently *(see section 6.3.2)*, and this may account for some of the difference in resistivity.

A comparison of Figures 6-9 and 6-13 shows the difference in the shape of the frequency response of the two types of conductive mortar. The effect of increasing WPCM was very similar in both cases. Each of these sets of responses was

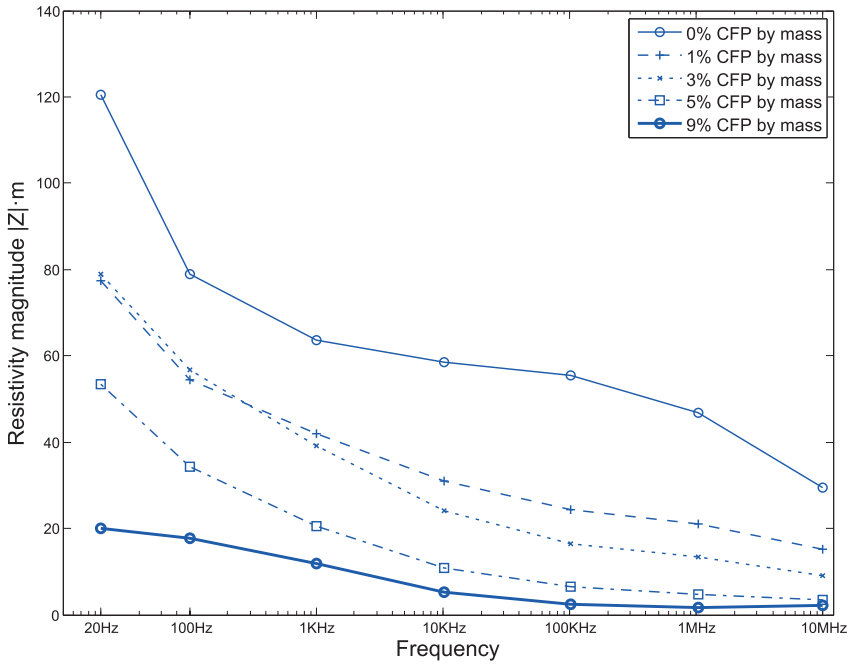

Figure 6-12: Stimulation frequency vs. resistivity magnitude for different weight-percentages of CFP at 35 days.

dominated by the carbonaceous material, as evidenced by the very minor effects of the changes to the other parameters. It is therefore reasonable to expect that the differences in shape of frequency response reflected either differences in the frequency response between the two materials, or differences in the distribution of particles within the mortar matrix.

6.4.3 Conductive mortar over the hydration process

Time development of the resistivity of mortar is related to the hydration process. It has therefore been studied for use as an indicator of the mechanical properties of a mortar at a particular point in time. This section compares the time development of Ω·m in mortar with and without carbonaceous materials.
Figure 6-14 shows the complex resistivity of a non-CBM mortar (mix 1) generally increasing over the hydration process.

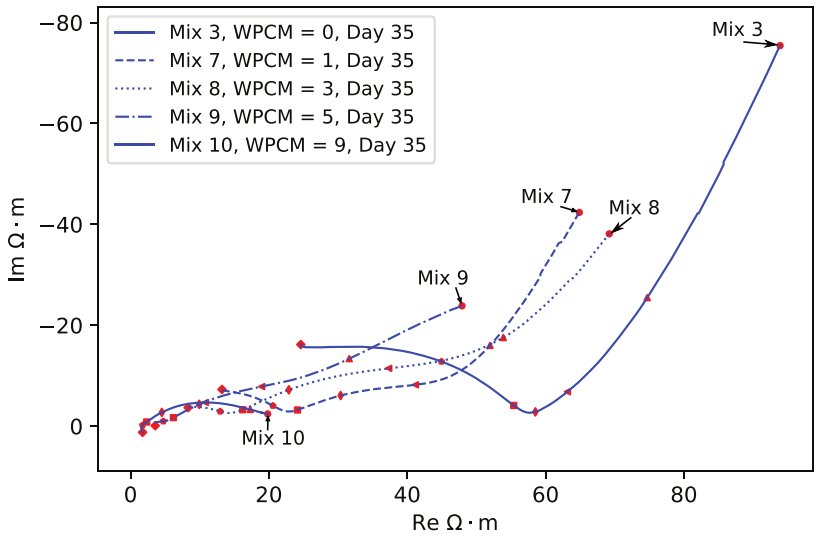

Figure 6-13: Nyquist plot showing the effect of varying CFP content at 35 days.

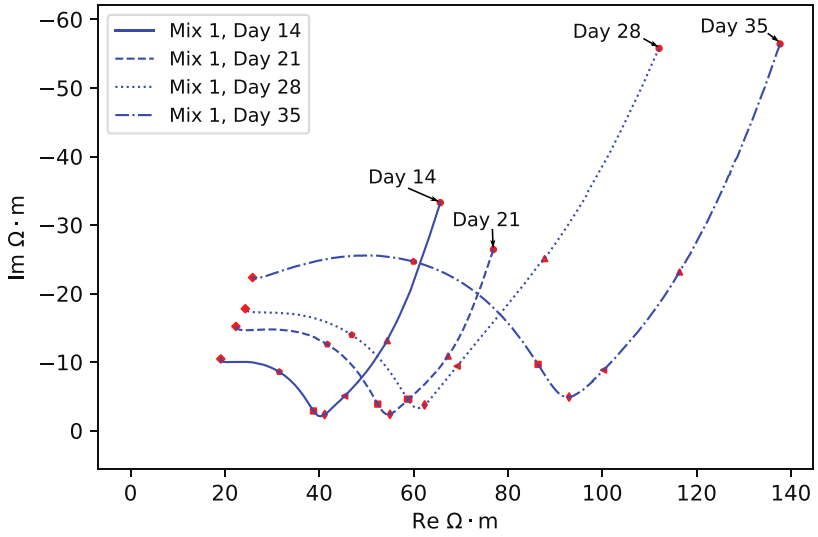

Figure 6-14: Nyquist plot showing effects of age on complex resistivity for a mix without conductive additions.

Figure 6-15 shows the resistivity of a 9% WPCM GP mortar (mix 19) over the hydration process.

Figure 6-16 gives an indication of the effect of the addition of carbonaceous materials on the time dependence of the resistivity of mortar.

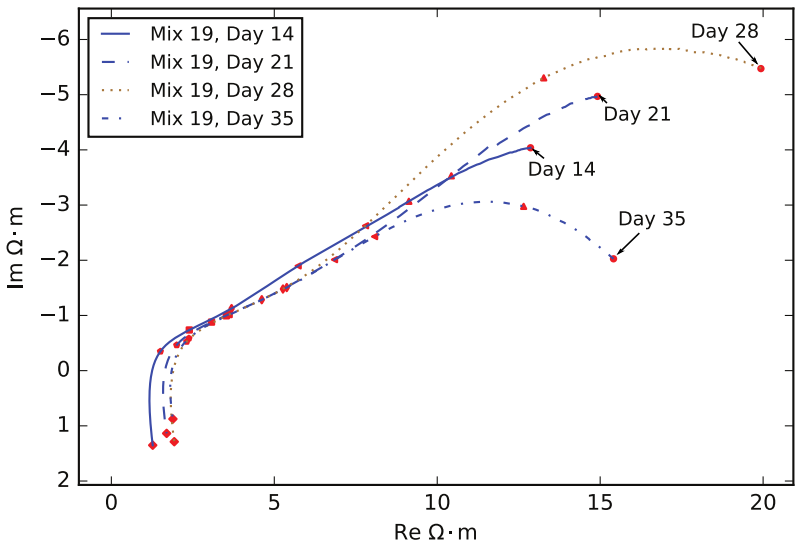

Figure 6-15: Nyquist plot showing effects of age on complex resistivity for a mix with 9% GP by mass.

Figure 6-14 shows that the resistivity of the shown non-CBM mortar increased over time, which is consistent with previous findings (Forde et al., 1981). In the CBM infused mortar the change in resistivity over time, as shown for a high-CBM case by Figure 6-16, would be expected to be less significant than than the standard mortar, because the CBMs which dominate the conduction behaviour are not believed to be affected by the chemical processes associated with curing. Figures 6-14 and 6-15 show that neither mix 1 nor mix 19 underwent substantial change to the shapes of their Nyquist plots during hydration. However it is immediately clear that the change in Ω·m was much less significant in the high-CBM case than the non-CBM case. Use of electrical properties to indicate progress in the hydration process can therefore be expected to be much more difficult in a conductive mortar than a conventional one. However, small variations of complex resistivity with hydration stage were observed even at the highest WPCM, especially at low frequency as shown in Figure 6-16. It is possible that there remains scope for correlating resistivity with hydration stage given sufficiently sensitive equipment.

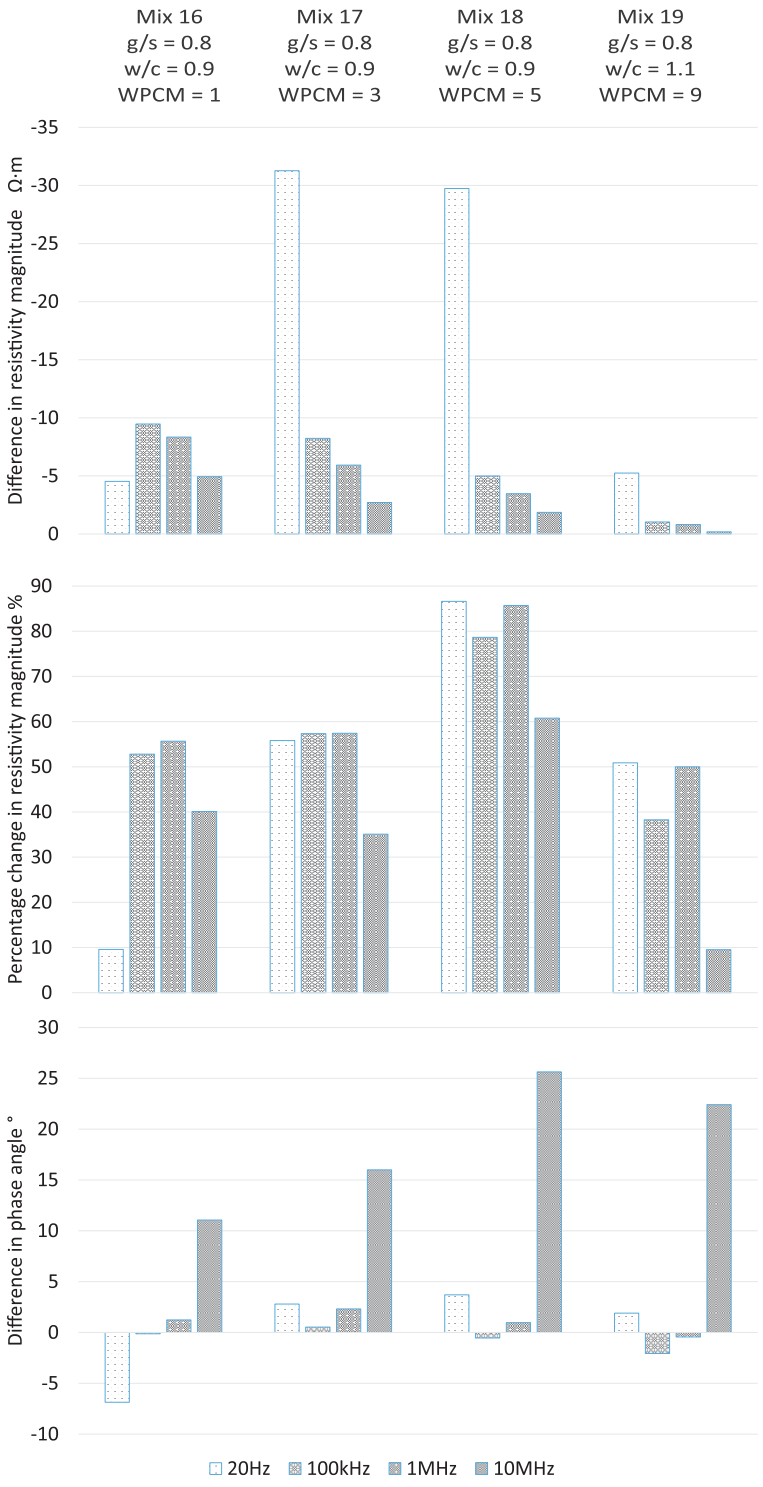

Figure 6-16: $\Delta\%$ between complex resistivity measurements on mixes 16, 17, 18 and 19 taken at 7 and 35 days after casting.

6.4.4 Mortars and concrete

This study has assessed the resistivity of mortars for practical reasons. Therefore there is the question of how well this information could be applied to concrete. McCarter (1996) measured the resistivity of both cement pastes and concrete. The findings in that case were that in general mortars and concretes would respond to changes to the same parameters in similar ways. However the addition of the large aggregates made a significant difference to not just the magnitude of resistivity but also to the characteristics and shape of the frequency response.
In spite of this, information on altering the electrical properties of mortar will inevitably be of some use for producing concrete. At lower AC frequencies or when applying DC, the mortar paste will provide the dominant conduction path. The interface between the concrete and any electrical measurement equipment will also primarily be comprised of mortar paste.
Use of conductive mortar pastes in concrete may also affect the durability of the concrete. Reduced resistivity may facilitate the flow of harmful ions such as chlorides and sulphates into the concrete body, causing reinforcement to deteriorate. Further research is necessary to determine whether the conductive mortar affects the appropriate usage cases of the concrete.

6.5 Conclusions

Complex resistivity data for mortars containing varying mix parameters including quantities of carbonaceous materials have been presented. From this data it is clear that changes to the quantity of carbonaceous material present had a greater effect on resistivity than these changes to the water or aggregate content of the mix. The general effect of a graphite powder addition has been found to be similar to that of carbon fibre powder. Though the difference between resistivity magnitudes when comparing mixes using the two additions was small, some differences in the shape of the frequency response were observed. If this shape difference can be ignored for a particular application, the decision on which option to choose can be made based on other factors than effect on complex resistivity. Separately from resistivity effects, both additions tested were found to increase the necessary water content of the mix in order to mix properly. Potential users

should be aware of this when working with these conductive additions.
The range of g/s tested roughly reflected the extremes of what is practical. W/c values were high to facilitate mixing, but the range in ratios was similar to the range that would be found in practically useful mortars. The data shows that of the two other mix factors varied, changes over these ranges to the w/c ratio have a greater effect on resistivity than changes to aggregates. Neither factor caused any change to the shape of the frequency response. In a conductive mix the effects of changes to the other mix parameters on resistivity are reduced further compared to the non-conductive mixes. The presence of carbonaceous powders in the mortar reduced the effect of the hydration process on resistivity, even with relatively small quantities of powder. All of these outcomes are consistent with the dominant electrical conduction path shifting from the cement to the dispersed CBMs in the mortar.
Overall the WPCM has been shown to be the most important factor for attempting to control the resistivity of a mortar. This has been demonstrated with two materials which are relatively affordable. The literature identifies other materials which are more effective at reducing resistivity, and therefore very likely to render other factors of the mix even less important.
These results on mortar will also be of interest to those investigating controlling the electrical properties of concrete. Further work is perhaps needed to understand the effects of conductive mortar on the complex resistivity characteristics of concrete. Further work is also necessary to assess the way a conductive mortar may affect the durability of concrete, especially in regards to reinforcement.

Acknowledgements

The authors would like to thank EPSRC for their support via grant EP/L016869/1. EPSRC had no direct role in carrying out this work. The work was also supported by a University of Bath research scholarship. Dr. Efi Tzoura is thanked for her comments on this manuscript.

Data access statement

Data collected during this study is freely available at https://doi.org/10.15125/BATH-00434 Where more data has been collected than used, this is made clear and justified in the article text.

6.6 Supplemental work

The preceding chapter is presented, except with small edits, as it was originally published. This section includes information and work not included in the journal paper due to format requirements.

6.6.1 Alternative table of mixes

Table 6.1 gives the mix proportions of each mix mostly in terms of the mass ratio of each material to cement. To aid reproducibility, the same information is given by Table 6.3 with the quantity of each dry material given as a percentage of the overall mass of dry materials.

				Weight percentage of dry material (%)			
Mix ID	CBM	WPCM	w/c	% Sand	% Gravel	% Cement	% CBM
1	None	0	0.70	41.66	33.33	25.01	0.00
2	None	0	0.80	42.32	33.87	23.81	0.00
3	None	0	0.90	42.93	34.35	22.72	0.00
4	None	0	0.80	47.62	28.57	23.81	0.00
5	None	0	0.80	38.10	38.10	23.81	0.00
6	None	0	0.80	34.63	41.56	23.81	0.00
7	CFP	1	0.90	41.18	33.87	23.81	1.14
8	CFP	3	0.90	38.90	33.87	23.81	3.43
9	CFP	5	0.98	36.61	33.87	23.81	5.71
10	CFP	9	1.06	30.90	33.87	23.81	11.43
11	CFP	4	1.04	36.03	33.33	25.01	5.62
12	CFP	5	1.17	37.13	34.35	22.72	5.80
13	CFP	4	1.14	41.90	28.57	23.81	5.71
14	CFP	5	1.11	32.38	38.10	23.81	5.71
15	CFP	5	1.08	28.91	41.56	23.81	5.71
16	GP	1	0.90	41.18	33.87	23.81	1.14
17	GP	3	0.90	38.90	33.87	23.81	3.43
18	GP	5	0.90	36.61	33.87	23.81	5.71
19	GP	9	1.14	30.90	33.87	23.81	11.43
20	GP	5	0.95	36.03	33.33	25.01	5.62
21	GP	5	1.00	37.13	34.35	22.72	5.80
22	GP	4	1.16	41.90	28.57	23.81	5.71
23	GP	5	0.90	32.38	38.10	23.81	5.71
24	GP	5	1.08	28.91	41.56	23.81	5.71

Table 6.3: Table of mixes tested in terms of weight percentage of dry material.

Note that WPCM is a percentage of the overall material mass including water, so differs from the weight percentage of dry material for each CBM.

7 | Results of further analysis of the conductive mortars

This chapter describes and discusses the results of further analysis that was performed on the conductive mortar cubes manufactured for Chapter 6. This analysis used the same data, and the methods, materials and equipment described in Sections 4.2.2, 4.4 and 6.3 apply here. Methods specific to this analysis are described by Section 4.5. Mix numbering is also carried over from Chapter 6; see Table 6.1 or 6.3.

The intent of this analysis was to develop a better understanding of the relative effects of the different parameters of the mix design on the mortar resistivity, as well as any differences between the Carbon Fibre Powder (CFP) and Graphite Powder (GP) additions, following the analysis in Chapter 6. Those results indicated that Weight Percentage of Carbonaceous Materials (WPCM) was the most important of the factors examined, followed by W/c and then G/s.

Measurements of particle length, diameter and electrical conductivity of the CFP and GP would have been useful in applying theoretical models to the mortar electrical properties. However, because modelling was not a priority and every effort was being made to reduce the risks from working with the carbonaceous powders, these quantities were not directly measured and performing more physical experiments was outside the scope of this work. Due to differences in manufacturing processes between vendors, this information could not be reliably sourced from the literature. The area in which measurements of these quantities would have been useful are discussed in Section 7.2.2.

7.1 Results

Some material from Section 4.5.1 is reproduced here for the reader's convenience. As in Chapter 6, measurements above 10MHz were discarded because of issues with the probes that were used to take the measurements.

7.1.1 Equivalent circuit modelling

The equivalent circuit used is reproduced here in Fig. 7-1.

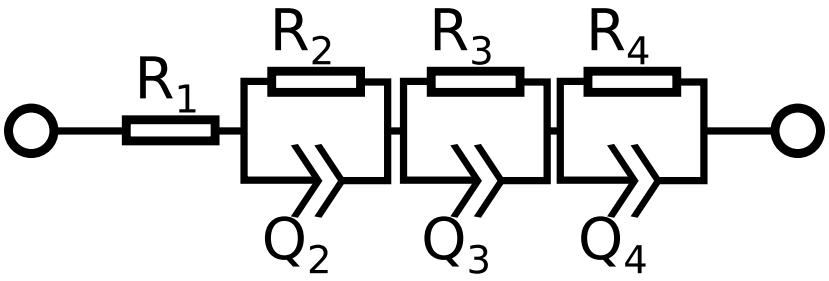

Figure 7-1: Diagram of the equivalent circuit, after L. Zhang et al. (2017).

The explanation of the physical meaning of the components from L. Zhang et al. (2017) states that R_1 represents the resistance of the fluid solution in the pores (this assumes a saturated mortar, which the cubes were when measured), R_2Q_2 represents the effects of the cement matrix excluding the additions, R_3Q_3 represents the effects of the electrodes, and R_4Q_4 represents the effects of the cement matrix in series with the additions.

7.1.2 Equivalent circuit component values

Table. 7.1 gives equivalent circuit parameters for each mix at 35 days hydration. This information is also available (although not in this collected format) in the online data repository for the publication that it was collected for; see Section 6.5.

Measured and fitted impedance spectra

Fig.7-2 gives some comparisons of measured and fitted impedance spectra. 35 day measured spectra are plotted along with their fitted spectra. For the sake of

	Mix	R_1 Ω	R_2 Ω	Q_2	Q_2(p)	R_3 Ω	Q_3	Q_3(p)	R_4 Ω	Q_4	Q_4(p)	Iterations
Non-CBM	1	44.60	37688.00	$3.67 \cdot 10^{-5}$	0.51	953.56	$5.73 \cdot 10^{-10}$	0.80	1760.20	$4.84 \cdot 10^{-9}$	0.75	1000
	2	$1.68 \cdot 10^{-12}$	1051.40	$1.58 \cdot 10^{-9}$	0.74	15477.00	$4.22 \cdot 10^{-5}$	0.63	952.79	$8.10 \cdot 10^{-9}$	0.73	1000
	3	132.16	20214.00	$1.29 \cdot 10^{-5}$	0.69	365.44	$2.90 \cdot 10^{-11}$	1.00	1272.90	$1.03 \cdot 10^{-8}$	0.68	1000
	4	$2.82 \cdot 10^{-12}$	1511.20	$2.78 \cdot 10^{-9}$	0.71	2062.90	$3.48 \cdot 10^{-5}$	0.53	23511.00	$5.70 \cdot 10^{-6}$	1.00	1000
	5	65.65	44705.00	$2.17 \cdot 10^{-5}$	0.60	1433.60	$1.75 \cdot 10^{-9}$	0.75	189.00	$7.27 \cdot 10^{-8}$	0.69	1000
	6	21.82	1473.30	$1.82 \cdot 10^{-9}$	0.73	473.02	$1.77 \cdot 10^{-5}$	0.63	$1.69 \cdot 10^{5}$	$1.27 \cdot 10^{-5}$	0.76	1000
CFP	7	26.09	626.33	$3.37 \cdot 10^{-9}$	0.73	901.93	$7.31 \cdot 10^{-6}$	0.52	27503.00	$1.51 \cdot 10^{-5}$	0.80	2900
	8	21.44	1216.30	$6.08 \cdot 10^{-6}$	0.54	403.75	$3.53 \cdot 10^{-8}$	0.62	63792.00	$2.59 \cdot 10^{-5}$	0.71	1000
	9	82.68	0.31	$1.84 \cdot 10^{-5}$	0.00	13.24	$3.73 \cdot 10^{-9}$	1.00	4937.50	$9.21 \cdot 10^{-5}$	0.34	3000
	10	47.22	5.59	$2.43 \cdot 10^{-7}$	1.00	237.25	$2.19 \cdot 10^{-4}$	0.50	407.07	$7.05 \cdot 10^{-6}$	0.64	1000
	11	119.78	661.79	$8.21 \cdot 10^{-6}$	0.54	29.66	$2.26 \cdot 10^{-9}$	0.99	62081.00	$8.68 \cdot 10^{-5}$	0.66	1000
	12	96.78	398.78	$4.09 \cdot 10^{-6}$	0.65	36.13	$3.95 \cdot 10^{-9}$	0.96	4784.10	$1.51 \cdot 10^{-4}$	0.43	3000
	13	77.20	119.67	$3.08 \cdot 10^{-7}$	1.00	23.51	$1.93 \cdot 10^{-8}$	0.87	10947.00	$1.71 \cdot 10^{-4}$	0.31	3000
	14	66.28	715.49	$5.81 \cdot 10^{-6}$	0.59	$1.00 \cdot 10^{6}$	$2.72 \cdot 10^{-5}$	0.63	105.34	$6.88 \cdot 10^{-7}$	0.56	3000
	15	95.97	29.25	$1.69 \cdot 10^{-8}$	0.89	648.76	$7.31 \cdot 10^{-6}$	0.56	1175.00	$4.19 \cdot 10^{-5}$	0.66	3000
GP	16	6.63	$9.69 \cdot 10^{5}$	$4.13 \cdot 10^{-5}$	0.71	532.33	$1.08 \cdot 10^{-9}$	0.79	570.99	$3.05 \cdot 10^{-5}$	0.30	3000
	17	22.70	42127.00	$1.17 \cdot 10^{-5}$	0.80	322.74	$1.64 \cdot 10^{-8}$	0.69	1266.10	$2.70 \cdot 10^{-5}$	0.33	1200
	18	53.58	1699.10	$1.10 \cdot 10^{-4}$	0.26	62.49	$6.86 \cdot 10^{-7}$	0.62	$9.74 \cdot 10^{5}$	$3.66 \cdot 10^{-5}$	0.68	1000
	19	55.46	68.16	$2.48 \cdot 10^{-6}$	0.70	23.22	$9.85 \cdot 10^{-9}$	1.00	396.09	$5.81 \cdot 10^{-5}$	0.54	1000
	20	0.03	$5.16 \cdot 10^{5}$	$2.20 \cdot 10^{-5}$	0.73	350.23	$1.25 \cdot 10^{-6}$	0.46	1410.10	$2.38 \cdot 10^{-5}$	0.38	1300
	21	37.18	1123.70	$3.66 \cdot 10^{-5}$	0.34	158.57	$1.78 \cdot 10^{-6}$	0.47	44025.00	$2.37 \cdot 10^{-5}$	0.77	1000
	22	$7.62 \cdot 10^{-13}$	45.52	$5.18 \cdot 10^{-8}$	0.63	1380.60	$7.40 \cdot 10^{-5}$	0.25	33633.00	$2.62 \cdot 10^{-5}$	0.83	1000
	23	0.12	421.20	$1.01 \cdot 10^{-7}$	0.59	1437.10	$1.09 \cdot 10^{-5}$	0.38	67015.00	$3.26 \cdot 10^{-5}$	0.54	3000
	24	$1.96 \cdot 10^{-13}$	2113.00	$4.41 \cdot 10^{-5}$	0.27	$1.23 \cdot 10^{5}$	$1.15 \cdot 10^{-5}$	0.78	61.95	$1.19 \cdot 10^{-9}$	0.99	3000

Table 7.1: Equivalent circuit parameters for all mixes at 35 days hydration.

space, only six mixes are presented here. These results are representative of the quality of fit that was obtained for the other mixes.

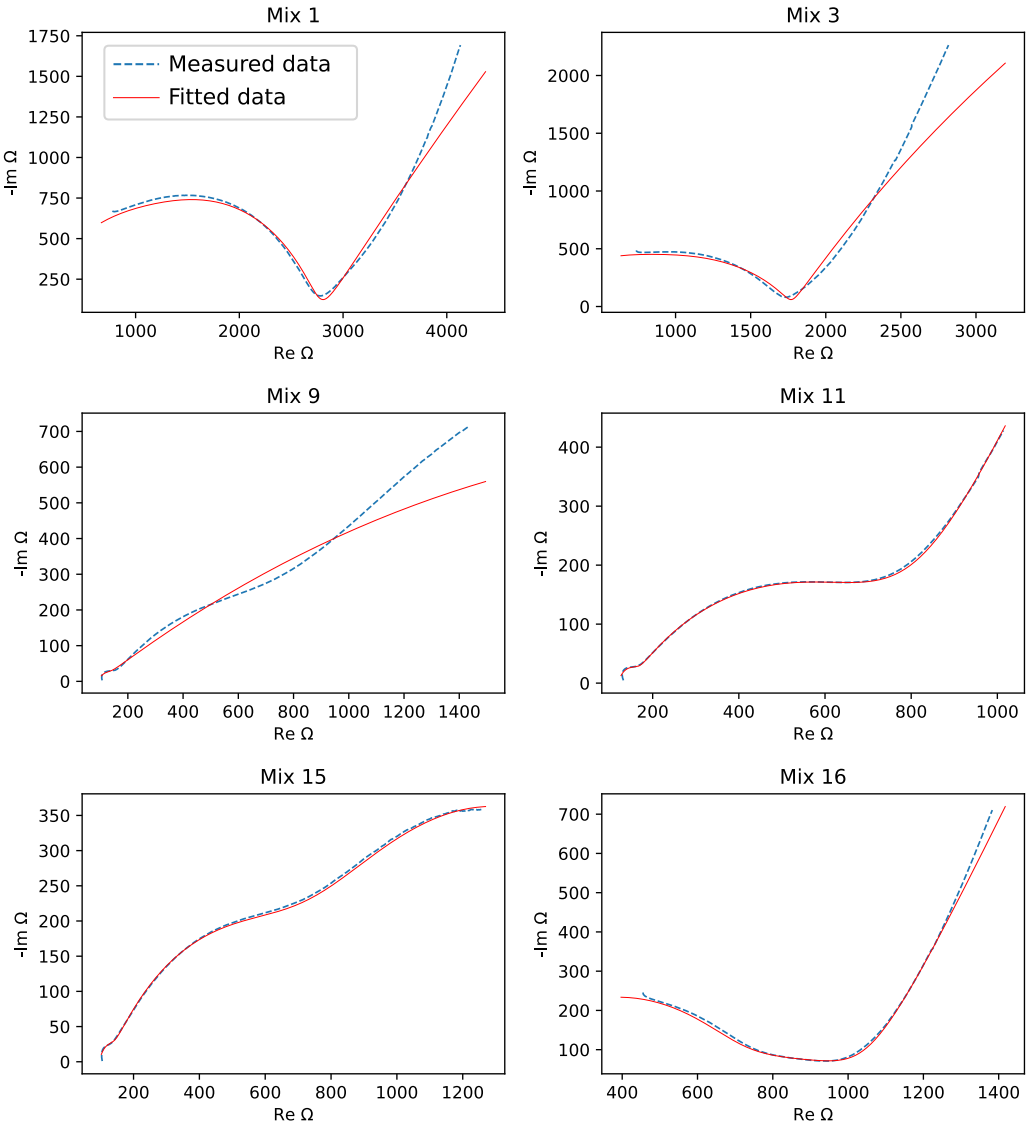

Figure 7-2: Measured and fitted impedance spectra for selected mortar mixes.

7.1.3 Theoretical and measured conductivity values

Measured conductivities for the conductive mortar mixes were compared to theoretical values. Mixes with varying quantities of CFP were used for this. The relevant methods are given by Section 4.5.2.

For clarity, a summary of variables and their uses is given here:
σ_e is the bulk conductivity of the mix, and is obtained from Nyquist plots or predicted using Eqs. 3.1 and 3.5.
σ_m is the matrix conductivity, obtained from the control mix.
σ_a is the conductivity of the conductive addition. This was found from literature for CFP as $6{\cdot}10^4$S/m Wypych (2016, pp. 252-255). ϕ is the volume percentage (also called volume fraction) of conductive additions in a mix.
f_c is the "cusp frequency" at which the Nyquist plot for a mix transitions from one arc to another.
A is the aspect ratio of the particles of a conductive addition.

Several conductivity values had to be determined by inspection of Nyquist plots, by looking for the transition between arcs and determining σ at this point. Table 7.2 gives these values.

Mix 3 f_c = 25kHz σ_m = 0.017 S/m Used as σ_m in all calculations.

	Mix	ϕ%	f_c	σ_e S/m	
CFP	7	1.1	320kHz	0.045	Used to calculate A.
	8	3.3	530kHz	0.068	
	9	5.3	740kHz	0.199	
	10	10.0	5MHz	0.653	

Table 7.2: Values obtained by inspection of Nyquist plots.

The value of σ_e for mix 7 was used in Eqs. 3.1 and 3.5 to solve for A in the randomly oriented additions cases, which led to $A = 30.2$.

This A value was substituted back into Eqs. 3.1 and 3.5, to predict σ_e. Fig. 7-3 shows the measured and predicted values of σ_e against ϕ for both the random and non-randomly oriented cases.

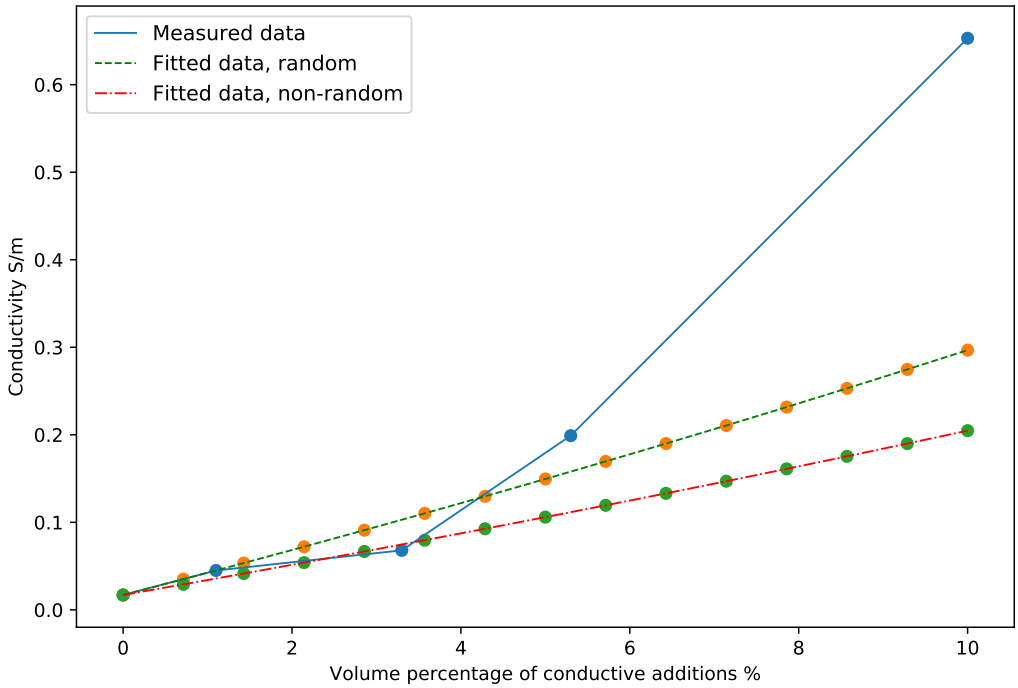

Figure 7-3: Measured and simulated σ_e against ϕ.

7.1.4 Percolation

Analysis was performed to determine whether or not the conductive inclusions had achieved percolation. The concept of percolation as it applies to cementitious materials containing conductive additions is described in Section 3.2.3, and methods for this analysis are described by Section 4.5.3.

Graphs of conductivity vs. volume percentage of conductive additions for CFP and GP by Figs. 7-4 and 7-5 respectively.

Attempts to fit Eq. 3.7 to the data and hence determine $\phi_{c,e}$ and n_e were made, but produced physically unrealistic results and as such are not presented.

7.2 Discussion

Results presented in this chapter represent three fairly distinct lines of inquiry into the mortar behaviour, intended to supplement the work presented in Chapter 6. The three areas are discussed here separately, followed by a note about the data.

7.2.1 Equivalent circuit analysis

The model from L. Zhang et al. (2017) was used because it was the only applicable model found in the literature that fit the measured data using the Powell algorithm in the EISAnalyzer software to a reasonable level of accuracy for all mixes.

The model consists of a single resistor in series with three parallel resistor/Constant Phase Element (CPE) blocks. A resistor and CPE in parallel can be used to model arcs in a Nyquist plot while accounting for errors between theoretical and actual systems. Three of these blocks in series simulates up to three separate arcs in the Nyquist plot, and fits well with spectra where three distinct arcs are apparent, such as in mixes 11 and 15.

Although the model fits the data well, it appears from the calculated component values that the physical interpretation of the model given by L. Zhang et al. is not applicable to the mortars used to obtain the measured data. For example it would be expected that R_3Q_3, representing the electrodes, would be expected to vary relatively little across the mixes. However as can be seen from Table 7.1, while R_3 values are often on the order of 10^1 ohms, several are much higher with the highest being over 1 MΩ. Similarly the Q_3 values range from the order of 10^{-11} to 10^{-4}, with CPE exponent values from 0.5 to 1.0. R_1, pore solution resistance, is more reasonable, but still varies by three orders of magnitude. For R_4Q_4, which models the conductive additions and their interactions with the cement matrix, it would be expected that impedance would reduce with increasing WPCM as seen in Chapter 6.

However, R_4 in mixes 7, 8 and 18, with WPCM 1%, 3% and 5% respectively, are all higher than that of mix 3, the control. By finding the impedance of the CPE using $X_{CPE} = Q(j\omega)^{-p}$ (Woo et al., 2003) at an arbitrarily chosen 10kHz and treating the R_4Q_4 as a parallel RC circuit, its impedance magnitude can be calculated by $(RX_{CPE})/(\sqrt{R^2 + X_{CPE}^2})$ (Floyd, 2010), resulting in 1.55Ω, 2.82Ω, 112.69Ω and 26.28Ω in CFP mixes with WPCM 1%, 3%, 5% and 9% respectively. Based on the trends observed in Chapter 6, the part of the model representing the conductive additions would be expected to trend downwards in impedance with higher WPCM.

Computing the impedance of each RQ block and summing them along with

R_1 does result in the expected trend, but this is not useful for trying to separate the effects of different mix factors on impedance.

Since no other model that could be found in the literature fit the measured data, it is likely that a new model would be required to both fit the data and provide a good physical interpretation for the calculated values. This would likely require examination of the experimental setup; scanning electron microscopy on some of the mortars might also be helpful. Alternatively it is possible that different software would be able to fit an existing model, if another software package were available.

7.2.2 Theoretical and measured conductivity values

The graph shown by Fig. 7-3 represents the best fit of the effective medium theory based approximation for the data. In the absence of measured physical data on the conductive particles, calculating A using another data point was the only option available, but because of the way the equation works this will always result in a line simply being drawn between the $\phi = 0\%$ data point and the point used to calculate A. Using the $\phi = 10.0\%$ data point to perform the calculation gives an A of 46.5, which may therefore be a more reasonable value as this line would fit the data somewhat better.

The randomly oriented model fits the data better when A is found assuming random orientation, having a steeper gradient than the non-randomly oriented model. When A is found assuming non-random orientation, the same is true; the randomly oriented model is steeper, the only difference being that whichever model is used to calculate A has its line pass through both the $\phi = 0\%$ and 1.1% measured data points. The difference suggests that the particles are entirely or almost entirely randomly oriented in all planes.

A larger issue than the lack of a directly measured A is that the model assumes a linear fit, which is not present in any of the data - see Figs. 7-4 and 7-5. This also affected the observations related to percolation, and possible explanations for this are discussed in Section 7.2.3.

7.2.3 Percolation

In the context of this work, percolation of the CFP and GP additions within their respective mortars would cause a reduction in the rate of change of conductivity with respect to the increasing quantity of the additions. If percolation were achieved, it would be reflected in a flattening of the lines in Figs. 7-4 and 7-5 - a reduction in the rate of change of σ with respect to ϕ. Increasing the quantity of these additions has been found to lead to difficulties with workability and the materials are expensive relative to the other components of cementitious materials, so this point of diminishing returns is of great interest when using the additions.

From examining Figs. 7-4 and 7-5 it does not appear that percolation has been achieved by the 5% volume percentage mark in either case. Neither CFP or GP appears closer to achieving percolation than the other.

It is possible that percolation has been achieved at 10% with a percolation threshold between 5% and 10%, but in neither material case is the gradient between the 5% and 10% values substantially different to that between the 3% and 5% values. This suggests that if the percolation threshold is lower than 10%, it is very close to 10%. More data points between 5% and 10% would allow some more confidence, but ultimately in the absence of data showing the characteristic flattening of the conductivity lines it is only possible to conclude that percolation has not been achieved by 5% volume percentage. It should be noted that this would likely require significant measures to improve mixing and workability of the mortar mix. It should also be considered that Huang et al. (2016) was able to achieve higher percentages (it is not specified if they have been calculated by weight or by volume) of graphite powder in mortar mixes, and from the data they present a percolation threshold of between 10% and 15% seems likely.

Mix 10, the ϕ = 10% CFP mix, exhibits some unexpected behaviour at 10MHz, with its conductivity decreasing below the 1MHz value. Inspection of the data reveals that this is probably the result of the issues with data capture at higher frequencies that were encountered with the probes used (as mentioned in Section 4.4.3) with conductivity increasing as is generally expected until 5MHz, at which point the behaviour becomes unpredictable. The unreliability of high frequencies measurements with the probes was generally consistent in other cases,

and it is unknown what has caused the problems at a comparatively low frequency. Note that this issue does not affect any of the analysis in Chapter 6.

Attempts to fit the data to the theory, and thus predict the ϕ at which percolation would be achieved, were not successful. In both the CFP and GP cases the few data points available behave non-linearly, and it is not known if they are anywhere near the percolation threshold. Determining the actual percolation threshold would be best done with data on mixes that have undoubtedly achieved percolation.

Non-linearity in the data

The non-linear behaviour in both Figs. 7-4 and 7-5 is unexpected. In the CFP case the $\phi = 5.3\%$ and 10% mix required extra water to mix properly, which probably accounts for the jump in conductivity between $\phi = 3.3\%$. For GP this was necessary for the $\phi = 9.3\%$ mix, but not before, accounting for the increase in gradient between mixes 18 and 19. Otherwise, the reasons for the non-linearity are unclear. The most unexpected result is probably the decrease in conductivity between GP mixes 16 and 17, $\phi = 1.0\%$ and 3.1% respectively. It may be the result of slightly different clamping force on the electrodes compared to others when the measurements were taken.

7.3 Conclusions

From the data that was produced for this work, little can be concluded about the actual percolation threshold of the conductive additions. Certainly percolation has not been achieved by 5% volume of either addition. It is possible that it has been achieved by 10%. Without more data it is impossible to say more, but the observations are consistent with another case in the literature. Predicting the conductivity of the mortars using the effective medium theory approach was largely unsuccessful due to non-linearity of the data, but the results did suggest that the fibres in both cases are randomly or very close to randomly aligned. Measured data was fitted to an equivalent circuit from the literature, but no meaningful physical interpretation of the modelled values could be made.

When the experiment in Chapter 6 was performed, it was as a purely experimental investigation into mortar conductivity. Because of safety issues associated

with working with CFP and GP, data not directly useful to the study as it was originally conceived was not collected, some of which would have been useful for this modelling work.

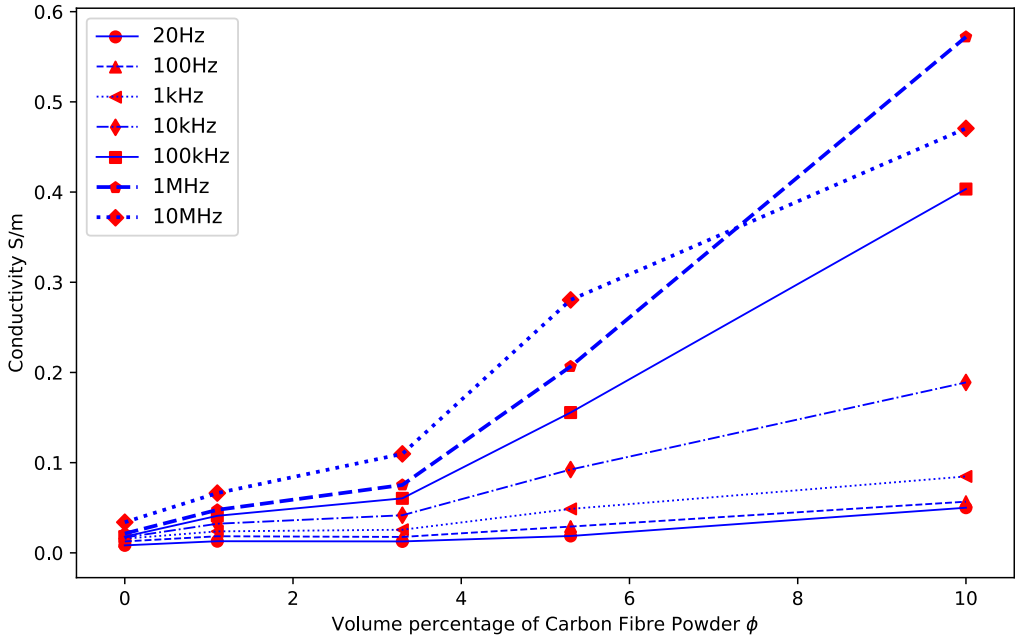

Figure 7-4: Conductivity vs. volume percentage of CFP additions at 35 days hydration. This graph shows varying ϕ on the X axis, using data from mixes 3, 7, 8, 9 and 10. Lines show conductivity for the same measurement frequency.

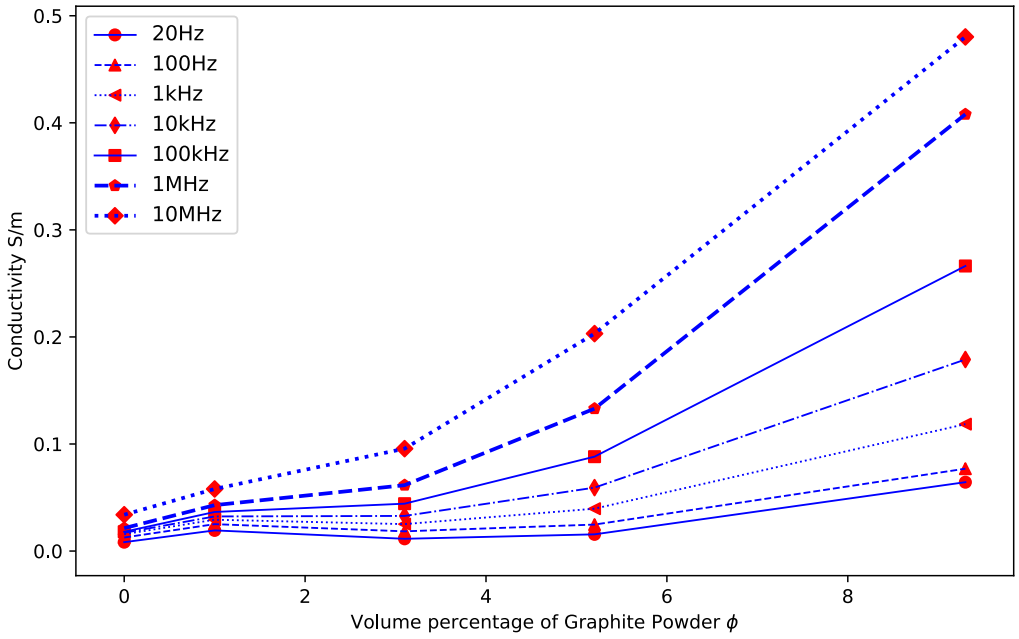

Figure 7-5: Conductivity vs. volume percentage of GP additions at 35 days hydration. This graph shows varying ϕ on the X axis, using data from mixes 3, 16, 17, 18 and 19. Lines show conductivity for the same measurement frequency.

8 | "EIT imaging of conductive mortars"

The final objective of the project was the Electrical Impedance Tomography (EIT) imaging of conductive mortars.

Based on the results of the mortar resistivity study a mortar mix was chosen for testing of imaging of conductive mortar cylinders - "Mix 20" from Chapter 6. This mix was chosen since it would provide substantially reduced resistivity as well as significant frequency dependence to resistivity over the frequencies available to the study. One of the less resistive mixes was not selected for a number of reasons. Firstly these would have been difficult to manufacture in quantity due to the adverse effect that the powders used had on workability. Secondly using an increased quantity of powder would have brought much greater cost and difficulty in maintaining lab safety. Imaging was carried out on the cylinders using the Kyung-Hee University Mark 2.5 EIT machine (KHU Mk 2.5) EIT machine. This built on the earlier work carried out on the dental plaster and concrete cylinders. In spite of the decreased resistivity, imaging remains difficult. This work fulfilled objective three of the project.

Special attention is paid in the paper to describing the different electrode configurations since this is important for practical purposes. In addition, a method of combining image reconstructions was proposed to reduce the dependence of the image reconstruction quality on abstract parameters defined by the operator was proposed and tested.

Not presented in the paper are attempts that were made at Frequency Difference Electrical Impedance Tomography (FDEIT) using the data. This was done because of the success encountered using this method on dental plaster in Section 5.1 This mortar mix had been determined in Chapter 6 to exhibit dif-

ferent resistivity across the frequencies used, to a level that should have been resolvable by the KHU Mk 2.5. FDEIT between 1kHz and 5kHz were attempted using Tikhonov regularisation (TK-R). These image reconstructions were not useful, and the fact that the Time Difference Electrical Impedance Tomography (TDEIT) images using the 5kHz data were also not useful suggests some issues with the data that was collected, as described in Section 8.3.1.

This paper has some slight changes from the submitted version. References have been changed from a numbered style to be consistent with the rest of the thesis. The bibliography has been integrated with that of the thesis. The methods from this paper are reproduced in Section 4.6.

This declaration concerns the article entitled:									
EIT imaging of conductive mortars									
Publication status (tick one)									
Draft manuscript	✓	**Submitted**		**In review**		**Accepted**		**Published**	
Publication details (reference)									
Candidate's contribution to the paper (detailed, and also given as a percentage).	The candidate contributed to/ considerably contributed to/predominantly executed the... Formulation of ideas: The concept of this paper was developed from K. Paine (25%) and M. Soleimani's (25%) original project proposal by S. Davey (50%) following the final direction of the project. Design of methodology: The basic experimental methods associated with EIT and some advice on the image reconstruction process was provided by M. Soleimani (30%). The configurations of the cylinders and the actual experimental methods used were designed by S. Davey (70%) based in part on information from the literature which has been referenced where appropriate. Experimental work: All experimental work carried out by S. Davey (100%). Presentation of data in journal format: Data analysis and writing performed by S. Davey (80%) with advice from M. Soleimani (10%) and K. Paine (10%).								
Statement from candidate	This paper reports on original research I conducted during the period of my Higher Degree by Research candidature.								
Signed					**Date**				

Abstract

The purpose of this work was to explore practical issues related to the use of Electrical Impedance Tomography (EIT) for in-situ structural health monitoring of buildings.
EIT was applied to conductive mortar cylinders to attempt to detect resistive air void inclusions. Different electrode types and sample preparations were compared, and imaging results were compared to simulated reconstructions. Image reconstruction was done using the common Tikhonov Regularisation (TK-R) method and used the open-source EIDORS Matlab library. A simple method for combining the results of these reconstructions was also applied.
Good image reconstructions of an inclusion relatively close to the cylinder surface was achieved with TK-R. Other inclusions were not properly distinguished using TK-R. Electrode type and sample preparation was found to be very important in obtaining good results using low voltage EIT equipment, in spite of the use of conductive mortar. The method for combining images was found to improve results in two out of three cylinders.
This work will be of use for anyone considering the practical aspects of implementing EIT for structural health monitoring in an industrial context.

Keywords

Non-destructive testing; Electrical impedance tomography; Conductive mortar; Mortar crack

8.1 Introduction

Deterioration in reinforced concrete compromises the strength and durability of infrastructure worldwide. Most problems arise due to the ingress of CO_2 or chloride ions that negatively affect the passive oxide layer that protects the steel reinforcement. Others are caused by the ingress of ions, such as sulphates, that attack the hardened cement paste (Dyer, 2014, p. 431). The resistance of concrete to deterioration can be enhanced by the use of appropriate cements and additions, suitable mix designs, and effective site practice (Dhir et al., 2004; McCarthy et al.,

2001). However some degree of cracking of concrete is inevitable and cracks within concrete provide a route for rapid ingress of harmful ions and compounds that prevails over all efforts to provide appropriate concrete specification. To this end the observation and knowledge of the depth and interconnectivity of cracks in concrete is an important consideration in the structural health monitoring of concrete (Afzal et al., 2012; Zhang, B. et al., 2010).

Furthermore, due to concerns with cracks, there has been considerable recent interest in the development of self-healing concretes that seal cracks soon after they develop (De Belie et al., 2018). In most techniques crack healing is most effective at the surface where water, and sometimes oxygen, are most readily available to initiate crack closure. This often means that visual inspection of self-healing concretes will show an uncracked and apparently unspoiled concrete surface. However, only a few millimetres below the surface the crack may still exist and consequently the resistance of the concrete to harmful ions and compounds is little improved. A method to assess and monitor the presence of cracks within the concrete is therefore required.

Electrical Impedance Tomography (EIT) is a non-destructive test technique belonging to the family of Electrical Property Imaging (EPI) methods. EPI produces images from the distribution of a particular electrical property within a body or medium, with changes in that property showing some kind of material discontinuity. Within this family of methods EIT is used for reconstructing conductivity by measuring potential differences across paths in a body, Electrical Capacitance Tomography (ECT) reconstructs permittivity by measuring capacitance across paths in a body (Yang, W. Q. and Peng, 2003), and Magnetic Induction Tomography (MIT) reconstructs conductivity by inducing and measuring eddy currents in a body (Ma and Soleimani, 2017). ECT and MIT have been used mostly for industrial process monitoring. Both modalities can be used without making physical contact with the body, which can be advantageous in that field. For imaging of near-surface cracks in concrete, physical access to the surface is not likely to pose a problem in general. ECT imaging is highly sensitive to electrical interference and MIT is best used for distinguishing metallic and non-metallic regions. For this reason work on the application of EPI to concrete has mostly focussed on EIT. Image reconstruction in all cases is based on the same mathematics, so developments made in one area may be applicable to

others.

Electrical conductivity of concrete is strongly influenced by liquid water content, as well as other parameters of the mix (McCarter, 1994). In general dry and fully hydrated concrete will typically have a DC conductivity on the order 10^{-6} S/m (Hornbostel et al., 2013). In contrast the conductivity of air is 10^{-14} S/m depending on temperature and humidity, and the conductivity of steel is 10^{7} or 10^{8} S/m also depending on temperature. A properly reconstructed conductivity distribution could therefore be used to distinguish reinforcement and voids filled with air from the concrete matrix, providing a crack identification and characterisation capability.

The EIT process involves injecting currents and measuring voltages on the boundary of the medium to be measured. The inverse problem of inferring a conductivity distribution from these boundary measurements is severely ill-posed (Holder, 2004) which limits the achievable accuracy of the reconstructed images. EIT was originally developed for medical imaging (Barber et al., 1983) in which resistive regions represented bone. While the spatial resolution of EIT is relatively coarse compared to X-Ray based methods or MRI, it can be used for much lower cost and has no health risks associated with repeated applications. It has therefore been positioned as a low cost method for monitoring patients, as a complement to higher resolution imaging methods. Significant progress has since been made in development of hardware and the image reconstruction process, leading to studies of EIT in such applications such as stroke detection (Zhou et al., 2015) and breast cancer imaging (Murphy et al., 2017). The terms EIT and Electrical Resistivity Tomography (ERT) are often used interchangeably in the literature. EIT may include the reconstruction of real and complex resistivity, whereas ERT refers exclusively to the real part of the resistivity. Here both terms are used to be consistent with the work being described.

ERT has been used for some geophysics applications. Martínez-Moreno et al. (2018) used a combination of ERT and induced polarisation methods to identify features correlated to the presence of water intrusion and erosion by creating a resistivity profile of the surrounding area. In the structural field, EIT and related technologies have been established as feasible for use on concrete. Hou, T. C. and Lynch (2008) applied EIT to beams made of a strain hardening fibre reinforced cementitious composite material during various mechanical tests to image cracks

and internal strain fields. The results show some changes to the conductivity map as a result of strain, and clear locations of large surface cracks resulting from specimen failure. Karhunen et al. (2010a) showed the detection of resistive and conductive (relative to the concrete body) inclusions in saturated early hydration concrete using an ERT device built for industrial process tomography. Hallaji and Pour-Ghaz (2014) did not image concrete directly, instead applying a conductive skin to the surface of a concrete beam while cracks were produced by loading. This allows the localisation of surface cracks without being sensitive to the electrical properties of the concrete itself. Detection and localisation of these cracks by ERT is good, but this system does require at least some prior knowledge of where cracks are likely to form, and does not distinguish between damage to the concrete and damage to the sensing skin. Reichling et al. (2014) used an array of electrodes mounted in a single line on a single side of a beam to examine conductivity distribution within the concrete in order to locate a reinforcement bar, and were able to achieve good imaging of the high-contrast feature. Several investigators have attempted to use EIT/ERT to measure water saturation in concrete, due to its relation to durability. Hallaji et al. (2015) used ERT to monitor moisture ingress in a block of cement paste material. The progress of moisture through the block was also tracked visually and with neutron radiography imaging for comparison. The resistivity reconstructions in this case compare well to the other methods used to track the moisture. Smyl et al. (2016) continued the work detailed in Hallaji et al. (2015), investigating EIT for 3D monitoring of moisture ingress, comparing the results to simulations of moisture ingress and X-Ray CT imaging. The EIT imaging results agreed reasonably well with the simulations, better than the X-Ray CT images. Suryanto et al. (2017b) cast electrodes into a concrete cylinder to perform ERT during water ingress. The system used was able to show water movement consistent with expectations based on some the presence of some damage in the cast concrete. Capozzoli and Rizzo (2017) combined ground penetrating radar with ERT measurements taken using geophysics resistance measurement equipment in a single-sided planar array configuration. This system was used to locate pipes made from conductive and non-conductive materials and damage in a simulated road segment. While the ERT was not able to resolve at the same depth as the ground penetrating radar, it was able to distinguish different layers of material at depths of up to

24cm. In this case the ERT electrodes were applied to concrete after an attempt to apply them to an asphalt layer was unsuccessful due to the high resistance of the asphalt.

Recently there has been some interest in smart structures and materials, which are constructed with features to facilitate health monitoring. Concretes with increased electrical conductivity have been studied for various forms of self-sensing including strain monitoring (Chen et al., 2017) and correlation of electrical resistance with damage (Ding et al., 2015). B.S. Huang et al. (2016) performed ERT imaging on four cylinders of identical cross-section and different levels of graphite content, and found that increasing conductivity had a positive effect on the quality of image reconstructions. Conductive concrete has also been examined for other purposes including electromagnetic shielding (Ogunsola et al., 2009) and self-heating concrete for de-icing (Yuan, Y.Q. et al., 2011). This presents an opportunity for using lower-voltage EIT equipment for NDT on mortars and concrete. Smart structures using conventional materials have also been investigated. For example Niederleithinger et al. (2015) has investigated using ultrasound sensors embedded in concrete for the detection and monitoring of the hydration process and damage. EIT has the potential to be applied in a similar way, with electrodes embedded in concrete. This would allow for constant monitoring, or damage scans on demand, although care would have to be taken to ensure that the damage would not also degrade the performance of the system.

In cases where a large number of concrete elements are to be tested it may be more economical to spend the money on this high voltage equipment and take the necessary safety precautions when using it. However, for applications where a smaller number of elements are to be assessed, it may make sense to design these elements to be friendlier to NDT at some added expense and use cheaper equipment to carry out testing.

This paper presents EIT images produced with three cylinders made of a mortar that has been altered to increase its conductivity - by addition of conductive materials to the mortar mix, and by saturation with liquid water - in order to facilitate EIT imaging using low-voltage equipment.

8.2 Materials and methods

8.2.1 EIT equipment

Impedance readings were taken using a KHU mark 2.5 EIT machine described by Wi et al. (2014) and using the standard control software provided with the machine. The KHU mark 2.5 is a PC-based system, consisting of an analogue measurement module, a digital control and network module, and the power supply.

The KHU series of EIT devices has been developed from the perspective of medical imaging rather than structural health monitoring or industrial process imaging. This requires that the current source be limited to low amperage for reasons of patient safety.

8.2.2 Conductive mortar cylinders

The mortar used a Portland fly ash cement, CEMII/B-V 32.5N. Fine aggregates used were an alluvial sand (s) and Marlborough grit (g), both conforming to BS EN 12620. The g/s ratio used was 0.8. The mortar's electrical resistivity was reduced by the addition of Graphite Powder (GP) such that the Weight Percentage of Carbonaceous Material (WPCM) was 5%. According to the manufacturer, the GP particles were sized such that 85% passed a 0.044mm sieve. Particle density was roughly 1900 kg/m^3. GP was used to represent fine sand for the purposes of calculating g/s. The composition of the conductive mix was based on earlier experiments into mortar conductivity and had a w/c ratio of 0.95, GP/c ratio of 0.22 and an overall aggregate (s+g+GP) to cement ratio of 2.77. It was not intended to closely represent a mix that might be used in a structural application.

The choice of mixing method was guided by the need to minimise the safety risks that carbon powders pose to humans and electrical equipment. GP was mixed by hand with fine aggregates and cement powder, and water added afterwards. Moulds were made by cutting plastic pipes in half lengthways and reassembling them with tape. The water content of the mortar was unusually high since it was found that this was necessary to ensure that the components mixed properly with the water in the presence of the GP.

Three cylinders were investigated. These were of approximately 120mm height

and 65mm nominal diameter. Each had a different defect created during casting using wooden inclusions, with the wood removed to produce air-filled voids. The inclusions were aligned with the long cylinder axis as far as possible, so that cross section was constant for 80% of the cylinder height. The diameter of all cylinders was 65mm. Cross sections of each cylinder are given by Fig. 8-1.

After moulding, the cylinders were stored at 20°C and 40% RH for 24 hours. They were then demoulded after 24 hours and kept in 20°C water for around six months before being allowed to air dry for the first set of tests. A more comprehensive drying protocol was not used since natural air drying better represents the actual conditions under which EIT might be used for structural health monitoring.

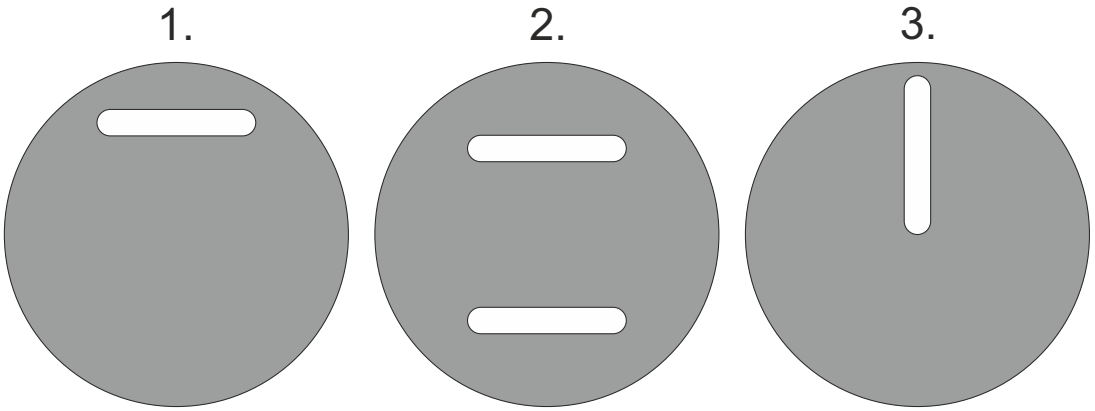

Figure 8-1: Diagrams of all mortar cylinders.

Testing of this conductive mortar versus a conventional mortar of the same mix parameters showed a reduction of real resistivity magnitude of over 50% at the frequencies used in this study. The real resistivity of the mortar at 1 kHz (at which the most useful imaging results were obtained) was 37 Ω·m.

8.2.3 Interfacing the cylinders and EIT equipment

Preliminary work found that the results of imaging attempts were very sensitive to the approach to connecting the EIT hardware and the mortar cylinders. Three measurement configurations were tested.

The first approach (method A) was to use electrodes consisting of sponges soaked in a conductive electrode gel. The small size of the mortar cylinders

prevented the use of readily available commercial gel electrodes. To produce electrodes of the necessary size sponges were soaked with a medical electrode gel and located using 3D printed jigs. Copper tape was used as an intermediary between the sponge and the clips from the connection cables of the EIT system. The sponges were left attached to the mortar surface for four hours between the initial application and the measurements being taken to allow the gel to penetrate the mortar to some degree and reduce overall impedance across electrodes. *A photograph of one of the sets of sponge electrodes is given by Fig. 4-2.*

In method B electrodes consisted of colloidal silver paint applied to the surface of the mortar, similarly to Hallaji et al. (2015). The connection to the EIT system was made by securing one end of a short length of multi-core wire to the painted electrode. The other end of the wire could then be attached to the connection cable of the EIT system. This produced a lower impedance connection between the electrode and the EIT system than the gel electrodes. Particularly useful was the ability to use a basic multimeter to verify continuity between parts of the electrode to ensure the integrity of each electrode. The same process was used to verify that each electrode was properly connected to the EIT system before measurements were taken.

Finally in method C, the cylinders were immersed in water to reduce the overall impedance of the mortar. It was found that the painted silver electrodes would survive the immersion reasonably well, and any erosion could be easily repaired by applying more paint. Cylinders were allowed to sit in water for seven days until saturation, and surface water was removed with a cloth before measurements were taken. Otherwise the process was identical to method B.*A photograph some of the painted on electrodes electrodes is given by Fig. 4-3.*

Results using the method A were poor and did not produce usable inversions. Problems encountered during cylinder preparation included verification that the sponge was properly located and seated, and ensuring continuity from the electrode to the EIT system. Method B was easier to control and required less experimental work than the first. In spite of this it did not produce usable data when used with the available EIT equipment. Method C was a minor variation on method B in terms of preparatory work, but produced usable data.

Karhunen et al. (2010a) had success using gel to make contact between concrete and electrodes. It is possible that better results could have been obtained

here if the electrodes used were refined further. This was not undertaken in this instance since the third method was shown to work quite successfully. The results presented here should not discourage the use of gel electrodes in other work.

8.2.4 Image reconstruction in EIT

Here follows a basic description of the mathematical process of image reconstruction in electrical property imaging - for a more detailed treatment see Holder (2004). The fundamental goal of EIT is to infer a conductivity distribution σ within a medium Ω from voltage measurements $\mathbf{V}$ taken on the medium boundary $\partial\Omega$. This is in practice difficult to do well but the basic principles of image reconstruction can be understood intuitively.

EIT image reconstruction uses a sensitivity matrix (taking the form of $^{\partial V}/_{\partial \sigma}$ it is often referred to as "the Jacobian") relating the effect of each voltage measurement in $\mathbf{V}$ to each element in σ.

Reconstructing σ from $\mathbf{V}$ is an example of an ill-posed inverse problem. The difficulty comes from the fact that significant variations in σ can produce variations in $\mathbf{V}$ which are significant compared to the resolution at which measurements can be obtained. This means that for a given $\mathbf{V}$, there may be no unique σ. The image reconstruction algorithm must determine the most plausible σ possible with the collected data.

Many algorithms have been developed to find solutions to inverse problems. Tikhonov regularisation is particularly common in EPI, and is the method used for all image reconstructions in this work. It balances the influence of the noisy measured data against an assumed solution or type of solution ("prior"). In the case of Tikhonov regularisation this assumption is of a uniform distribution of resistivity, expressed by an identity matrix. The regularisation parameter (or hyperparameter) α is used to control the relative influence of the data and the prior. *As elsewhere in the project, TK-R is used over Total Variation (TV) because the inclusions were large enough that the benefits of TV were outweighed by the effort of implementing it.* This results in the Tikhonov functional which is to be minimised, shown in Eq. 8.1 from Kirsch (2011, p.37), in EIT terms.

$$||J\sigma - \mathbf{V}||^2 + \alpha||\sigma||^2 \tag{8.1}$$

Once the sensitivity matrix J is obtained, Tikhonov regularisation calculates the conductivity of the physical body from the measured data as shown in Eq. 8.2:

$$\sigma = (J^*J + \alpha L)^{-1} J^*\mathbf{V} \tag{8.2}$$

Where α is the regularisation parameter which is chosen before performing the calculation and L is the regularisation matrix, which for Tikhonov regularisation is an identity matrix of the necessary dimensions. However if information is already known about what σ *should* be, L can be modified to favour or penalise particular elements. This can also produce results which are misleading - see the section "Cheating with EIT" in Adler and Lionheart (2006) for more details.

A limitation of this method in the context of mortar and concrete NDT is the need for the user to choose and appropriate hyperparameter α. The quality of reconstruction when conductivity is so low relative to the available equipment is strongly dependent on the choice of the hyperparameter, as described in section 8.3. Additionally it does not appear that there is a reliable best setting for a given experimental configuration. This is an area where further work is needed before the technique can be applied to mortar and concrete bodies in which locations of defects are not known.

An image can be reconstructed from a single set of measurements (absolute imaging) but this is difficult in practice as it requires perfect correspondence between the computer model and experimental setup. Much more common is difference imaging, in which $\mathbf{V} = \mathbf{V}_1 - \mathbf{V}_2$ where $\mathbf{V}_1$ and $\mathbf{V}_2$ are two different sets of voltage measurements. Different voltage measurements may be the result of frequency dependent behaviour of materials within the boundary, as used in Frequency difference EIT (FdEIT) or some time-variance as in Time difference EIT (TdEIT).

The difficulty in time difference imaging is ensuring that the change which is interesting to the user is the only one represented in the measured data. For example, changes in the electrode position around the cylinder, changes in the impedance between the electrodes and the medium, or changes in the body shape (possibly as the result of introducing a crack) will all change the measurements in ways which may obfuscate the interesting feature. Some of these difficulties can be mitigated if FdEIT can be used, since in this case an image can be produced with two sets of data taken within a few minutes of each other. However FdEIT

requires that the background and feature to be distinguished exhibit sufficiently different frequency dependence in their conductivity. It also is more sensitive to errors between the physical experiment and computer model than TdEIT.

For this work, a method equivalent to TdEIT was used. While there was no actual time variance in any of the cylinder cross sections, a plain background cylinder provided data that was compared to readings from the cylinders with inclusions. This method was used as opposed to physically modifying the cylinders to avoid producing GP dust, which requires some safety protocols. Image reconstruction was done in Matlab using functions from the EIDORS library (Adler and Lionheart, 2006) and the Distmesh FEM meshing tool (Persson and Strang, 2004), which provide tested and verifiable software for EIT imaging.

Two hyperparameters were used and the results compared to the known cross-section of the cylinders; the differences in results arising from these changes are shown and discussed. Additionally a simple method for combining the results of multiple image reconstructions, described in section 8.2.5, was applied and compared to the results of the individual image reconstructions.

8.2.5 Combining images produced using different reconstruction parameters

The following describes a simple method for combining several image reconstructions at different parameters into a single image.

This method is based on the observation that less noise-dominated (higher α) image reconstructions often give good contrast between an inclusion and noise-related artefacts, but are less useful for assessing the actual size and details of the inclusion. Conversely an image reconstructed with a lower α often has better detail of the inclusion but more erroneous high contrast regions caused by noise. These noise regions cannot necessarily be distinguished from actual inclusions using only information present in a single image reconstruction. With this in mind a simple algorithm was developed to combine the relatively reliable low noise images with the higher detail of the high noise images, to improve usability and reduce the sensitivity to user selection of parameters.

The algorithm process is outlined below. The implementation used in this work was done in MATLAB and based on the EIDORS library, as with all of the

image reconstruction. The process is based on repeated image reconstructions on the same FEM mesh, which is simplified by the EIDORS default behaviour of caching and reusing meshes unless the user requests a recalculation. It would be possible to apply the method to dissimilar meshes provided they had very similar levels of coarseness by correlating elements in each mesh based on their location, but this was not necessary for this work.

$\sigma_{n\ large}$ produced by retaining a percentage of the highest and lowest valued elements within each σ_n and setting all others element values to zero.
for *each element within the mesh* **do**
  if *Current element value is non-zero in each* $\sigma_{n\ large}$ **then**
    Element added to σ_{all}
  end
  if *Current element value is non-zero in any* $\sigma_{n\ large}$ **then**
    Element added to σ_{any}
  end
end
(Note that σ_{all} is a subset of σ_{any})
Set $\sigma_{combined} = \sigma_{all}$
while *new connected elements were found on the last iteration* **do**
  for *each element in* σ_{all} **do**
    if *element in adjacent to one in* $\sigma_{combined}$ **then**
      Element from σ_{all} added to $\sigma_{combined}$
    end
  end
end
Elements from $\sigma_{combined}$ shown on original mesh

Algorithm 2: Basic process for combining the results of several independent image reconstructions.

8.3 Results

8.3.1 TK-R images from simulated and measured data

The following section presents the time difference imaging performed on the conductive mortar cylinders as described in section 8.2.4. Image reconstructions are all produced using EIDORS. Measurements were done at several excitation frequencies above 1kHz available using the KHU Mark 2.5 equipment. Inspection

of the raw data - done by comparing the shape of the data to the expected shape given the measurement and stimulation protocols - showed problems with the acquisition at higher frequencies, which were verified by the imaging results. Data taken at 1kHz and 5kHz were consistently found to be of expected shape. This does not guarantee good imaging results, and in fact none of the reconstructed images from 5kHz measurements were useful.

Note that the orientation of inclusions depends on their location relative to the electrodes. The physical experiments were performed such that the inclusions were generally closer to the number 1 electrode, but otherwise reconstructions have not had their orientations altered. Fig. 8-1 shows the cross-sections of each cylinder.

Fig. 8-2 shows simulated image reconstructions for all three cylinders as produced using EIDORS for the same geometry and similar conductivity distributions given in Fig. 8-1.

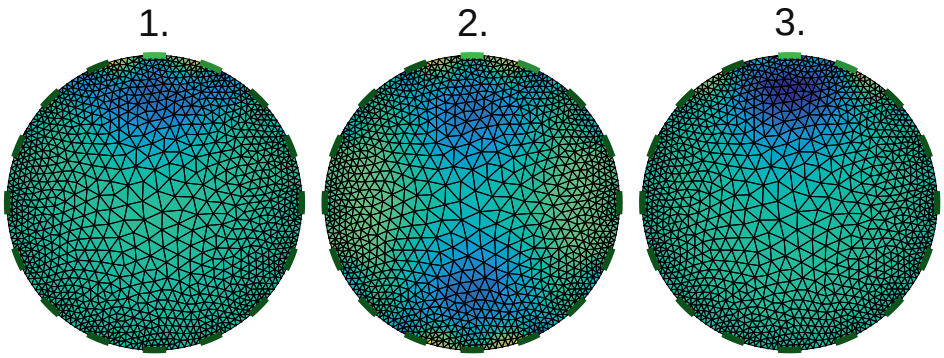

Figure 8-2: Simulation results for all cylinders. Images show the simulated reconstructions using a standard Tikhonov Regularisation process and $\alpha = 0.001$. Darker regions represent lower conductivity.

Figs. 8-3, 8-4 and 8-5 show TK-R image reconstructions on cylinders 1, 2 and 3 respectively at different hyperparameters.

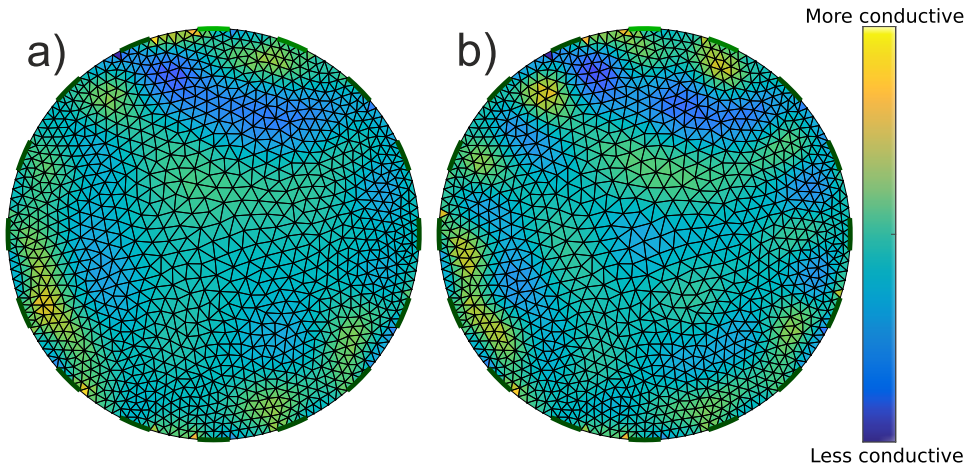

Figure 8-3: Reconstructed images of cylinder 1 at 1kHz. In a) $\alpha = 0.001$ and in b) $\alpha = 0.0001$.

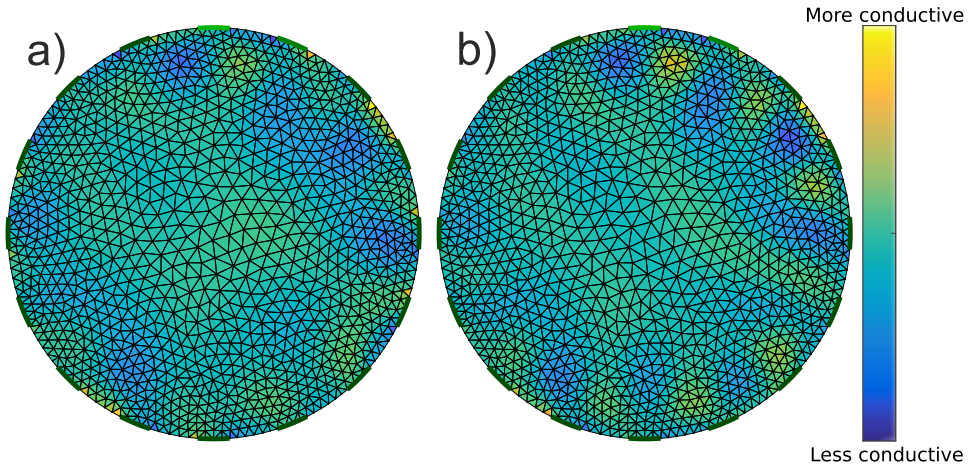

Figure 8-4: Reconstructed images of cylinder 2 at 1kHz. In a) $\alpha = 0.001$ and in b) $\alpha = 0.0001$.

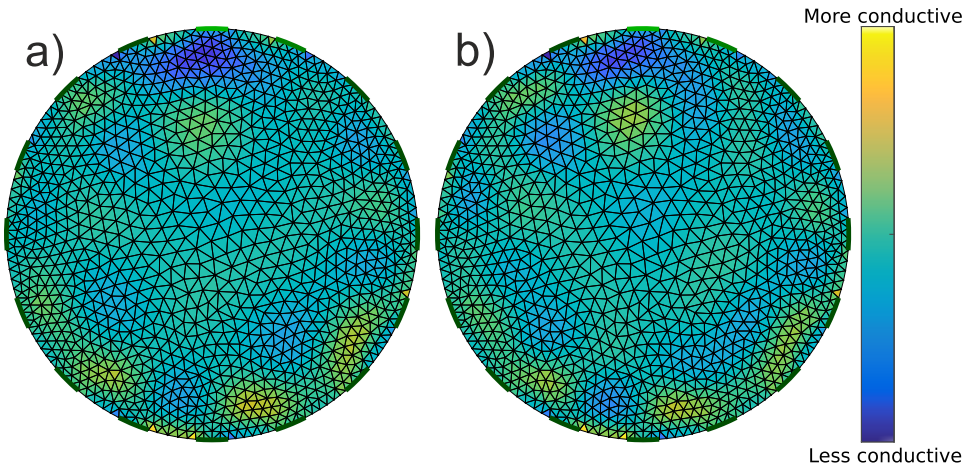

Figure 8-5: Reconstructed images of cylinder 3 at 1kHz. In a) $\alpha = 0.001$ and in b) $\alpha = 0.0001$.

8.3.2 Combined images

The following shows the results of the combination of the images shown in section 8.3.1 using the method described in section 8.2.5. Unlike in the individual image reconstructions, each of the highlighted elements is shown as having negative or positive conductivity relative to the rest of the image. This is because the reconstructed conductivity values for each cylinder vary depending on α, so each element likely has a different conductivity in each constituent image.

Results from the method are shown in Fig. 8-6. In this case each combined image has been produced using three images for each cylinder at $\alpha = 0.01$, $\alpha = 0.001$ and $\alpha = 0.0001$, and has retained top top and bottom 10% of elements from each constituent image.

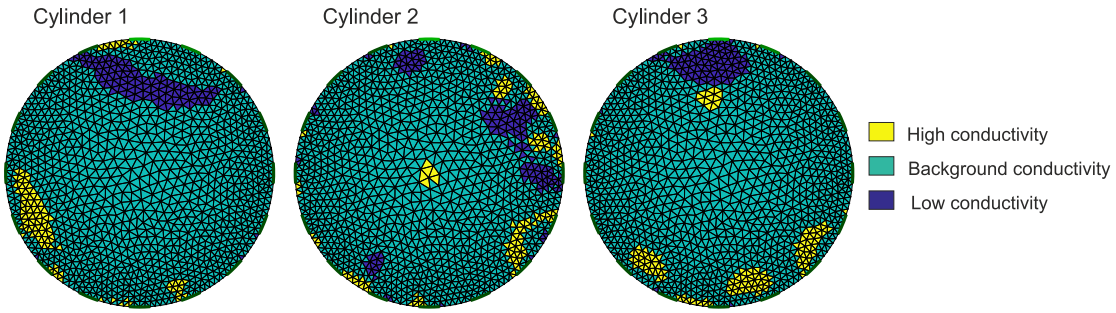

Figure 8-6: The results of combining the TK-R images according to the process described in section 8.2.5.

8.4 Discussion

8.4.1 Overall reconstruction quality of individual TK-R images

The simulated and actual reconstructions are compared to assess the quality of the experimental and computational procedure. As previously noted, the general quality of the results can be described as:

- Cylinder 1 is a close representation of the actual physical cross-section, and somewhat better than would be expected from the simulation.
- Cylinder 2 does not resemble the physical situation, and is worse than would be expected from the simulation.
- Cylinder 3 also does not resemble the cross-section of the cylinder, but is good in the context of the simulated reconstruction.

It is interesting to compare the reconstructions - actual and simulated - of cylinders 1 and 2. The inclusions are of the same size and shape, and similar location and orientation relative to the cylinder boundary. However the slots in cylinder 2 are slightly further from the boundary than the one in cylinder 1. This distance has a substantial effect on the reconstruction quality, suggesting that the inclusion in cylinder 1 is close to the maximum depth that could be measured by this experimental configuration.

Choice of image reconstruction parameters

Section 8.3 shows tomograms using various image reconstruction parameters. It is clear from observing these tomograms that there is no single correct set of reconstruction parameters to achieve the "best" image. Changes to α can introduce more detail, but do so at the cost of introducing ambiguity as to which regions in the image represent features and which are caused by noise.

Measurements were taken at a variety of frequencies, with only the 1kHz data being useful. This is an impediment for the use of EIT in industry, since in an actual NDT context the settings cannot be altered until the result best matches the actual physical case since that case is not known.

This problem also does not necessarily affect higher voltage equipment.

8.4.2 Combined images using different reconstruction parameters

Combined images produced using the algorithm described by section 8.2.5 are compared to the single images produced using TK-R as well as to the specimens. The effects of such an image combination method on the practicality of EIT for SHM use is also considered.

The results of the combination of the reconstructions for cylinders 1 and 3 are generally similar in character to the individual reconstructions. The combination algorithm remains vulnerable to some erroneous regions since while their intensity may change, their location does not.

The combination of cylinder 2 is perhaps slightly closer to the physical situation than the constituent images. Each of the less conductive regions is approximately within what should be a less conductive region (when considering the rotational shift of the tomograms), and the ends of the less conductive region in the top right appear to be represented. However, the shape and size of the inclusions are not properly represented. If the percentage of included elements were increased the reconstruction quality may increase, but knowledge of the cylinder cross-section would be required to know to do this.

The results from the combination algorithm are all at least as good as the individual image reconstructions that were produced. Although in some cases there are also no significant benefits to the combination, the only disadvantage

in this context is the additional computational time. In this context of distinguishing high contrast inclusions for SHM, it is unlikely that online imaging will be beneficial or necessary so combining images represents a small cost for some potential benefit.

Effects of the combination process on overall usability of EIT for SHM applications

The intent of the combination algorithm was to provide a way of enhancing the usability of EIT for SHM applications by reducing the barrier to entry for users without experience using EIT. It is useful to compare the dependence on user selection of parameters in individual image reconstruction with the combination method.

Whereas in the typical process the user must supply a single value of α, in the combination method a range of α must be supplied. The need to supply α values remains but the outcome is less dependent on an individual value. While in single image reconstruction it may be necessary to test different α, once a range of values is set it can be used repeatedly.

In the combination method a new parameter is required, the fraction of elements retained from each image. This is not analogous to any requirement of individual image reconstruction but unlike the hyperparameter it relates directly to a physical property of the material under test.

The result of both of these methods is also related to the quality and appropriateness of the finite element mesh being used. Individual image reconstruction and the combination method are equally dependent on this, and the combination method does not have any advantage or disadvantage in this regard.

It may be feasible to select parameters by using a genetic algorithm, given enough training data and an appropriate method of quantifying image quality. This could replace the image combination method or work in conjunction with it. With this the need for user judgement might be reduced further.

It is important to note that the combination method as described is suitable for imaging the most extreme regions of contrast within the material under test. This is useful in the current crack detection application, but would be a disadvantage in any application where there is a requirement to fully reconstruct the conductivity distribution with a number of regions at different conductivity

values.

8.4.3 Effects of changes to the experimental method

A variety of experimental methods were tried, as described in section 8.2.3. The results when using methods A and B did not reflect the actual cross section of the cylinders, while method C was successful in some cases when used with the right image reconstruction parameters.

These outcomes were compared to the measurement noise observed with each method. Fifty full sets of measurements were taken for each cylinder at each stimulation frequency for the purposes of averaging. Measurement noise can be simply quantified as the Relative Standard Deviation (RSD) of the fifty data points for each combination of driving and measurement electrode pair. This was compared for each of the connection methods at 1kHz stimulation.

Comparing RSDs, it was found that the method C measurements were the least noisy, with method B (similar to method C with an entirely dry body) being the most noisy. Measurement noise in terms of RSD was also compared for each individual cylinder with the method C connection. The largest RSDs were generally in measurements on cylinder 1, which did return results that were not representative of the actual cross-section. Comparing the RSDs of each measurement to the reconstructions demonstrates that measurement noise is not the sole, or even apparently main, cause of poor image reconstructions.

The increase in quality when comparing the conductive and non-conductive mortars indicates that such issues could be mitigated with the use of high voltage measurement equipment, though this brings issues of increased cost of equipment and safety. A combination of development of electrode configurations and use materials intended to facilitate EIT would mitigate these issues for its future use in SHM.

8.4.4 Applicability to concrete

The results presented here were obtained with mortar, but concrete is the more interesting material from the perspective of industrial use. Concrete is less conductive in general than mortar (McCarter, 1996) but otherwise EIT is feasible using appropriate equipment (Karhunen et al., 2010a). In general controlling the

conductivity of the concrete can only be achieved through modifications to the cement paste as the aggregates must be chosen to meet structural requirements. While the work did not test concrete, its conclusions are applicable to concrete for these reasons.

One of the motivations for the use of EIT - and potentially other NDT methods on concrete - is the validation of the performance of self-healing concrete, as described in section 8.1. A literature search has not found any work investigating the effects of the presence of CBM additions on self-healing concrete mechanisms. Some study into the compatibility of self-healing concrete technologies with these additions is necessary before they can be recommended to facilitate NDT in this particular application.

8.5 Conclusions

In general, it is difficult to obtain EIT images of mortar on typical EIT equipment in spite of increased conductivity. Concrete is expected to be more difficult that mortar to image due to the differences in the material composition. Of the three conductive cylinders, standard EIT methods produced good images of cylinder 1, with the less conductive region being discernible at a range of image reconstruction parameters. These images were better than those simulated on the same geometry. Standard methods did not produce usable images with cylinder 2, but a combination of several images was able to produce slightly better agreement with the true geometry. Images of cylinder 3 were as good as could be expected given the simulated results, but not a reflection of the true geometry. In general features closer to the boundary were easier to image. Because of the nature of crack formation, with cracks forming at the surface, this is not a serious limitation for the use of EIT on concrete.

In spite of the conductivity of the mortar relative to conventional mortar, with the low-voltage equipment it was still necessary to immerse the cylinders in water to obtain reasonable results. Immersion in water may be also be advantageous for real-life EIT for Structural Health Monitoring (SHM) for increasing the frequency dependence of the mortar electrical properties, increasing the contrast between background and inclusion for FDEIT. However water immersion will also impractical in many cases. The improvement in imaging from increasing

conductivity also confirms that EIT imaging of mortar and concrete would be easier if specialist equipment capable of driving higher voltages could be used.

Comparing the images using different reconstruction parameters, as well as different frequencies, shows the difficulty in choosing the best settings and parameters for EIT on the mortar. A relatively simple algorithm for combining reconstructions has been proposed and shown to produce results at least as good as the individual reconstructions, but this still requires that at least some of the images fed into it have been done with reasonably good settings. It also does not totally remove the need for user judgement; a number of top and bottom elements must be selected. This is an area with potential for further work, potentially making some use of machine learning.

A final consideration is in relation to using conductive additions to facilitate EIT verification of self-healing concrete. Work is needed to assess the effects of these additions on the self-healing processes, possibly through destructive testing or observations at the concrete surface, before such a technique can be used.

8.6 Data access statement

Data collected during this study is freely available at https://doi.org/10.15125/BATH-00567.

8.7 Compliance with ethical standards

The authors declare that they have no conflicts of interest.
No human participants or animals were involved.
Informed consent issues were not relevant to this work.

8.8 Supplemental work

Following the work on imaging of mortar cylinders, the image combination algorithm described in Section 8.2.5 (reproduced in Section 4.6.5) was applied to the imaging attempts from Chapter 5. This was not included in the paper because the amount of context required would have made it too long.

This used the same data as Chapter 5. The exact same procedure for the image combination as in Section 8.2.5 was used. The individual images were produced according to the same procedure as during the original imaging work. For the dental plaster cylinders this is described by Section 4.3.1 and for the concrete cylinders this is described by Section 4.3.2. These were FDEIT reconstructions, and used the 10kHz and 50kHz data. In all cases, α values of 0.01, 0.001 and 0.0001 were used. As in the combinations of conductive mortar cylinders, the threshold was set at 10%. The diagram of the plaster cylinder cross sections and the photographs of the concrete cylinders from Sections 4.3.2 and 5.1 are reproduced here to remind the reader of the target images.

8.8.1 Results and discussion of the image combination algorithm applied to EIT images produced earlier in the project.

Fig. 8-7 gives the cross-sections of the plaster cylinders. Fig. 8-8 shows the results of the image combination algorithm applied to each of the cylinders.

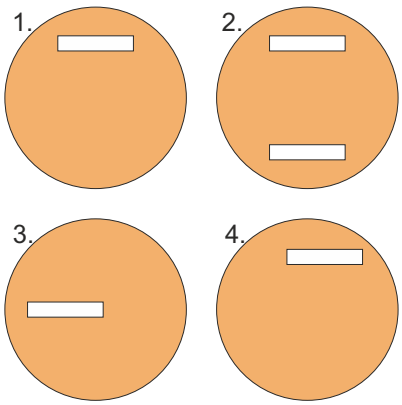

Figure 8-7: Numbered plaster cylinder cross sections.

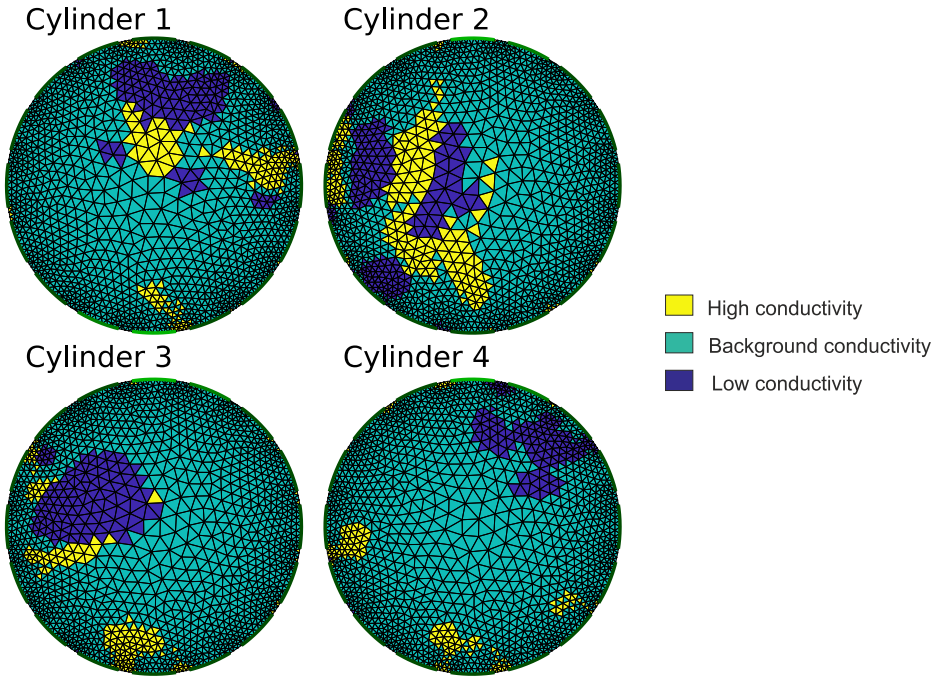

Figure 8-8: The results of combining the dental plaster image reconstructions. Each constituent image is an FDEIT reconstruction using 10kHz and 50kHz, and α values were 0.01, 0.001 and 0.0001.

Fig. 8-7 gives the cross-sections of the plaster cylinders. Fig. 8-8 shows the results of the image combination algorithm applied to each of the cylinders.

Of the dental plaster reconstructions presented in Section 5.1.1, cylinders 1 and 3 were good representations of the real cross sections and cylinders 2 and 4 were not. Here cylinder 2 is totally unrecognisable and does not represent the real cross section at all. Cylinders 1 and 3 are, as the original reconstructions were, fairly good representations. Cylinder 1 has some fairly large erroneous more conductive regions, but represents the inclusion quite well. Cylinder 3 has fewer erroneous regions but distorts the shape of the inclusion substantially, although its orientation and position are reasonably good. In the original reconstructions for cylinder 4 (see Fig. 5-6) the inclusion was not discernible. The combination image, while by no means completely accurate, is a better representation of the actual cross section. The location is well represented, and the width of the entire top right region is reasonably accurate. However the shape is very poorly represented, and it is difficult to say with any confidence what an operator not aware of the actual nature of the inclusion would expect the cutout to look like

Figure 8-9: The three concrete samples.

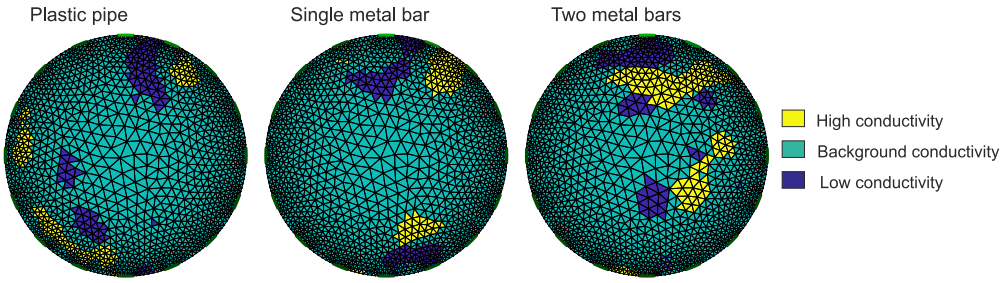

Figure 8-10: The results of combining the concrete image reconstructions. Each constituent image is an FDEIT reconstruction using 10kHz and 50kHz, and α values were 0.01, 0.001 and 0.0001.

based on this image.

The combinations of the concrete images, much like the reconstructions presented in Section 5.2.1, basically do not represent the physical situations.

Applying the combination method to these images yields generally the same results as it did to the conductive mortar cylinders; the result is dependent on the quality of the input data, and is at least as good as the constituent images, without necessarily being any better. The conclusions from Section 8.5 apply here also; combination of images produces results at least as good as the input images, but still requires the user to intelligently make decisions about reconstruction parameters.

9 | Conclusions and further work

9.1 Conclusions

Performing Electrical Impedance Tomography (EIT) on cementitious materials remains difficult. This project set out with the general aim of developing EIT techniques to detect and classify cracks in concrete, with a particular aim to be able to apply it to self-healing concrete.

The project objectives as stated in Section 1.2 were:

1. Assess the feasibility of using EIT on concrete using the available equipment
2. Investigate the electrical properties of concrete containing conductive additions, and thus determine how best to produce a concrete that can be imaged using the available equipment
3. Develop a methodology for performing EIT imaging on this conductive concrete with the available equipment

As discussed in Section 1.2.1 mortar was substituted for concrete in work after the first attempt at imaging concrete, but the findings still apply to concrete.

Though EIT is a promising technology for Structural Health Monitoring (SHM) and Non-Destructive Testing (NDT) in civil engineering, particularly with respect to smart structures, there is still work to be done before it can find acceptance industrially.

9.1.1 Objective one

Objective one was completed through the initial work in Chapter 5 which showed that imaging of mature concrete with the available equipment was at best extremely difficult.

The work on dental plaster suggested that Frequency Difference Electrical Impedance Tomography (FDEIT) would be feasible using the available equipment. The results when trying to apply Time Difference Electrical Impedance Tomography (TDEIT) reinforced the importance of maintaining agreement between the electrode locations in each cylinder to be measured as well as the computer model, and particular attention was paid to this in the subsequent imaging work.

The work on concrete was unsuccessful in producing useful image reconstructions. Based on the relative success of the plaster imaging work and the concentration on early-age concrete in the literature, this was believed to be the result of the relatively high resistivity of the concrete. Attempts to reduce the impedance between electrodes by altering the electrode configuration were relatively successful but EIT even in the ideal case was still unsuccessful.

The difficulty in applying EIT to the concrete cylinders informed the direction of the rest of the project, and the decisions was made that the best contribution could be made by concentrating on subjects related to practicalities of applying EIT.

9.1.2 Objective two

Objective two was completed through the comprehensive study of mortar resistivity in Chapter 6. Two carbonaceous additions (Graphite Powder (GP) and Carbon Fibre Powder (CFP)) were tested and found to be very similar in terms of magnitude change to the resistivity but they did have noticeably different effects on the shape of the Nyquist plots they produced.

Both additions required higher water content than typical mortar mixes in order to mix properly. Safety considerations when working with the materials were also significant.

The quantity of conductive addition is the strongest influencer of resistivity in a mix where one is present, followed by w/c ratio and lastly g/s. Changes to the w/c and g/s ratios do alter resistivity but not the shape of the Nyquist plots in the same way that the conductive additions do.

Some further experimental work would be necessary to apply mathematical models to the measured data on the mortars as described in Chapter 7, but this

was not necessary for the completion of the objective.

9.1.3 Objective three

Objective three was completed by the imaging of conductive mortar cylinders as described in Chapter 8. The conductive mortar was chosen from the study of mortar resistivity. The selection was made to balance reduction in resistivity with difficulty in workability, increased danger in the manufacturing process, and cost of the experiment.

Even with the reduced resistivity of the mortar, EIT imaging remains difficult. Several experimental configurations were tested and finally a method involving the use of silver painted electrodes on a cylinder saturated with water produced some images of reasonable quality. The same electrode configuration, without the saturation, did not produce useful results, showing the importance of increasing conductivity as far as possible. The experiment showed again the sensitivity of EIT on resistive materials to the electrode configuration - the computer model and experiment must agree very closely in electrode configuration, and if another experiment is to be used as a background this must also agree very closely with the first two.

A simple method for combining image reconstructions was developed and demonstrated. This was intended to reduce the sensitivity of the quality of results to the level of operator expertise, in service of the project's overall focus on the practicalities of using EIT industrially. The method was tested using all of the other EIT results produced for the project, and led to some level of improvement in three cases and at least did not make things any worse in the others.

9.2 Further work

The project has opened up several possible avenues for further work. There are two questions in particular that should be investigated to develop a better understanding of appropriate usage cases for conductive mortars:

- Do the relationships between resistivity and factors of mix design hold when coarse aggregates are introduced?

- How does the reduction in resistivity affect the vulnerability of the material to corrosion, especially in cases where reinforcement is present?

These questions are relevant not only for the use of conductive additions to facilitate imaging, but for self-heating and other applications too. Some further experimental work would also help in applying theoretical models to the electrical properties of the conductive mortars, which would be useful for future mix design work. The original motivation for the project was to apply the technologies involved to self-healing concrete, and there are some investigations that will need to be carried out to start this process:

- Does the presence of conductive additions affect the self-healing performance of the concrete?
- Does the self-healing process have any effect on the effectiveness of EIT, for example through changes to the resistivity of the concrete?

Both of these investigations would apply to any of the variety of mechanisms by which self-healing concretes can work.

Other aspects of the project, including the imaging side, are perhaps more open ended. Some possible next steps include:

- Investigation of impedance for concrete mixes including additions such as plasticisers, in order to verify that the data is applicable to concretes that might be used industrially. Plasticisers are particularly important as they would most likely be necessary to mitigate the negative effects that carbonaceous powders have on workability characteristics.
- Testing the methodology with physically smaller inclusions and attempting to achieve the necessary resolution. Resolution improvements may come from the use of more sophisticated image reconstruction algorithms, particularly iterative algorithms, or by changes to measurement protocols such as the rotational system investigated by Murphy et al. (2017).
- Attempting 3D EIT (as has been performed by Smyl et al. (2016)) on cylinders with non-constant cross-section.
- Imaging of cylinders with relatively conductive as well as resistive inclusions.

- Systematic comparison of the results using EIT to other imaging and NDT methods used for crack detection and classification. Ground Penetrating Radar (GPR) and ultrasound based methods are the most likely to be in competition with EIT and should be prioritised.

Bibliography

Abbas, S., Soliman, A. M. and Nehdi, M. L. (2015), 'Exploring mechanical and durability properties of ultra-high performance concrete incorporating various steel fiber lengths and dosages', *Construction and Building Materials* **75**, 429–441.

Acoustic Control Systems (2014), 'Ultrasonic tomograph for imaging of concrete structures A1040 MIRA'.
URL: *http://www.acsys.ru/eng/production/detail/a1040-mira/*

Adler, A., Arnold, J. H., Bayford, R., Borsic, A., Brown, B., Dixon, P., Faes, T. J. C., Frerichs, I., Gagnon, H., Gärber, Y., Grychtol, B., Hahn, G., Lionheart, W. R. B., Malik, A., Patterson, R. P., Stocks, J., Tizzard, A., Weiler, N. and Wolf, G. K. (2009), 'GREIT: a unified approach to 2D linear EIT reconstruction of lung images.', *Physiological measurement* **30**(6), S35–55.

Adler, A., Gaggero, P. O. and Maimaitijiang, Y. (2011), 'Adjacent stimulation and measurement patterns considered harmful.', *Physiological measurement* **32**(7), 731–44.

Adler, A. and Lionheart, W. R. B. (2006), 'Uses and abuses of EIDORS: an extensible software base for EIT.', *Physiological measurement* **27**(5), S25–42.

Afzal, M. B., Kabir, S. and Sidek, O. (2012), 'An In-depth Review: Structural Health Monitoring using Fiber Optic Sensor', *IETE Technical Review* **29**(2), 105.

Aggelis, D. G., Leonidou, E. and Matikas, T. E. (2012), 'Subsurface crack determination by one-sided ultrasonic measurements', *Cement and Concrete Composites* **34**(2), 140–146.

Agilent Technologies (n.d.), *Agilent Impedance Measurement Handbook*.

Alazhari, M., Sharma, T., Heath, A., Cooper, R. and Paine, K. (2018), 'Application of expanded perlite encapsulated bacteria and growth media for self-healing concrete', *Construction and Building Materials* **160**, 610–619.

Alwan, Z., Jones, P. and Holgate, P. (2017), 'Strategic sustainable development in the UK construction industry, through the framework for strategic sustainable development, using Building Information Modelling', *Journal of Cleaner Production* **140**, 349–358.

Amer-Yahia, C. and Majidzadeh, T. (2012), 'Inspection of Insulated Concrete Form walls with Ground Penetrating Radar', *Construction and Building Materials* **26**(1), 448–458.

Ammari, H., Seo, J. K., Zhang, T. and Zhou, L. (2014), 'Electrical impedance spectroscopy-based nondestructive testing for imaging defects in concrete structures'.

Barber, C., Brown, B. and Freeston, I. (1983), 'Imaging spatial distributions of resistivity using applied potential tomography', *Electronics Letters* **19**(22), 933.

Barsoukov, E. and Macdonald, J. R. (1987), *Impedance spectroscopy : emphasizing solid materials and systems*, Wiley, New York ; Chichester.

Boland, C. S., Khan, U., Ryan, G., Barwich, S., Charifou, R., Harvey, A., Backes, C., Li, Z., Ferreira, M. S., Möbius, M. E., Young, R. J. and Coleman, J. N. (2016), 'Sensitive electromechanical sensors using viscoelastic graphene-polymer nanocomposites', *Science* **354**(6317), 1257–1260.

Boverman, G., Kao, T. J., Kulkarni, R., Kim, B. S., Isaacson, D., Saulnier, G. J. and Newell, J. C. (2008), 'Robust linearized image reconstruction for multifrequency EIT of the breast', *IEEE Transactions on Medical Imaging* **27**(10), 1439–1448.

Brantervik, K. and Niklasson, G. A. (1991), 'Circuit models for cement based materials obtained from impedance spectroscopy', *Cement and Concrete Research* **21**(4), 496–508.

Capozzoli, L. and Rizzo, E. (2017), 'Combined NDT techniques in civil engineering applications: Laboratory and real test', *Construction and Building Materials* **154**, 1139–1150.

Carriço, A., Bogas, J. A., Hawreen, A. and Guedes, M. (2018), 'Durability of multi-walled carbon nanotube reinforced concrete', *Construction and Building Materials* **164**, 121–133.

Chen, M., Gao, P., Geng, F., Zhang, L. and Liu, H. (2017), 'Mechanical and smart properties of carbon fiber and graphite conductive concrete for internal damage monitoring of structure', *Construction and Building Materials* **142**, 320–327.

Chew, S., Zulkifli, A., Hamad, H., Harun, S., Lee, L., Razak, H. and Adikan, F. (2018), 'Singlemode-multimode-singlemode fiber structure as compressive strain sensor on a reinforced concrete beam', *Optik - International Journal for Light and Electron Optics* **154**, 705–710.

Choi, H. J., Kim, M. S., Ahn, D., Yeo, S. Y. and Lee, S. (2019), 'Electrical percolation threshold of carbon black in a polymer matrix and its application to antistatic fibre', *Scientific Reports* **9**(1), 1–12.

Choi, M. H., Kao, T. J., Isaacson, D., Saulnier, G. J. and Newell, J. C. (2007), 'A reconstruction algorithm for breast cancer imaging with electrical impedance tomography in mammography geometry', *IEEE Transactions on Biomedical Engineering* **54**(4), 700–710.

Chu, H. Y. and Chen, J. K. (2016), 'The experimental study on the correlation of resistivity and damage for conductive concrete', *Cement and Concrete Composites* **67**, 12–19.

Cruz, J. M., Fita, I. C., Soriano, L., Payá, J. and Borrachero, M. V. (2013), 'The use of electrical impedance spectroscopy for monitoring the hydration products of Portland cement mortars with high percentage of pozzolans', *Cement and Concrete Research* **50**, 51–61.

De Belie, N., Gruyaert, E., Al-Tabbaa, A., Antonaci, P., Baera, C., Bajare, D., Darquennes, A., Davies, R., Ferrara, L., Jefferson, T., Litina, C., Miljevic, B., Otlewska, A., Ranogajec, J., Roig-Flores, M., Paine, K., Lukowski, P., Serna,

P., Tulliani, J.-M., Vucetic, S., Wang, J. and Jonkers, H. M. (2018), 'A Review of Self-Healing Concrete for Damage Management of Structures', *Advanced Materials Interfaces* p. 1800074.

Demčenko, A., Visser, H. A. and Akkerman, R. (2016), 'Ultrasonic measurements of undamaged concrete layer thickness in a deteriorated concrete structure', *NDT and E International* **77**, 63–72.

Dérobert, X., Lataste, J., Balayssac, J. and Laurens, S. (2017), 'Evaluation of chloride contamination in concrete using electromagnetic non-destructive testing methods', *NDT & E International* **89**, 19–29.

Dhir, R. K., McCarthy, M. J., Zhou, S. and Tittle, P. A. J. (2004), 'Role of cement content in specifications for concrete durability: cement type influences', *Proceedings of the Institution of Civil Engineers - Structures and Buildings* **157**(2), 113–127.

Ding, Y., Huang, Y., Zhang, Y., Jalali, S. and Aguiar, J. (2015), 'Self-monitoring of freeze–thaw damage using triphasic electric conductive concrete', *Construction and Building Materials* **101**, 440–446.

Dyer, T. (2014), *Concrete Durability*, CRC Press.

Easy Composites (n.d.*a*), 'Easy composites aluminium metal powder', `https://www.easycomposites.co.uk/#!/resin-gel-silicone-adhesive/filler-powders-and-additives/metal-powders/aluminium-metal-filler-powder.html`. Accessed 17/02/2020.

Easy Composites (n.d.*b*), 'Easy composites graphite powder', `https://www.easycomposites.co.uk/#!/resin-gel-silicone-adhesive/filler-powders-and-additives/general-fillers-and-additives/graphite-pigment-powder-low-friction.html`. Accessed 17/02/2020.

Easy Composites (n.d.*c*), 'Easy composites milled carbon fibre powder', `https://www.easycomposites.co.uk/#!/resin-gel-silicone-adhesive/filler-powders-and-additives/general-fillers-and-additives/milled-carbon-fibre-powder.html`. Accessed 17/02/2020.

Fares, M., Fargier, Y., Villain, G., Derobert, X. and Lopes, S. P. (2016), 'Determining the permittivity profile inside reinforced concrete using capacitive probes', *NDT and E International* **79**, 150–161.

Feng, D. and Feng, M. Q. (2018), 'Computer vision for SHM of civil infrastructure: From dynamic response measurement to damage detection – A review'.

Floyd, T. (2010), *Principles of Electric Circuits: Conventional Current Version*, ninth edition edn, Pearson.

Forde, M. C., McCarter, W. J. and Whittington, H. W. (1981), 'Resistivity Characteristics of Concrete', *ICE Proceedings* **71**(1), 107–117.

Frazão, C., Camões, A., Barros, J. and Gonçalves, D. (2015), 'Durability of steel fiber reinforced self-compacting concrete', *Construction and Building Materials* **80**, 155–166.

Gomis, J., Galao, O., Gomis, V., Zornoza, E. and Garcés, P. (2015), 'Self-heating and deicing conductive cement. Experimental study and modeling', *Construction and Building Materials* **75**, 442–449.

González, G., Kolehmainen, V. and Seppänen, A. (2017), 'Isotropic and anisotropic total variation regularization in electrical impedance tomography', *Computers and Mathematics with Applications* **74**(3), 564–576.

Gorse, C., Johnston, D. and Pritchard, M. (2012), *A Dictionary of Construction, Surveying and Civil Engineering*, Oxford University Press.

Hallaji, M. and Pour-Ghaz, M. (2014), 'A new sensing skin for qualitative damage detection in concrete elements: Rapid difference imaging with electrical resistance tomography', *NDT & E International* **68**, 13–21.

Hallaji, M., Seppänen, A. and Pour-Ghaz, M. (2015), 'Electrical resistance tomography to monitor unsaturated moisture flow in cementitious materials', *Cement and Concrete Research* **69**, 10–18.

Han, B., Wang, Y., Dong, S., Zhang, L., Ding, S., Yu, X. and Ou, J. (2015), 'Smart concretes and structures: A review', *Journal of Intelligent Material Systems and Structures* **26**(11), 1303–1345.

Hansen, P. C. (1987), 'The truncatedSVD as a method for regularization', *BIT* **27**(4), 534–553.

Holder, D. S. (2004), *Electrical Impedance Tomography: Methods, History and Applications*, CRC Press.

Hornbostel, K., Larsen, C. K. and Geiker, M. R. (2013), 'Relationship between concrete resistivity and corrosion rate – A literature review', *Cement and Concrete Composites* **39**, 60–72.

Hou, T. and Lynch, J. P. (2008), 'Electrical Impedance Tomographic Methods for Sensing Strain Fields and Crack Damage in Cementitious Structures', *Journal of Intelligent Material Systems and Structures* **20**(11), 1363–1379.

Hou, Z., Li, Z. and Wang, J. (2007), 'Electrical conductivity of the carbon fiber conductive concrete', *Journal of Wuhan University of Technology–Materials Science Edition* **22**(2), 346–349.

Hou, Z., Li, Z. and Wang, J. (2010), 'Electrically conductive concrete for heating using steel bars as electrodes', *Journal Wuhan University of Technology, Materials Science Edition* **25**(3), 523–526.

Hu, X., Shi, C., Liu, X., Zhang, J. and de Schutter, G. (2019), 'A review on microstructural characterization of cement-based materials by AC impedance spectroscopy', *Cement and Concrete Composites* **100**, 1–14.

Huang, B. S., Qin, L., Ren, H. W., Hua, Z. X. and Tian, K. G. (2016), 'ERT Imaging of Graphite Electrically Conductive Concrete', *Key Engineering Materials* **680**, 388–391.

Huang, Y., Ellingford, C., Bowen, C., McNally, T., Wu, D. and Wan, C. (2020), 'Tailoring the electrical and thermal conductivity of multi-component and multi-phase polymer composites', *International Materials Reviews* **65**(3), 129–163.

Ioannou, S. (2012), An assessment of the performance of calcium sulfoaluminate and supersulfated cements for use in concrete, PhD thesis, University of Bath.

Jorcin, J. B., Orazem, M. E., Pébère, N. and Tribollet, B. (2006), CPE analysis by local electrochemical impedance spectroscopy, *in* 'Electrochimica Acta', Vol. 51, Pergamon, pp. 1473–1479.

Karhunen, K. (2013), Electrical Resistance Tomography Imaging of Concrete, PhD thesis, University of Eastern Finland.

Karhunen, K., Seppänen, A., Lehikoinen, A., Blunt, J., Kaipio, J. P. and Monteiro, P. J. M. (2010a), 'Electrical Resistance Tomography for Assessment of Cracks in Concrete', *Materials Journal* **107**(5).

Karhunen, K., Seppänen, A., Lehikoinen, A., Monteiro, P. J. and Kaipio, J. P. (2010b), 'Electrical Resistance Tomography imaging of concrete', *Cement and Concrete Research* **40**(1), 137–145.

Khalid, T., Albasha, L., Qaddoumi, N. and Yehia, S. (2017), 'Feasibility Study of Using Electrically Conductive Concrete for Electromagnetic Shielding Applications as a Substitute for Carbon-Laced Polyurethane Absorbers in Anechoic Chambers', *IEEE Transactions on Antennas and Propagation* **65**(5), 2428–2435.

Kim, J. W., Kim, J., Park, S. and Oh, T. K. (2014), 'Integrating embedded piezoelectric sensors with continuous wavelet transforms for real-time concrete curing strength monitoring', *Structure and Infrastructure Engineering* **11**(7), 897–903.

Kirsch, A. (2011), *An Introduction to the Mathematical Theory of Inverse Problems*, Vol. 120 of *Applied Mathematical Sciences*, Springer New York, New York, NY.

Kourunen, J., Savolainen, T., Lehikoinen, A., Vauhkonen, M. and Heikkinen, L. M. (2009), 'Suitability of a PXI platform for an electrical impedance tomography system', *Measurement Science and Technology* **20**(1), 015503.

Kozlov, A. V. and Kozlov, V. N. (2015), 'The development and current state of methods for the nondestructive testing and acoustic tomography of concrete', *Russian Journal of Nondestructive Testing* **51**(6), 329–337.

Kunieda, M., Ueda, N. and Nakamura, H. (2014), 'Ability of recycling on fiber reinforced concrete', *Construction and Building Materials* **67**(PART C), 315–320.

Liu, S. H., Wu, M. Q., Rao, M. J., Li, L. H. and Xiao, H. L. (2019), 'Preparation, Properties, and Microstructure of Graphite Powder-Containing Conductive Concrete', *Strength of Materials* **51**(1), 76–84.

Ma, L. and Soleimani, M. (2017), 'Magnetic induction tomography methods and applications: a review', *Measurement Science and Technology* **28**(7).

Maleki, P., Iranpour, B. and Shafabakhsh, G. (2017), 'Investigation of de-icing of roads with conductive concrete pavement containing carbon fibre-reinforced polymer (CFRP)', *International Journal of Pavement Engineering* pp. 1–9.

Martínez-Moreno, F. J., Delgado-Ramos, F., Galindo-Zaldívar, J., Martín-Rosales, W., López-Chicano, M. and González-Castillo, L. (2018), 'Identification of leakage and potential areas for internal erosion combining ERT and IP techniques at the Negratín Dam left abutment (Granada, southern Spain)', *Engineering Geology* **240**, 74–80.

Mason, T. O., Campo, M. A., Hixson, A. D. and Woo, L. Y. (2002), 'Impedance spectroscopy of fiber-reinforced cement composites', *Cement and Concrete Composites* **24**(5), 457–465.

McCarter, W. J. (1994), 'A parametric study of the impedance characteristics of cement-aggregate systems during early hydration', *Cement and Concrete Research* **24**(6), 1097–1110.

McCarter, W. J. (1996), 'The a.c. impedance response of concrete during early hydration', *Journal of Materials Science* **31**(23), 6285–6292.

McCarter, W. J., Garvin, S. and Bouzid, N. (1988), 'Impedance measurements on cement paste', *Journal of Materials Science Letters* **7**(10), 1056–1057.

McCarthy, M. J., Giannakou, A. and Jones, M. R. (2001), 'Specifying concrete for chloride environments using controlled permeability formwork', *Materials and Structures* **34**(243), 566–576.

Miguel-Ángel, C., Carmona, J. and Garcés, P. (2016), 'Graphite-cement paste: A new coating of reinforced concrete structural elements for the application of electrochemical anti-corrosion treatments', *Coatings* **6**(3).

Mistral Industrial Chemicals (n.d.), 'Mistral industrial chemicals carbon black powder', `https://mistralni.co.uk/products/carbon-black-powder`. Accessed 17/02/2020.

Murphy, E. K., Mahara, A. and Halter, R. J. (2017), 'Absolute Reconstructions Using Rotational Electrical Impedance Tomography for Breast Cancer Imaging', *IEEE Transactions on Medical Imaging* **36**(4), 892–903.

Nguyen, D. L., Song, J., Manathamsombat, C. and Kim, D. J. (2014), 'Comparative electromechanical damage-sensing behaviors of six strain-hardening steel fiber-reinforced cementitious composites under direct tension', *Composites Part B: Engineering* **69**, 159–168.

Niederleithinger, E., Wolf, J., Mielentz, F., Wiggenhauser, H. and Pirskawetz, S. (2015), 'Embedded ultrasonic transducers for active and passive concrete monitoring.', *Sensors (Basel, Switzerland)* **15**(5), 9756–72.

Ogunsola, A., Reggiani, U. and Sandrolini, L. (2009), Shielding properties of conductive concrete against transient electromagnetic disturbances, *in* '2009 IEEE International Conference on Microwaves, Communications, Antennas and Electronics Systems, COMCAS 2009', IEEE, pp. 1–5.

Oh, T. I., Wi, H., Kim, D. Y., Yoo, P. J. and Woo, E. J. (2011), 'A fully parallel multi-frequency EIT system with flexible electrode configuration: KHU Mark2.', *Physiological measurement* **32**(7), 835–49.

Packham, B., Koo, H., Romsauerova, A., Ahn, S., McEwan, A., Jun, S. C. and Holder, D. S. (2012), 'Comparison of frequency difference reconstruction algorithms for the detection of acute stroke using EIT in a realistic head-shaped tank', *Physiological Measurement* **33**(5), 767–786.

Paine, K., Lark, R. and Al-Tabbaa, A. (2015), Biomimetic multi-scale damage immunity for concrete, *in* 'Concrete Research: Driving Profit and Sustainability', University of Bath.

Pan, P., Wu, S., Xiao, F., Pang, L. and Xiao, Y. (2015), 'Conductive asphalt concrete: A review on structure design, performance, and practical applications', *Journal of Intelligent Material Systems and Structures* **26**(7), 755–769.

Persson, P. and Strang, G. (2004), 'A Simple Mesh Generator in MATLAB', *SIAM Review* **46**(2), 329–345.

Pomerantsev, A. L. (2005), *Progress in Chemometrics Research*, Nova Science Publishers.

Prem, P. R. and Murthy, A. R. (2017), 'Acoustic emission monitoring of reinforced concrete beams subjected to four-point-bending', *Applied Acoustics* **117**, 28–38.

Reichling, K., Raupach, M. and Klitzsch, N. (2014), 'Determination of the distribution of electrical resistivity in reinforced concrete structures using electrical resistivity tomography', *Materials and Corrosion* pp. n/a–n/a.

Rucka, M. and Wilde, K. (2015), 'Ultrasound monitoring for evaluation of damage in reinforced concrete', *Bulletin of the Polish Academy of Sciences Technical Sciences* **63**(1), 65–75.

Rudin, L. I., Osher, S. and Fatemi, E. (1992), 'Nonlinear total variation based noise removal algorithms', *Physica D: Nonlinear Phenomena* **60**(1-4), 259–268.

Saint-Gobain Formula (n.d.), 'Dentstone KD Plaster'.
URL: *http://www.saintgobainformula.com/eng/Products/Plaster/Dentstone-KD*

Seppänen, A., Hallaji, M. and Pour-Ghaz, M. (2017), 'A functionally layered sensing skin for the detection of corrosive elements and cracking', *Structural Health Monitoring: An International Journal* **16**(2), 215–224.

Shengxi, S., Yujie, Y. and Xiaoya, Y. (2011), 'Conductivity and mechanical properties study of steel fiber reinforced graphite conductive concrete', *Mechanic Automation and Control Engineering (MACE), 2011 Second International Conference on* pp. 2052–2054.

Shi, C., Jiménez, A. F. and Palomo, A. (2011), 'New cements for the 21st century: The pursuit of an alternative to Portland cement', *Cement and Concrete Research* **41**(7), 750–763.

Sigma-Aldrich (n.d.*a*), 'Sigma-aldrich carbon nanofibers', `https://www.sigmaaldrich.com/catalog/product/aldrich/719811?lang=en&region=GB`. Accessed 17/02/2020.

Sigma-Aldrich (n.d.*b*), 'Sigma-aldrich carbon nanotube, multi-walled', `https://www.sigmaaldrich.com/catalog/product/aldrich/659258?lang=en&region=GB&cm_sp=Insite-_-prodRecCold_xviews-_-prodRecCold10-5`. Accessed 17/02/2020.

Smyl, D., Hallaji, M., Seppänen, A. and Pour-Ghaz, M. (2016), 'Three-Dimensional Electrical Impedance Tomography to Monitor Unsaturated Moisture Ingress in Cement-Based Materials', *Transport in Porous Media* pp. 1–24.

Smyl, D., Pour-Ghaz, M. and Seppänen, A. (2018), 'Detection and reconstruction of complex structural cracking patterns with electrical imaging', *NDT and E International* **99**, 123–133.

Stauffer, D. and Aharony, A. (1994), *Introduction To Percolation Theory*, second edn, Taylor & Francis.

Suryanto, B., McCarter, W. J., Starrs, G. and Chrisp, T. M. (2017a), Characterization of Fly-ash using Electrochemical Impedance Spectroscopy, *in* 'Procedia Engineering', Vol. 171, Elsevier Ltd, pp. 705–714.

Suryanto, B., McCarter, W. J., Starrs, G. and Ludford-Jones, G. V. (2016), 'Electrochemical immittance spectroscopy applied to a hybrid PVA/steel fiber engineered cementitious composite', *Materials and Design* **105**, 179–189.

Suryanto, B., Saraireh, D., Kim, J., McCarter, W. J., Starrs, G. and Taha, H. M. (2017b), 'Imaging water ingress into concrete using electrical resistance tomography', *International Journal of Advances in Engineering Sciences and Applied Mathematics* **9**(2), 109–118.

Swisstom AG (2013), 'Swisstom - Lots of tail wind during market launch of first product', Press release.

The Concrete Society (2000), Concrete Society Technical Report No. 54 - Diagnosis of deterioration in concrete structures, Technical report, The Concrete Society.

The Concrete Society (2010), Concrete Society Technical Report No. 22 Fourth Edition - Non-structural cracks in concrete, Technical report, The Concrete Society.

Torrents, J. M., Mason, T. O., Peled, A., Shah, S. P. and Garboczi, E. J. (2001), 'Analysis of the impedance spectra of short conductive fiber-reinforced composites', *Journal of Materials Science* **36**(16), 4003–4012.

Tseng, K. K. and Wang, L. (2004), 'Smart piezoelectric transducers for in situ health monitoring of concrete', *Smart Materials and Structures* **13**(5), 1017–1024.

Tumidajski, P. J., Xie, P., Arnott, M. and Beaudoin, J. J. (2003), 'Overlay current in a conductive concrete snow melting system', *Cement and Concrete Research* **33**(11), 1807–1809.

Vauhkonen, P., Vauhkonen, M., Savolainen, T. and Kaipio, J. (1999), 'Three-dimensional electrical impedance tomography based on the complete electrode model', *IEEE Transactions on Biomedical Engineering* **46**(9), 1150–1160.

Wang, D., Wang, Q. and Huang, Z. (2019), 'Investigation on the poor fluidity of electrically conductive cement-graphite paste: Experiment and simulation', *Materials and Design* **169**.

Wang, J., Dewanckele, J., Cnudde, V., Van Vlierberghe, S., Verstraete, W. and De Belie, N. (2014), 'X-ray computed tomography proof of bacterial-based self-healing in concrete', *Cement and Concrete Composites* **53**, 289–304.

Wansom, S., Kidner, N. J., Woo, L. Y. and Mason, T. O. (2006), 'AC-impedance response of multi-walled carbon nanotube/cement composites', *Cement and Concrete Composites* **28**(6), 509–519.

Wen, S. and Chung, D. (2003), 'A Comparative Study of Steel- and Carbon-Fiber Cement as Piezoresistive Strain Sensors', *Advances in Cement Research* **15**(3), 119–128.

Whittington, H. W., McCarter, J. and Forde, M. C. (1981), 'The conduction of electricity through concrete', *Magazine of Concrete Research* **33**(114), 48–60.

Wi, H., Sohal, H., McEwan, A. L., Woo, E. J. and Oh, T. I. (2014), 'Multi-frequency electrical impedance tomography system with automatic self-calibration for long-term monitoring.', *IEEE transactions on biomedical circuits and systems* **8**(1), 119–28.

Woo, L. Y., Wansom, S., Hixson, A. D., Campo, M. A. and Mason, T. O. (2003), 'A universal equivalent circuit model for the impedance response of composites', *Journal of Materials Science* **38**(10), 2265–2270.

Wu, J., Liu, J. and Yang, F. (2015), 'Three-phase composite conductive concrete for pavement deicing', *Construction and Building Materials* **75**, 129–135.

Wu, Y., Jiang, D., Duan, J., Liu, X., Bayford, R. and Demosthenous, A. (2018), Towards a High Accuracy Wearable Hand Gesture Recognition System Using EIT, *in* '2018 IEEE International Symposium on Circuits and Systems (ISCAS)', IEEE, pp. 1–4.

Wypych, G. (2016), fourth edition edn, ChemTec Publishing.

Xie, P., Gu, P., Fu, Y. and Beaudoin, J. J. (1995), 'Conductive cement-based compositions'.

Xin, Y., Zhu, G. and Yu, L. (2012), Freeze/thaw durability of carbon fiber reinforced concrete, *in* 'Applied Mechanics and Materials', Vol. 174-177, pp. 816–820.

Xu, S., Liu, J. and Li, Q. (2015), 'Mechanical properties and microstructure of multi-walled carbon nanotube-reinforced cement paste', *Construction and Building Materials* **76**, 16–23.

Xue, W., Wang, L., Wang, D. and Druta, C. (2014), 'Pavement Health Monitoring System Based on an Embedded Sensing Network', *Journal of Materials in Civil Engineering* **26**(10), 04014072.

Yang, L., Xu, C., Dai, M., Fu, F., Shi, X. and Dong, X. (2016), 'A novel multi-frequency electrical impedance tomography spectral imaging algorithm for early stroke detection', *Physiological Measurement* **37**(12), 2317–2335.

Yang, W. Q. and Peng, L. (2003), 'Image reconstruction algorithms for electrical capacitance tomography', *Measurement Science and Technology* **14**(1), R1–R13.

Yao, A. and Soleimani, M. (2013), 'A pressure mapping imaging device based on electrical impedance tomography of conductive fabrics', *Sensor Review* **32**(4), 310–317.

Yim, H. J., Lee, H. and Kim, J. H. (2017), 'Evaluation of mortar setting time by using electrical resistivity measurements', *Construction and Building Materials* **146**, 679–686.

Yuan, Q., Junrui, C., Weihua, D., Faning, D., Man, L. and Zengguang, X. (2015), 'A quasi real-time approach to investigating the damage and fracture process in plain concrete by X-ray tomography', *Journal of Civil Engineering and Management* pp. 1–8.

Yuan, Y. Q., Gao, D. Y., Shao, H. J. and Fan, Y. D. (2011), 'Research on Ice and Snow Melting by Conductive Asphalt Concrete', *Applied Mechanics and Materials* **97-98**, 429.

Zhang, B., Zhou, Z. and Li, X. (2010), 'A Crack Monitoring Method for Concrete Structures', *Intelligent Automation and Soft Computing* **16**(5), 763–770.

Zhang, J., Xu, L. and Zhao, Q. (2017), 'Investigation of carbon fillers modified electrically conductive concrete as grounding electrodes for transmission towers: Computational model and case study', *Construction and Building Materials* **145**, 347–353.

Zhang, L., Han, B., Ouyang, J., Yu, X., Sun, S. and Ou, J. (2017), 'Multifunctionality of cement based composite with electrostatic self-assembled CNT/NCB composite filler', *Archives of Civil and Mechanical Engineering* **17**(2), 354–364.

Zhang, W. and Li, D. (2014), 'An instrumental electrode model for solving EIT forward problems.', *Physiological measurement* **35**(10), 2001–26.

Zhang, Y., Xiao, R. and Harrison, C. (2016), Advancing Hand Gesture Recognition with High Resolution Electrical Impedance Tomography, *in* 'Proceedings

of the 29th Annual Symposium on User Interface Software and Technology - UIST '16', ACM Press, New York, New York, USA, pp. 843–850.

Zhou, Z., Dowrick, T., Malone, E., Avery, J., Li, N., Sun, Z., Xu, H. and Holder, D. (2015), 'Multifrequency electrical impedance tomography with total variation regularization.', *Physiological measurement* **36**(9), 1943–61.

A | Appendix

This appendix gives the Matlab scripts used to produce Electrical Impedance Tomography (EIT) images in Chapters 5 and 8. Some code related to formatting and saving of output has been removed to reduce the length of the section. Some scripts are presented as functions; their arguments are explained in comments.

All of these scripts have been tested in Matlab R2018b. Each of them requires the EIDORS library (Adler and Lionheart, 2006) to have been installed and initialised before they will run. They are known to work with EIDORS v3.9, and may run with other versions too.

A.1 Imaging of dental plaster cylinders

The script used to produce the images in Section 5.1.

```
%Arguments:
%sample_no and frequency are used to find the files
%alpha is the hyperparameter

function image = plaster_reconstr_func(sample_no, frequencyA, frequencyB,
    ↪ alpha)

switch sample_no
    case 1
        dirA = strcat('\Data\Plaster_imaging\One_cast\', num2str(frequencyA),'
            ↪ KHz\');
        dirB = strcat('\Data\Plaster_imaging\One_cast\', num2str(frequencyB),'
            ↪ KHz\');
    case 2
        dirA = strcat('\Data\Plaster_imaging\Two_cast\', num2str(frequencyA),'
            ↪ KHz\');
```

```
        dirB = strcat('\Data\Plaster_imaging\Two_cast\', num2str(frequencyB),'
            ↪ KHz\');
    case 3
        dirA = strcat('\Data\Plaster_imaging\Three_cast\', num2str(frequencyA),
            ↪ 'KHz\');
        dirB = strcat('\Data\Plaster_imaging\Three_cast\', num2str(frequencyB),
            ↪ 'KHz\');
    case 4
        dirA = strcat('\Plaster_imaging\Four_cast\', num2str(frequencyA),'KHz\'
            ↪ );
        dirB = strcat('\Data\Plaster_imaging\Four_cast\', num2str(frequencyB),'
            ↪ KHz\');
end

%Model inputs
num = 16; %number of electrodes
len = 1.5; %length of electrodes in cm
diam = 10; %diameter of the disc in cm

%Figure out the arc angle
theta = len/(diam/2);
htheta = theta / 2;
elec_pts = cell(num); %creates empty cell array

incr = (2*pi)/num; %Find the arc which we will add to each position to roll
    ↪ around the circle

for i = 0:num-1
   elec_pts{i+1} = [sin((i*incr) - htheta),cos((i*incr) - htheta);sin((i*incr)
       ↪  + htheta),cos((i*incr) + htheta)];
end

model_type = 'a2C'; %This is a variable so it can be printed or otherwise
    ↪ output

%Eidors needs certain fields set up, this passage sets them
plas_fmdl = mk_common_model(model_type,16);
plas_fmdl.fwd_model = dm_2d_circ_pt_elecs(elec_pts, [], [0.05,10,0.02] );
[stim,mpat] = mk_stim_patterns(num, 1, '{ad}','{ad}',{'no_meas_current'},1); %
    ↪ This depends on the hardware setup
```

```
plas_fmdl.fwd_model.normalize_measurements = 0;
plas_fmdl.fwd_model = setfield(plas_fmdl.fwd_model, 'solve', 'eidors_default')
    ↪ ;
plas_fmdl.fwd_model = setfield(plas_fmdl.fwd_model, 'system_mat', '
    ↪ eidors_default');
plas_fmdl.fwd_model = setfield(plas_fmdl.fwd_model, 'jacobian', '
    ↪ eidors_default');

prior = @prior_tikhonov;

plas_fmdl.fwd_model.stimulation = stim;
plas_fmdl.fwd_model.meas_select = mpat;
plas_fmdl.hyperparameter.value = alpha;
plas_fmdl.RtR_prior = prior;
plas_fmdl.fwd_model.gnd_node = 1;
%Now we have a reasonably nice mesh

%Data comes out of the KHU2.5 in a format that MATLAB takes in very easily
%using load;
numscans = 5;

%Average the scans for some noise reduction
dataA = load(strcat(dirA, '1Scan.txt'));
re_dataA = zeros(size(dataA, 1), numscans);
re_dataB = re_dataA;

for i = 1:numscans
    dataA = load(strcat(dirA, num2str(i), 'Scan.txt'));
    re_dataA(:,i) = dataA(:,3);
    dataB = load(strcat(dirB, num2str(i), 'Scan.txt'));
    re_dataB(:,i) = dataB(:,3);
end

KHzA = mean(re_dataA, 2);
KHzB = mean(re_dataB, 2);

%Ignore self-measurments
rem = [1,2,16,17,18,19,34,35,36,51,52,53,68,69,70,85,86,87,102,103,104,
      ... 119,120,121,136,137,138,153,154,155,170,171,172,187,188,189,
      ... 204,205,206,221,222,223,238,239,240,241,255,256];
```

```
KHzA(rem) = [];
KHzB(rem) = [];

%Got to scale the data, the machine picks up different magnitudes at
%different freqs
scale_factor = mean(KHzA)/mean(KHzB);
KHzB = KHzB * scale_factor;

plas_solv = inv_solve(plas_fmdl,KHzA,KHzB);

image = plas_solv;
end
```

A.2 Imaging of concrete cylinders

The script used to produce the images in Section 5.2.

```
%Arguments:
%sample_no and frequency are used to find the files
%alpha is the hyperparameter

%Arbitrary sample numbering used just for this: Plastic tube is 1, One
%rebar is 2, Two rebars is 3.
function image = concrete_reconstr_func(sample_no, frequencyA, frequencyB,
    ↪ alpha)

numscans = 20; %number of scans, user to change

switch sample_no
    case 1
        dirA = strcat('\Data\Concrete_imaging\plastic_', num2str(frequencyA),'k
            ↪ \');
        dirB = strcat('\Data\Concrete_imaging\plastic_', num2str(frequencyB),'k
            ↪ \');
    case 2
        dirA = strcat('\Data\Concrete_imaging\onerebar_', num2str(frequencyA),'
            ↪ k\');
        dirB = strcat('\Data\Concrete_imaging\onerebar_', num2str(frequencyB),'
            ↪ k\');
    case 3
```

```
        dirA = strcat('\Data\Concrete_imaging\tworebar_', num2str(frequencyA),'
            ↪ k\');
        dirB = strcat('\Data\Concrete_imaging\tworebar_', num2str(frequencyB),'
            ↪ k\');
end

stimpattern = '{ad}';

dataA = load(strcat(dirA, '1Scan.txt'));
re_dataA = zeros(size(dataA, 1), numscans);
re_dataB = re_dataA;

for i = 1:numscans
    dataA = load(strcat(dirA, num2str(i), 'Scan.txt'));
    re_dataA(:,i) = dataA(:,3);
    dataB = load(strcat(dirB, num2str(i), 'Scan.txt'));
    re_dataB(:,i) = dataB(:,3);
end

KHzA = mean(re_dataA, 2);
KHzB = mean(re_dataB, 2);

% Scale the data, the machine picks up different magnitudes at
% different freqs
scale_factor = mean(KHzA)/mean(KHzB);
KHzB = KHzB * scale_factor;

%%%=========================%%%
%Make a model
%Firstly, figure out the electrode points.
%Basically the dm_2d_circ_pt_elecs() function wants to take an array of
%startx, starty;endx, endy

%Model inputs
num = 16; %number of electrodes
len = 1; %length of electrodes in cm
diam = 15; %diameter of the disc in cm

%Figure out the arc angle
theta = len/(diam/2);
htheta = theta / 2;
```

```
elec_pts = cell(num); %create empty cell array

incr = (2*pi)/num; %Find the arc which we will add to each position to roll
    ↪ around the circle

for i = 0:num-1
    elec_pts{i+1} = [sin((i*incr) - htheta),cos((i*incr) - htheta);sin((i*incr
        ↪ ) + htheta),cos((i*incr) + htheta)];
end
model_type = 'a2C'; %This is a variable so it can be printed or otherwise
    ↪ output

%Settings needed for the jacobian calculation
imdl = mk_common_model(model_type,16);
meshparams = [0.05,10,0.02];
imdl.fwd_model = dm_2d_circ_pt_elecs(elec_pts, [], meshparams); %first term in
    ↪  the [] is coarseness of the mesh
[stim,mpat] = mk_stim_patterns(num, 1, stimpattern ,'{ad}',{'no_meas_current'
    ↪ },1); %This depends on the hardware setup
%Remove the self-measurements.
rem = find(mpat == 0);
KHzA(rem) = [];
KHzB(rem) = [];

imdl.fwd_model.stimulation = stim;
imdl.fwd_model.meas_select = mpat;
imdl.fwd_model.jacobian = 'eidors_default';
imdl.fwd_model.solve = 'eidors_default';
imdl.fwd_model.system_mat = 'eidors_default';
imdl.fwd_model.normalize_measurements = 'eidors_default';

image = mk_image(imdl);
J = calc_jacobian(image);

reg = prior_tikhonov(imdl); %This is an identity matrix of the appropriate
    ↪ size

%Regularise (tk-r)
volt_diff = KHzA - KHzB;

y = (J'*J + alpha*reg) \ J'*(-volt_diff); %The tk-r eqn
```

```
image.elem_data = y;
end
```

A.3 Imaging of conductive mortar cylinders

The script used to produce the images in Section 8.3.1.

```
%Arguments:
%sample_no and frequency are used to find the files
%alpha is the hyperparameter
function image = timediff_reconstr_func(sample_no, frequency, alpha)
%Data comes out of the KHU2.5 in a format that MATLAB takes in very easily
%using load.

numscans = 50; %number of scans, user to change

dirA = strcat('H:\PhD\Output\cbm_cyl_imaging\study_data\Method_C\homog\',
    ↪ num2str(frequency),'KHz\');
dirB = strcat('H:\PhD\Output\cbm_cyl_imaging\study_data\Method_C\cyl', num2str
    ↪ (sample_no), '\', num2str(frequency), 'KHz\');

stimpattern = '{ad}';

dataA = load(strcat(dirA, '1Scan.txt'));
re_dataA = zeros(size(dataA, 1), numscans);
re_dataB = re_dataA;

for i = 1:numscans
    dataA = load(strcat(dirA, num2str(i), 'Scan.txt'));
    re_dataA(:,i) = dataA(:,3);
    dataB = load(strcat(dirB, num2str(i), 'Scan.txt'));
    re_dataB(:,i) = dataB(:,3);
end

KHzA = mean(re_dataA, 2);
KHzB = mean(re_dataB, 2);


%%%=========================%%%
```

```
%Make a model
%Firstly, figure out the electrode points.
%Basically the dm_2d_circ_pt_elecs() function wants to take an array of
%startx, starty;endx, endy

%user inputs
num = 16; %number of electrodes
len = 0.5; %length of electrodes in cm
diam = 6.4; %diameter of the disc in cm

%Figure out the arc angle
theta = len/(diam/2);
htheta = theta / 2;
elec_pts = cell(num); %create empty cell array

incr = (2*pi)/num; %Find the arc which we will add to each position to roll
    ↪ around the circle
for i = 0:num-1
    elec_pts{i+1} = [sin((i*incr) - htheta),cos((i*incr) - htheta);sin((i*incr
        ↪ ) + htheta),cos((i*incr) + htheta)];
end
model_type = 'a2C'; %This is a variable so it can be printed or otherwise
    ↪ output

%Settings needed for the jacobian calculation
imdl = mk_common_model(model_type,16);
imdl.fwd_model = dm_2d_circ_pt_elecs(elec_pts, [], [0.08,4.5,0.02] ); %first
    ↪ term in the [] is coarseness of the mesh
[stim,mpat] = mk_stim_patterns(num, 1, stimpattern ,'{ad}',{'no_meas_current'
    ↪ },1); %This depends on the hardware setup
%Remove the self-measurements.
rem = find(mpat == 0);
KHzA(rem) = [];
KHzB(rem) = [];


imdl.fwd_model.stimulation = stim;
imdl.fwd_model.meas_select = mpat;
imdl.fwd_model.jacobian = 'eidors_default';
imdl.fwd_model.solve = 'eidors_default';
imdl.fwd_model.system_mat = 'eidors_default';
```

```
imdl.fwd_model.normalize_measurements = 'eidors_default';

image = mk_image(imdl);
J = calc_jacobian(image);

reg = prior_tikhonov(imdl); %This is an identity matrix of the appropriate
    ↪ size

volt_diff = KHzA - KHzB;

y = (J'*J + alpha*reg) \ J'*(-volt_diff); %The tk-r eqn

image.elem_data = y;
end
```

A.4 Combination of images

The script used to produce the image combinations shown in Sections 8.3.2 and 8.8.1, using the algorithm described in Section 8.2.5. Two versions of this script were used, one for the frequency difference scripts and one for the time difference script. The time difference version is included here. The two combination scripts differ only in the way the reconstruction functions are called. More detail in included in comments.

```
%How this works, broadly:
% - A number of images are acquired at different parameters. EIDORS caching
    ↪ means these images share a mesh which simplifies things substantially
% - These images are thresholded in one of two ways depending on user
% choice: either at a certain fraction of their maximum element value, or
% the top x percentage of element values. See lines 30, 49
% - The set of remaining nonzero elements is identified for each image
% - Two further sets are found: a set of all elements that are above the
    ↪ threshold in all of the images (1), and a set of all elements above the
% threshold in at least one image (2)
% - Each element from set (1) is scanned for adjacent elements within set (2)
% - This process is repeated until all of the elements in set (2) that are
    ↪ connected to an element in set (1) are found
%In this way features that we are confident actually exist from the less noisy
    ↪  images are given the detail that they have in the noisier images,
```

```
%without allowing the noise to obscure the overall picture.
clear
%This is the version for time difference imaging. It was used for the
%imaging of conductive mortar cylinders. It differs from the frequency
%difference imaging version in the user inputs (one fewer than fd) and
%the initial function call (line 25).

%Do some image reconstructions.
alphas = [1e-2 1e-3 1e-4];
sample = 1;
freq = 1;
image_cells = cell(1, size(alphas, 2));
for images = 1:size(alphas, 2)
    image_cells{images} = timediff_reconstr_func(sample,freq,alphas(images));
end
fprintf('\r\r');

%Must choose the threshold type:
threshold = 0;
if threshold
    threshold_frac = 0.4;
    fprintf('Thresholding␣element␣values.');
else
    include_percent = 10;
    fprintf('Including␣a␣top␣percentage␣of␣elements.');
end
%Not preallocating the cell arrays because they are relatively small.
for images = 1:size(image_cells, 2)
    %Pull out the vertexes/simplexes. The vtx are pairs of X,Y co-ords, and
        ↪ the
    %simplexes are defined in terms of the indexes of the three vertexes that
    %they incorporate.
    vtx{images} = image_cells{images}.fwd_model.nodes;
    elems{images} = image_cells{images}.fwd_model.elems;

    actualelemdata{images} = [(1:size(image_cells{images}.elem_data, 1))'
        ↪ image_cells{images}.elem_data]; %Save the reconstruction. Give the
        ↪ elements their IDs.
    otherelem_inds{images} = 1:size(image_cells{images}.elem_data, 1);
    %How are we doing the element cropping...
    if threshold
```

```
        %Find regions relative to a threshold
        maxelem{images} = max(image_cells{images}.elem_data);
        minelem{images} = min(image_cells{images}.elem_data);
        highelem_inds{images} = find(image_cells{images}.elem_data > (maxelem{
            ↪ images} * threshold_frac));
        lowelem_inds{images} = find(image_cells{images}.elem_data < (minelem{
            ↪ images} * threshold_frac));

        %Remove everything with low magnitude - probably not inclusions
        zeroelem_inds{images}([highelem_inds{images}; lowelem_inds{images}]) =
            ↪ [];
    else
        %Find the x% most resistive and conductive regions
        sorted{images} = sortrows(actualelemdata{images}, 2);
        lowbound{images} = floor((size(image_cells{images}.elem_data, 1) / 100)
            ↪  * (include_percent / 2));
        highbound{images} = size(image_cells{images}.elem_data, 1) - lowbound{
            ↪ images};
        highelem_inds{images} = sorted{images}(highbound{images}:end,1); %Need
            ↪ to have these indexes for figuring out which of the carried over
            ↪  elements are high and low conductivity later on
        lowelem_inds{images} = sorted{images}(1:lowbound{images},1);
        sorted{images}([1:lowbound{images} highbound{images}:end], :) = [];
        zeroelem_inds{images} = sort(sorted{images}(:,1));
    end
    image_cells{images}.elem_data(zeroelem_inds{images}) = 0;

    %Match the probable inclusions to their simplexes
    featured_inds{images} = find(image_cells{images}.elem_data ~= 0); %Indexes
        ↪  of elements, not vertexes
    featured_elems{images} = elems{images}(featured_inds{images},:);
    featured_vtx{images} = unique([featured_elems{images}(:,1); featured_elems
        ↪ {images}(:,2); featured_elems{images}(:,3)]);
end

%Generate sets of elements (1) and (2) by looping through each image
repeat_elem_inds = featured_inds{1}; %Start this out somewhere so it can be
    ↪ repeatedly intersected.
all_featured_elem_inds = featured_inds{1};
for images = 2:size(featured_inds, 2)
    repeat_elem_inds = intersect(repeat_elem_inds, featured_inds{images});
```

```
    all_featured_elem_inds = [all_featured_elem_inds; featured_inds{images}];
end
all_featured_elem_inds = unique(all_featured_elem_inds);
repeat_elems = elems{1}(repeat_elem_inds, :); %Can use elems{1} because the
    ↪ mesh is shared
all_featured_elems = elems{1}(all_featured_elem_inds, :);

%Need to find all featured elems connected to the repeated ones, and save them
    ↪ .
%Start with the vtxs of the repeat_elems - the ones we're surest are features.

%Find the indexes of all simplexes/elements associated with these vtxs
disp('Tracking');
carried_elem_inds = []; %Indexes inside the all_featured_elems set rather than
    ↪  the OG set, annoyingly
carried_elems = repeat_elems;
new_elem_count = 1;
prev_elem_count = 0;
%How this loop works:
% - The 'carried elems' start out as the ones that are known to repeat in all
    ↪ reconstruction runs. Then
%as elements are found, these are carried over between loops.
% - The outer while loop tracks how many new connected elements were
    ↪ discovered in the previous run,
%and stops the loop once new elements are no longer being found.
% - The for i loop goes through each element in the carried_elems - recall
    ↪ that this is a three value vector giving
%the indexes of the vertexes associated with the element. It sets the
    ↪ current_elem var.
% - The for j loop goes through the three vertexes in each element, and finds
    ↪ other elements from the set of featured elements
%that they appear in. It adds the indexes to the connected elements to
    ↪ connected_elem_inds. This vector is then added to the end of
%the vector of indexes of carried elements. The connect_elem_inds vector is
    ↪ reset on every iteration. Carried_elems is
%reset after every element in the previous carried_elems has been tested.
%There is some scope here for optimisation by ensuring that each element is
    ↪ only ever tested once, but this is not necessary right now.
while (new_elem_count - prev_elem_count) > 0
    prev_elem_count = size(carried_elem_inds, 1);
    for i = 1:size(carried_elems, 1) %Go through all of the elements that
```

```
        ↪ appear to be in a region shared between the runs
        current_elem = carried_elems(i,:);
        for j = 1:size(current_elem, 2)
            %Finding the elements connected to the current one
            current_vtx = current_elem(j);
            vert1 = find(all_featured_elems(:,1) == current_vtx);
            vert2 = find(all_featured_elems(:,2) == current_vtx);
            vert3 = find(all_featured_elems(:,3) == current_vtx);
            %The indexes within all_featured_elems of the newly found
            %connected elements
            connected_elem_inds = unique([vert1; vert2; vert3]);
            %Save the carried indexes
            carried_elem_inds = unique([carried_elem_inds; connected_elem_inds
                ↪ ]);
        end
    end
    %Need to update the elems matrix. Carried_elem_inds indexes the
        ↪ all_featured_elems matrix
    carried_elems = all_featured_elems(carried_elem_inds, :);
    new_elem_count = size(carried_elem_inds, 1);
end
%Convert back to the original elems format
carried_elem_inds = all_featured_elem_inds(carried_elem_inds);

%Distnguish between conductive and non-conductive regions
carried_highelem_inds = highelem_inds{1};
carried_lowelem_inds = lowelem_inds{1};
for images = 2:size(image_cells, 2)
    %Intersect all of the known high and low elems with the whole set of
        ↪ carried elems
    carried_highelem_inds = unique([carried_highelem_inds; intersect(
        ↪ carried_elem_inds, highelem_inds{images})]);
    carried_lowelem_inds = unique([carried_lowelem_inds; intersect(
        ↪ carried_elem_inds, lowelem_inds{images})]);
end

%Any of the images is fine here
image_cells{size(image_cells, 2)}.elem_data(:) = 0;
image_cells{size(image_cells, 2)}.elem_data(carried_highelem_inds) = 1;
image_cells{size(image_cells, 2)}.elem_data(carried_lowelem_inds) = -1;
```

```
%Visualise
image_cells{size(image_cells, 2)}.calc_colours.cmap_type = parula(256);
show_fem(image_cells{size(image_cells, 2)});
eidors_colourbar(image_cells{size(image_cells, 2)});
axis off

fig = gcf; %These lines stop the pdfs saving at very large size.
fig.PaperPositionMode = 'auto';
fig_pos = fig.PaperPosition;
fig.PaperSize = [fig_pos(3) fig_pos(4)];
```